TAMPEREEN TEKNILLINEN YLIOPISTO
TAMPERE UNIVERSITY OF TECHNOLOGY

Jukka Viinamäki

Aspects on Designing Power Electronic Converters for Photovoltaic Application

Julkaisu 1513 • Publication 1513

Tampere 2017

Tampereen teknillinen yliopisto. Julkaisu 1513
Tampere University of Technology. Publication 1513

Jukka Viinamäki

Aspects on Designing Power Electronic Converters for Photovoltaic Application

Thesis for the degree of Doctor of Science in Technology to be presented with due permission for public examination and criticism in Rakennustalo Building, Auditorium RG202, at Tampere University of Technology, on the 15th of December 2017, at 12 noon.

Tampereen teknillinen yliopisto - Tampere University of Technology
Tampere 2017

Doctoral candidate: Jukka Viinamäki
Laboratory of Electrical Energy Engineering
Faculty of Computing and Electrical Engineering
Tampere University of Technology
Finland

Supervisor: Teuvo Suntio, Prof.
Laboratory of Electrical Energy Engineering
Faculty of Computing and Electrical Engineering
Tampere University of Technology
Finland

Pre-examiners: Adrian Ioinovici, Prof., IEEE Fellow
Electrical and Electronics Engineering
Holon Institute of Technology
Israel

Richard Redl, Dr., IEEE Fellow
Redl Consulting
Switzerland

Opponent: Jorma Kyyrä, Prof.
Electrical Engineering and Automation
Aalto University
Finland

ISBN 978-952-15-4049-3 (printed)
ISBN 978-952-15-4072-1 (PDF)
ISSN 1459-2045

ABSTRACT

The amount of electrical energy produced by using grid-connected photovoltaic (PV) power plants has increased rapidly during the last decade and the upward trend is expected to continue in the future. The conversion from direct current (dc) produced by the photovoltaic generator (PVG) to alternating current (ac) fed into the grid is made by using the power electronic device called PV inverter. The PV inverter can be implemented using single dc-ac inverter, or there might be an additional voltage boosting dc-dc converter between the PVG and the dc-ac inverter. Corresponding names are single-stage and two-stage PV inverter. Depending on the topology of the dc-ac inverter, it can have single-phase or three-phase grid connection.

When the PV inverter is feeding power to the grid and operating at unity power factor, it is said to operate in grid-feeding mode. In countries, where the share of distributed generation is high, the inverter is also required to operate in grid-supporting mode. In the future, the inverter is possibly required to operate also in grid-forming mode. In this operating mode, the inverter defines the grid voltage and creates the grid locally.

As the amount of installed PV capacity is expected to increase in the future, it becomes increasingly important to design the PV inverters to be reliable, cheap, efficient and able to operate in all the above mentioned operating modes. For this reason, all the topics studied in this thesis are focusing on the design of the PV inverter.

The component sizing and control design of dc-dc converter operating as a part of two-stage single-phase PV inverter is studied. The operation in grid-feeding and grid-forming modes are both investigated separately. Also the attenuation of double-line-frequency voltage ripple from the dc-link voltage to the voltage of the PVG, when using dc-link voltage feedforward is studied. The target in the attenuation of the double-line-frequency voltage ripple is to enable using of smaller and more reliable components.

Minimization of the size of the grid filter of single-stage three-phase PV inverter might yield saturating filter inductors. As the trend is towards even more cost-efficient and small inverters, it is important to study the effects of inductor saturation on the performance of the inverter. The simulation model of single-stage grid-connected three-phase photovoltaic inverter having saturating L-filter inductors is developed. The developed model is used for studying the effect of saturating filter inductors on the low-frequency and switching-frequency current harmonics produced by the inverter.

PREFACE

This work was carried out at the Laboratory of Electrical Energy Engineering (LEEE) of Tampere University of Technology (TUT) during the years 2013 - 2017. The research was funded by TUT, Fortum Foundation, and ABB Oy. I also highly appreciate the personal grant from Otto A. Malm Foundation.

First of all, I want to express my gratitude to Professor Teuvo Suntio for supervising my thesis. Your support have been invaluable with the research itself but also with the writing process. Secondly, I want to thank my former colleagues Ph.D. Juha Jokipii, Assistant Professor Tuomas Messo, Ph.D. Jenni Rekola, M.Sc. Aapo Aapro, M.Sc. Jyri Kivimäki, and M.Sc. Kari Lappalainen for sharing your ideas and offering valuable comments on the problems I faced with the research during these years. It has been motivating to work together with highly talented people working with positive and encouraging attitude. I also want to thank Ph.D. Anssi Mäki, Ph.D. Lari Nousiainen, Ph.D. Joonas Puukko, Ph.D. Juha huusari, and Ph.D. Diego Torres Lobera for the guidance in the beginning of my doctoral studies. I am thankful to Professor Adrian Ioinovici and Dr. Richard Redl for pre-examining the thesis and for offering constructive comments helping me to further improve the quality of the manuscript. Moreover, I want to thank laboratory engineers Pentti Kivinen and Pekka Nousiainen for helping to build the laboratory prototypes, and Merja Teimonen, Terhi Salminen, Nitta Laitinen, Mirva Seppänen, Päivi Oja-Nisula, and Jukka Kaipainen for taking care of various practical matters at the office.

Finally, I want to thank my life partner Sanna, mother Mailis, brother Jussi and my sister Katriina for your support and encouragement during my doctoral studies. You all made this possible.

Tampere, December 2017

Jukka Viinamäki

SYMBOLS AND ABBREVIATIONS

Abbreviations

ac	Alternating current
CC	Constant current
CD	Conventional design
CF	Current-fed
CPG	Constant power generation
CV	Constant voltage
CCM	Continuous conduction mode
dB	Decibel
dc	Direct current
DG	Distributed generation
DSP	Digital signal processor
ESS	Energy storage system
LHP	Left half plane
LVRT	Low-voltage-ride-through
MD	Modified design
MPP	Maximum power point
MPPT	Maximum power point tracking
p.u.	Per unit
PC	Personal computer
OC	Open circuit
PF	Power factor
PI	Proportional-integral controller
PID	Proportional-integral-derivative controller
PLL	Phase-locked loop
PV	Photovoltaic
PVG	Photovoltaic generator
PWM	Pulse-width modulation
RHP	Right half plane
SAS	Solar array simulator
SC	Short circuit
SPWM	Sinusoidal pulse width modulation
SR	Sizing ratio
SRF-PLL	Synchronous reference frame phase-locked loop
STC	Standard-test condition
THD	Total harmonic distortion

VF	Voltage-fed
VSI	Voltage-source inverter

Greek characters

Δ	Determinant, difference
ω	Angular frequency
Ψ	Flux linkage
θ	Phase angle

Latin characters

a	Diode ideality factor
$\mathbf{A}$	Coefficient matrix of the state-space representation
$\mathbf{B}$	Coefficient matrix of the state-space representation
$\mathbf{C}$	Coefficient matrix of the state-space representation
c	Control variable
C_1	Capacitance of the input capacitor
C_2	Capacitance of the output capacitor
d	Differential operator
D, d	Duty ratio
D', d'	Complement of the duty ratio
$\mathbf{D}$	Coefficient matrix of the state-space representation
f	Frequency
$\mathbf{G}$	Transfer function matrix
G	Transfer function, solar irradiance
G_{a}	Modulator gain
G_{c}	Transfer function of the controller
G_{ci}	Control-to-input transfer function
G_{co}	Control-to-output transfer function
G_{ff}	Feedforward gain
G_{io}	Forward transfer function
G_{se}	Measurement gain
$\mathbf{I}$	Identity matrix
$i_{\mathrm{pv}}, I_{\mathrm{pv}}$	Photovoltaic generator current
$i_{\mathrm{dc}}, I_{\mathrm{dc}}$	Current from the dc-dc converter to the dc-link
$i_{\mathrm{ph}}, I_{\mathrm{ph}}$	Photocurrent
$i_{\mathrm{d}}, I_{\mathrm{d}}$	Diode current
i_{in}	Input current
i_{o}	Output current

k	Boltzmann constant
L	Inductance, loop-gain
m	Modulation index
N_{bp}	Number of bypassed cells
N_{s}	Number of series connected cells
q	Electron charge
r_{pv}	Dynamic resistance of a photovoltaic generator
R_{pv}	Static resistance of a photovoltaic generator
R_{sh}	Shunt resistance of a PVG
R_{s}	Series resistance of a PVG
r_{D}	Diode on-state resistance
r_{sw}	On-state resistance of a MOSFET
r_{C}	Parasitic resistance of a capacitor
r_{L}	Parasitic resistance of an inductor
s	Laplace variable
t	Time
T	Temperature
T_{oi}	Reverse-voltage transfer function
$\mathbf{u}$,$\mathbf{U}$	Input vector
V_{D}	Diode threshold voltage
v_{dc}, V_{dc}	DC-link voltage
v_{in}	Input voltage
v_{o}	Output voltage
v_{pv}, V_{pv}	Voltage across the terminals of a photovoltaic generator
$\mathbf{x}$,$\mathbf{X}$	State vector
$\mathbf{y}$,$\mathbf{Y}$	Output vector
Y_{in}	Input admittance
Y_{out}	Output admittance
Z_{in}	Input impedance
Z_{out}	Output impedance

Subscripts

c	Refers to closed-loop transfer function
ff	Refers to transfer functions under dc-link voltage feedforward
in	Refers to input-side transfer function
inf	Refers to ideal transfer function
max	Refers to maximum value
min	Refers to minimum value

mpp	Refers to operation at the MPP
nom	Refers to nominal operating condition
num	Refers to numerator
o	Refers to open-loop transfer function
oc	Refers to operation in open-circuit condition
out	Refers to output-side transfer function
p-p	Refers to peak-to-peak-value
ro	Refers to reference-to-output transfer function
sc	Refers to operation in short-circuit condition
stc	Refers to operation in standard test condition
zc	Refers to zero-state in case of centered PWM
zt	Refers to zero-state in case of trailing edge PWM

Superscripts

ff	Refers to transfer functions under dc-link voltage feedforward
g	Refers to g-parameter model
h	Refers to h-parameter model
in	Refers to transfer functions of an input voltage-controlled converter
lf	Refers to low-frequency
S	Refers to source-affected transfer functions
z	Refers to z-parameter model

CONTENTS

1 INTRODUCTION

In this chapter, the background information about the research conducted in this thesis is introduced. The role of the solar photovoltaic (PV) systems in the electricity production is discussed and its future views are evaluated. After this, the commonly used PV plant concepts and the basic properties of the photovoltaic generator (PVG) are presented. Next, a short literature review on the investigated topics is given. Finally, the main scientific contributions of the thesis are summarized.

1.1 Electricity production using renewable energy sources

Electric energy is the most widely used form of energy in modern society. It is used e.g. for manufacturing, transportation, communications, heating and cooling. In 2014, world gross electricity production was 23 815 TWh and it was shared between different sources as follows: Coal 40.8 %, natural gas 21.6 %, hydro 16.4 %, nuclear 10.6 %, oil 4.3 %, renewables (exl. hydro) 7.5 %, biofuels and waste 3.1 %. These numbers are slightly diffenrent when the total primary energy supply is investigated: Coal 28.6 %, oil 31.3 %, natural gas 21.2 %, nuclear 4.8 %, hydro 2.4 %, biofuels and waste 10.3 % and renewables(exl. hydro) 1.4 % (International Energy Agency, 2016a). The share of oil is much higher as it is used widely in transportation.

Unfortunately, burning of fossil fuels produces pollutant gases, of which, CO_2 is considered to be the most detrimental as it is shown to be the main contributor to the global warming. Even if nuclear power does not produce the above mentioned gasses, the risk of radiation hazard is serious (Bose, 2010). As a recent example, the accident in Fukushima nuclear plant in 2011 has accelerated the discussion about other alternatives for non-polluting energy production. According to climate change agreement contracted at Paris climate conference in December 2015, 195 countries agreed to limit global warming well below 2 °C and the agreement is due to enter into force in 2020. In order to reach this objective, it is necessary to reduce the share of energy produced by the fossil fuels and to increase the share of energy produced by renewable energy sources. Actually, the increase of renewable power generation has already begun as will be later discussed.

Renewable energy resources include hydro, solar, wind, geothermal and tidal. Hydro has already quite significant share of the energy supply and therefore, significant increase is difficult to obtain. Thus, solar energy is considered to be one of the most promising

alternatives (Romero-Cadaval et al., 2013) and (Kouro et al., 2015). Solar energy can be used to heat water using solar thermal collector or it can be converted directly into electricity by using photovoltaic generator. The amount of installed PV capacity has increased rapidly during the last decade and the annual growth is fast. The total amount of installed photovoltaic capacity was 227 GW in the end of 2015. The capacity was increased by 50 GW compared to previous year and the upward trend is expected to continue in the future (International Energy Agency, 2016b).

More than 99% of the installed PV capacity is grid-connected and the rest are stand-alone systems (Kouro et al., 2015). In grid connected PV systems, the direct current produced by the PVG is converted to ac and interfaced to the grid by using power electronic converter, i.e. inverter. In addition to PVG itself, also the inverter plays important role in the PV system. Thus, it is important to study how these inverters can be designed to be reliable, cheap, efficient and able to support electricity network for stable operation as well.

1.2 Properties of a photovoltaic generator

The photovoltaic generator consists of photovoltaic cells. The single photovoltaic cell is basically a $p-n$ junction that converts the sunlight into electrical current by photovoltaic effect. Commonly used materials in commercial PV cells are monocrystalline and polycrystalline silicon. In this case, the voltage across the terminals of a single PV cell is less than one volt. Therefore, cells are connected in series to form PV panel. The maximum voltage is approximately 40 V in 250 W PV panel. The amount of maximum current can be increased by increasing the cell area or by connecting cells in parallel. The series connection of PV panels is called string and combination of series and parallel connected cells is called PV array. Photovoltaic generator is a general name for a system consisting of several PV panels.

Electrical properties of a PV panel can be modeled by equivalent circuit based on one-diode model shown in Fig. 1.1, where I_{ph} is the photocurrent generated by the incident light, R_{s} is the equivalent series resistance of the PV panel and R_{sh} is the equivalent parallel resistance (Villalva et al., 2009). The current produced by PV panel can be expressed mathematically using one-diode model as

$$I_{\mathrm{pv}} = I_{\mathrm{ph}} - I_0 \left[\exp\left(\frac{V_{\mathrm{pv}} + R_{\mathrm{s}} I_{\mathrm{pv}}}{N_{\mathrm{s}} a k T/q} \right) - 1 \right] - \frac{V_{\mathrm{pv}} + R_{\mathrm{s}} I_{\mathrm{pv}}}{R_{\mathrm{sh}}}, \tag{1.1}$$

where, I_0 is the saturation diode current, N_{s} is the number of series connected cells, a is the diode ideality factor, k is the Bolzmann constant, T is the temperature of the $p-n$ junction and q is the electron charge. Even if more complex models has been presented,

one-diode model offers good compromise between accuracy and complexity.

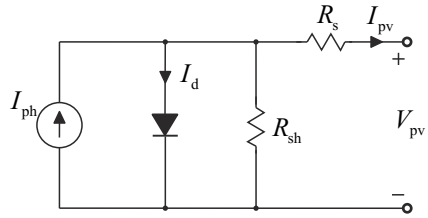

Fig. 1.1: The equivalent circuit of a PV panel based on one-diode model.

When I_{pv} is zero, PV panel operates in open-circuit (OC) condition. Respectively, when the voltage V_{pv} is zero, PV panel operates in short-circuit (SC) condition. In both of these conditions, the output power of the PV model is zero. The output power is maximized at a certain operating point called maximum power point (MPP), located between these conditions. The dependency of output current, output power and dynamic resistance on voltage in a typical PV panel is shown in Fig. 1.2. As the current is almost constant in the area between the SC condition and MPP, it is called constant current (CC) region. Correspondingly, the area between MPP and SC condition is called constant voltage (CV) region. The dynamic resistance represents the low-frequency value of the PV panel output impedance and can be defined as

$$r_{pv} = -\frac{\Delta v_{pv}}{\Delta i_{pv}}, \tag{1.2}$$

where the minus sign indicates that the current is flowing out from the PVG. As shown in Fig. 1.2, the dynamic resistance is nonlinear and dependent on the operating point. At the MPP, static and dynamic resistances are equal, i.e. $r_{pv} = U_{mpp}/I_{mpp} = R_{pv}$ (Wyatt and Chua, 1983). In CC region, dynamic resistance is higher than static resistance, whereas in CV region, dynamic resistance is lower than static resistance.

The current-voltage (IV) curve of a PV panel is shown in Fig. 1.3 for two different irradiance and ambient temperature levels. As it is shown, the current produced by the PV panel is linearly dependent on irradiance level and inversely proportional to temperature. However, the effect of irradiance is much stronger compared to the effect of temperature level. Correspondingly, the voltage across the PV panel terminals is inversely proportional to temperature and it is also slightly affected by the irradiance level. The highest output power is obtained at low temperature and high irradiance level.

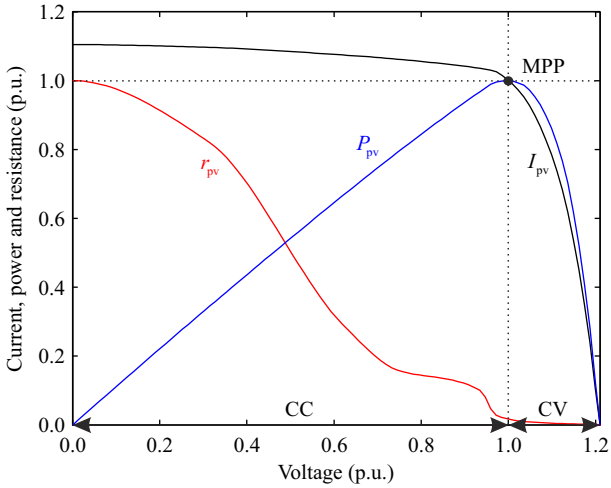

Fig. 1.2: Typical IV curve and dynamic resistance of a PV panel.

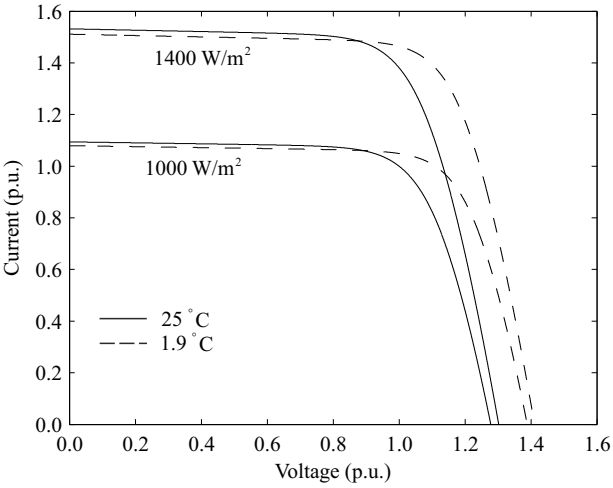

Fig. 1.3: The effect of temperature and irradiance on IV curve of a PV panel.

Manufacturers of PV panels provide values of OC voltage, SC current, MPP voltage and MPP current in the datasheet of the panel. These values are measured in Standard Test Condition (STC), i.e. when the irradiance is 1000 W/m^2 and the ambient temperature is 25 °C. However, the ambient temperature is usually higher and the irradiance is varying due to the passing clouds. In addition, the irradiance can be reflected from the clouds yielding as high irradiance as 1400 W/m^2 at the surface of the PV panel (Luoma et al., 2012). This phenomenon is known as cloud enhancement. The maximum value of the produced current and power together with the maximum voltage must be taken into

account in the design of the interfacing converter.

In addition to temperature and voltage, also the distribution of solar irradiance on a PV generator surface affects heavily the IV curve and maximum output power of the PV generator. The surface can be shaded partially or entirely e.g. by clouds, buildings and trees. In order to prevent heating of shaded cells by the non-shaded cells, manufacturers add so called bypass diodes antiparallel of group of cells. Typically, the size of the cell group is around 20 cells yielding three bypass diodes in 190 W PV panel. In this kind of PV panel, three separate maximum power points can occur if the irradiance level is different for each group.

The MPP locates at the lowest voltage level, when two out of three cell groups are shaded. This situation is shown in Fig. 1.4, where the output current (solid line) and power (dashed line) are shown as functions of voltage. The irradiance of the non-shaded cell is 1000 W/m^2 and 100 W/m^2 for the shaded cells. In this situation, the voltage of the MPP is one third of the MPP voltage in non-shaded condition. If the maximum power is to be extracted also in this situation, the input voltage range of the interfacing converter should be wide, as it should be able to handle also the maximum OC voltage of the PVG.

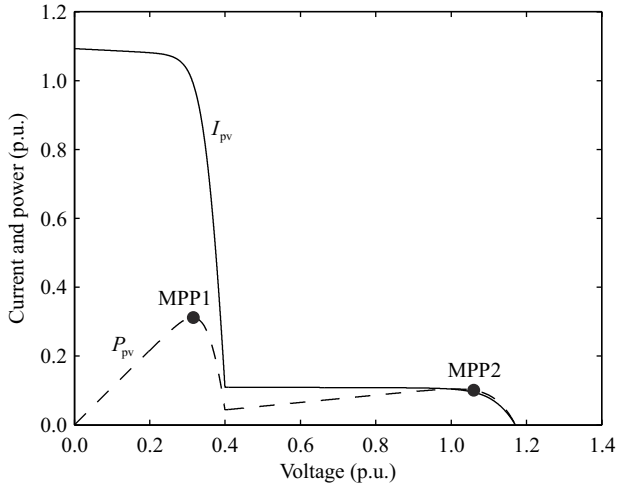

Fig. 1.4: The effect of partial shading on IV curve of a PV panel.

As the location of the MPP is constantly varying, the operating point of the interfacing converter must be changed as well in order to extract maximum power from the PVG. Various maximum power point tracking (MPPT) algorithms have been developed for this purpose (Esram and Chapman, 2007). Perturb & Observe (P&O) is simple and one of the most widely used methods, where the operation point is changed in small steps.

If the power level was increased, second step is made to the same direction, but if the power level was decreased, the direction of the step is changed. One of the drawbacks of this algorithm is that it can locate only local MPP but fails to locate global MPP. For example, if the P&O algorithm starts from OC voltage in Fig. 1.4, it goes to lower voltage levels step-by-step. Once it obtains MPP2, it starts to oscillate around it and will not go down to MPP1 even if the power level would be higher. For this reason, also algorithms for tracking the global MPP has been developed (Boztepe et al., 2014).

1.3 Grid-connected PV power plant concepts

According to Blaabjerg et al. (2004); Kjaer et al. (2005), four most commonly used PV power plant concepts are as shown in Fig. 1.5. In module-integrated-inverter concept, each PV panel is connected to the grid by a dedicated micro inverter. Due to the operating principle of a typical grid-connected inverter, the input voltage must be higher than the peak value of the grid voltage. As the voltage of single PV panel is low, usually two stage conversion scheme is used, i.e., voltage-boosting dc-dc converter is connected between the PV panel and the inverter. Also galvanic isolation is usually provided in the dc-dc stage using high-frequency (HF) transformer. The main benefit of this approach is the ability to locate the MPP of each PV panel, which is important in severe partial shading conditions as in complex roof structures. Unfortunately, the main drawbacks are lower power converter efficiency and higher price per kW compared to other approaches. Even if various micro inverters are available in the market, their share on the total PV electricity production is small (Kouro et al., 2015).

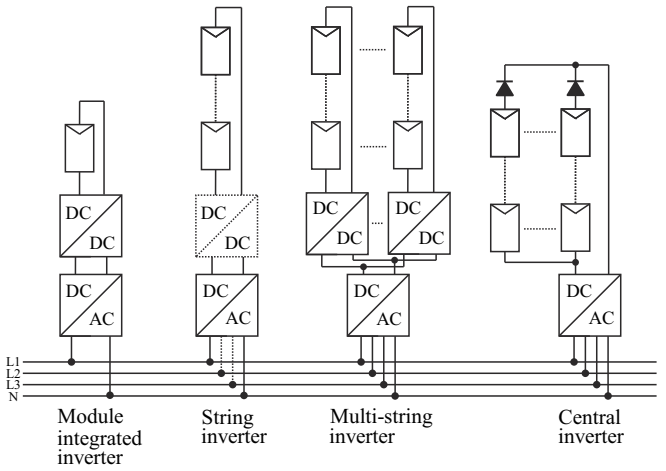

Fig. 1.5: PV power plant concepts.

The voltage of the PVG can be increased by connecting several PV panels in series. String inverter is used to connect this type of PV generator to the grid. Usually the amount of series connected PV panels is high enough so that the voltage-boosting dc-dc converter is not required. However, as the wide input voltage range enables the operation at the MPP in different partial shading conditions, the two-stage conversion is also commonly used in string inverters. As MPP cannot be reached in the panel level, the MPPT efficiency is lower compared to module-integrated-inverter. However, the converter efficiency is higher and price per kW is lower. The string inverter concept is mainly used in domestic and other small to medium scale PV power plants (Kouro et al., 2015).

In multi-string concept, fewer PV panels are connected in series suggesting better MPPT efficiency in partial shading conditions, compared to string inverter concept. These strings are connected to the inverter by individual dc-dc converter stage. It is more cost-effective to use several dc-dc converters than several string inverters. Galvanic isolation can be included also into multi-string inverter. Multi-string concept is more common in medium to large-scale PV power plants (Kouro et al., 2015).

Central inverter is one of the most common concepts in large-scale PV power plants. The PV array is formed by connecting separate strings in parallel using a blocking diode in series with each string. These blocking diodes protect shaded strings from damaging in partial shading conditions. Clear drawback of this concept is its inability to locate more than single MPP for the whole PV array yielding low MPPT efficiency. However, the efficiency of the inverter is high and the structure of the PV plant is simple.

1.4 Design of PV inverter

Design of PV inverter includes various application specific requirements such as high efficiency, long warranty periods (to extend the lifetime closer to PVG), high power quality, endurance of heavily fluctuating power, leakage current minimization, and special control requirements such as grid support functions and MPPT (Kouro et al., 2015). Decreasing price of the PVG has increased the share of the PV inverter on the total price of the PV plant. Thus, also the price minimization is increasingly important design parameter.

At present, the total cost of a PV power plant is approximately 1000 €/kW in Germany. The share of PV inverter is 11 % and the share of PV generator is 55 %. The remaining 34 % includes all other components such as mounting system, cabling, etc. The total price of the PV power plant is expected to decrease down to 610 €/kW or even as low as 280 €/kW by 2050 (Mayer et al., 2015). This suggests that also inverter cost must be significantly reduced in the future. As the cost can be affected by careful design of the PV inverter, the following sections discuss the design considerations of dc-dc and

dc-ac converters in PV application.

1.4.1 Design considerations of dc-dc converter in PV application

As it was mentioned earlier, addition of dc-dc converter between the PVG and the dc-ac inverter increases the input voltage range of the PV inverter. When considering conventional MPPT operation, the main benefit is increased MPP range. It is also beneficial to implement the galvanic isolation in the dc-dc converter if such property is required in the local grid code. As the share of the electricity produced by PV power plants increases, it becomes more important to implement grid-supporting functions in the PV inverters. One of these functions is the ability to limit the output power of the PV inverter. This means that instead of MPP operation, the inverter is limiting the output power referred to as a constant power generation (CPG). In order to obtain CPG in varying environmental conditions, two stage conversion might be compulsory (Cai et al., 2016; Sangwongwanich et al., 2016; Tonkoski et al., 2011; Yang et al., 2014). Moreover, bidirectional dc-dc converters are required in grid-connected energy storage systems (ESS) (Grainger et al., 2014). Due to the aforementioned reasons, using of double stage conversion in future PV inverters seems essential. Thus, main focus of this thesis is on the control design and component sizing of dc-dc converters in PV application.

Typically the PVG and the power electronic devices are purchased from different manufacturers. The required number of PV panels is calculated by dividing the target power level of the PV plant by the STC power provided in the panel datasheet. The power electronic devices are further selected based on the STC power of the PVG. It must also be checked that the maximum input current of the PV inverter is high enough and the input voltage range is suitable for the PVG. The relation between the STC power of the PVG $P_{\mathrm{PV,STC}}$ and the nominal power of the inverter $P_{\mathrm{inv,nom}}$ can be described by the dc-ac ratio or by its inverse, the sizing ratio SR:

$$SR = \frac{P_{\mathrm{inv,nom}}}{P_{\mathrm{pv,stc}}}, \tag{1.3}$$

The optimal value of sizing ratio is extensively studied in the literature (Burger and Rüther, 2006; Chen et al., 2011, 2013; Koutroulis and Blaabjerg, 2011; Luoma et al., 2012; Mondol et al., 2006; Notton et al., 2010; Sulaiman et al., 2012; Tonkoski and Lopes, 2011; Zhu et al., 2011). The optimal value depends on the location of the PV plant, government incentives, inverter power efficiency curve, inverter protection scheme, cost of the PV panels and inverters, cloud shading conditions, etc. (Chen et al., 2011; Luoma et al., 2012). The optimum value of the sizing ratio in the range of 0.6-1.5 has been suggested.

As the PV inverter is not usually designed for a specific PVG, the inverter manufacturers aim to design the inverter as generally applicable as possible. Therefore, the input current of the inverter is usually calculated by diving the nominal power of the converter by the minimum input voltage (*Datasheet of ABB string inverter PRO-33.0*, 2016; *Datasheet of Sunny Tripower 10000TLEE-JP*, 2016; *Datasheet of Vacon 8000 solar inverter series*, 2014). This is also the case in (Ho et al., 2013, 2012), where the interleaved voltage-boosting converter was designed for PV application. By dividing the nominal power by the minimum input voltage it is guaranteed that the nominal power can be handled over the whole input voltage range. However, as the source is PVG, the power is maximized at higher than the minimum voltage. This design method yields reasonable design when the input voltage range is narrow. However, it yields oversized components and uneven temperature distribution if used for designing PV inverter having wide input voltage range, as shown in Chapter 2.

Single-phase PV inverters are used in small-scale residential string inverters and in micro inverters as it was shown in Fig. 1.5. The grid current and voltage are both fluctuating at the grid frequency. When assuming unity power factor, the output power of a single phase inverter is fluctuating at twice the grid frequency. This power fluctuation causes voltage ripple in the dc-link voltage and the PVG voltage. However, the PVG voltage should be as constant as possible to maximize the energy yield (Sullivan et al., 2013) and maintain stable operation of the MPPT (Femia et al., 2009). The low-frequency ripple causes problems also in lightning and fuel-cell applications, when single-phase inverter is used (Sun et al., 2016). Various solutions has been presented to prevent output power ripple from affecting the input power, i.e. to implement power decoupling (Hu et al., 2013; Sun et al., 2016; Tang and Blaabjerg, 2015).

In case of two stage conversion scheme, a large capacitor can be connected in parallel to the PVG or the dc-link capacitance can be increased to produce power decoupling. As the dc-link voltage level is higher than the PVG voltage, the same amount of capacitance produces stronger power decoupling, when added to the dc-link instead of adding it parallel to the PVG. As large capacitor parallel to the PVG also limits the control bandwidth of the input voltage controlled dc-dc converter, increasing the dc-link capacitance is the best of these two passive power-decoupling options.

The dc-link voltage ripple is inversely proportional to the capacitance value of the dc-link capacitor. Minimized capacitance value is desired, as the reliability could be improved if electrolytic capacitors could be replaced by film or other type of capacitors. It is possible to use relatively small capacitor yielding high ripple if the ripple is prevented from affecting the PVG voltage. This ripple-rejection capability can be obtained by using input-voltage control in the dc-dc converter. It has been shown that the double-line frequency ripple can be attenuated by using simple I-type controller (Viinamaki et al.,

2014), high bandwidth PI controller together with quasi-resonant controller (Gu et al., 2014) or high bandwidth PID controller (Femia et al., 2009). High-bandwidth input-voltage control enables also faster MPPT, yielding higher MPPT efficiency compared to open-loop operation. Despite these advantages, the open-loop operation is still widely used. The reasons for its popularity might be simplicity and lower risk for instability as there are no feedback loops.

The double-line frequency ripple rejection capability can be implemented also in dc-dc converter operating in open loop by using dc-link voltage feedforward (Mirzahosseini and Tahami, 2012). Input voltage feedforward has been conventionally used in voltage sourced dc-dc converters to reduce the magnitude of the audio susceptibility, i.e. input-to-output transfer function (Kazimierczuk and Starman, 1999; Redl and Sokal, 1986). It has also been used in PFC boost converters to reduce harmonic components from grid current (Van De Sype et al., 2005). However, using of feedforward in this application has not been extensively studied so far. In Chapter 2, small-signal model of conventional voltage-boosting dc-dc converter including dc-link voltage feedforward is shown. The presented model is used for studying the factors affecting the maximum attenuation of double-line frequency voltage ripple.

1.4.2 Selection of passive components in three-phase dc-ac inverter

Two-level three-phase dc-ac inverter is commonly used topology in higher power level string inverters and central inverters. It consists of switch bridge, input or dc-link capacitor and grid connection filter. Many studies has been carried out on sizing of dc-link capacitor and grid connection filter as these passive components are the biggest contributors to the size and cost of the inverter. The minimum capacitance value of the input capacitor is limited by the maximum allowable voltage ripple and the stability of the control loop. In (Messo et al., 2014), design rules were presented for the minimum dc-link capacitance, when considering the stable operation of the PV inverter.

In grid-connected PV inverters, LCL-type grid filter is typically used. It offers the same attenuation capability in smaller size compared to L-type filter, which was popular in traditional grid-connected inverters. The selection of the optimum capacitance and inductance values of the LCL-type grid filter has been studied in (Beres et al., 2016; Channegowda and John, 2010; Karshenas and Saghafi, 2006; Lang et al., 2005; Liserre et al., 2004, 2005; Muhlethaler et al., 2013; Pan et al., 2014; Zheng et al., 2013). In (Pan et al., 2014), the focus was on the inductor design and it was shown how the core material can be saved by combining the cores of the filter inductors. In (Muhlethaler et al., 2013), it was shown how the optimal LCL-filter design is a compromise between the losses and filter size.

Using of soft-saturating core materials without discrete air gap or by minimizing the

core size yield an inductor, which will saturate during the grid period. The inductance of the saturating inductor is current dependent, whereas in linear inductor the inductance is approximately constant. Given that the cost and size of PV inverter must be further reduced and using of saturating inductors might help to obtain this target, it is important to study the effect of saturating filter inductors on the performance of the PV inverter.

The effect of saturation and hysteresis can be investigated by the Jiles-Atherton model (Liu et al., 2012; Ngo, 2002; Sadowski et al., 2002). If the target is to model only the inductor saturation and the inclusion of hysteresis does not provide any useful information, the effect of hysteresis can be neglected. In this case, a simple behavioral model can be used (Perdigao et al., 2008; Wölfle and Hurley, 2003). The Jiles-Atherton model is based on the physical properties of the core material, whereas the behavioral model is based on the measured properties of the inductor. In (Di Capua and Femia, 2016), a behavioral model including inductor saturation and temperature dependency was developed. It was also demonstrated that this model predicts the switching-frequency current ripple of the dc-dc converter correctly.

The modeling and simulation of saturated induction motors is widely studied in the literature. An extensive literature review on these models is given in (Nandi, 2004). It also proposes a new model for predicting the low-frequency current harmonics produced by the saturation in induction motor aiming to fault analysis. Most of the presented models are also based on measured parameters and are rather behavioral than physical models. For example in (Donescu et al., 1999), the dependency of magnetizing inductance on stator flux was measured in three operating points and the mathematical representation was fitted to the measured data. As the simplified equivalent circuit of induction motor resembles the grid-connected PV inverter, some of the results observed in the operation of saturating induction motors might be valid also for the PV inverter. However, these similarities might not be easy to observe due to the complexity of the motor model.

Mastromauro et al. studied the effect of saturating inductor in the L-filter of a grid-connected single-phase inverter and explained by Volterra theory that applying 50 Hz sinusoidal voltage across the saturating inductor produces third and fifth harmonics to the current (Mastromauro et al., 2008). Moreover, the presence of third harmonic voltage produces third, ninth and fifteenth harmonic currents. If both of these components are applied at the same time, intermodulation components are also produced. Furthermore, Wolfe and Hurley explained through Fourier analysis that the saturating inductor produces odd harmonics (Wölfle and Hurley, 2003). In (Mastromauro et al., 2008), it was also shown that in case of single-phase inverter, the harmonics caused by inductor saturation can be effectively attenuated using resonant or repetitive controllers.

In Chapter 4, the effect of saturating L-filter inductor on the low-frequency current harmonics of three-phase PV inverter is studied by simulations and experimental mea-

surements. Also an equation for approximating the switching-frequency ripple of the L-filter inductor is developed. The developed equation can be used for studying the ripple in case of saturating inductors having different inductance-current (LI) dependency.

1.5 Grid-feeding, grid-forming and grid-supporting operation modes of PV inverter

At present, the PV inverters connected to low-voltage grid are usually required to operate at unity power factor (PF) and to operate at the MPP. Furthermore, the inverter is disconnected in case of grid fault. These requirements are determined in the grid code locally. As the share of renewable energy sources on the total electricity production increases, shutting down several distributed generation (DG) plants simultaneously will have severe effect on the grid stability. Other well known issue of the renewable energy sources is the intermittent nature, which will also affect the grid stability due to the power imbalance. In order to ensure reliable operation of the grid, various improvements have been suggested to the current grid codes and some of them has already been executed in countries having high penetration of renewable energy (Yang et al., 2015).

In Germany, the PV power plants having rated power below 30 kWp have to be able to limit the maximum feed-in power (e.g. 70% of the rated power). This means that the inverter has to be able to operate in power limiting mode called constant power generation (CPG) in addition to MPPT. This operation is also described in the Danish grid code (Sangwongwanich et al., 2016). The aim is to improve the power balance of the grid by cutting the highest peaks from the feed-in power. These peaks could also be handled by using energy storage systems (ESS), but their extensive use would require cheaper and more reliable ways to store energy. Thus, CPG is seen as good method to avoid the use of ESS at the moment.

Several countries have also requirement to feed reactive power to the grid by the PV inverter in case of voltage sag in medium- and high-voltage grids. This property is known as low-voltage-ride-through (LVRT) capability (Neves et al., 2016). In (Yang et al., 2015) it was suggested that LVRT requirement should be applied also for low-voltage grid. When the PV inverter is performing some of these grid-supporting functions, it is said to operate in grid-supporting mode.

When the PV inverter is feeding power to the grid at unity power factor and operates at the MPP, it is said to operate in grid-feeding mode. In grid-feeding operation, the inner control loop of the inverter controls the grid current. The q-component reference is set to zero for unity power factor, and the d-component reference is determined by the dc-link voltage controller. In case of two-stage conversion, dc-dc converter controls the PVG voltage and the reference value is given by the MPPT. In case of single-stage conversion, the outer control loop of the inverter is controlling the PVG voltage instead

of the dc-link voltage. The control scheme is basically similar in grid-support operation. However, in this case, the grid current q-component can be controlled to increase the grid voltage or the MPPT can be disabled and the reference value of the PVG voltage controller can be determined, e.g., by CPG function.

The purpose of LVRT is to support the grid during a short-term voltage sag. If the grid voltage drops down for longer period, the inverter must be disconnected from the grid for safety reasons according to majority of current grid codes. This might be changed in the future, when the microgrid vision will turn into reality (Mastromauro, 2014). Microgrid refers to a small-scale network composed of distributed power generation as PV and wind power plants, ESSs and consumers. The communication between the parts of microgrid is much heavier than in current grid enabling the stable operation of the grid even without large large-scale power plants such as nuclear etc. (Bacha et al., 2015; Rocabert et al., 2012; Wang et al., 2015). In microgrid, the grid-connected PV inverter can operate either in grid-feeding, grid-supporting or grid-forming operation modes (Rocabert et al., 2012). In grid-forming operation, the inverter will determine the grid voltage. In case of double-stage PV inverter, the dc-link voltage is determined by the dc-dc converter. The power fed to the grid is determined by the local load, suggesting that MPPT cannot be used. In addition to microgrid, some grid codes allow the grid-forming operation already in small-scale (islanding), under condition that the islanded grid is isolated from the grid (Bacha et al., 2015).

In ESS, where a dc-dc converter is connected between PVG and a battery, the converter must be able to operate in MPPT mode, when the voltage of the battery is below the set limit. After the voltage exceeds this limit, operation mode is changed to constant voltage charging. This means that the converter must be able to quickly change between MPPT mode and output voltage control mode (Qin et al., 2015). The control problem is the same for dc-dc converter in two-stage PV inverter, which must be able to operate in grid-feeding and grid-forming operation modes. According to previous discussion, it is important to understand how the operation in both of these modes affects the control design and component selection of the converter.

When operating in MPPT mode, the dc-dc converter can operate either in open loop or in closed loop. If the converter is operating in open loop, the tracker speed must be small. Using closed loop operation, higher speed and better MPPT efficiency can be obtained. In case of open-loop operation, the output of the MPPT is duty cycle. Respectively, when the converter is operating in closed loop, the PVG voltage is controlled and the output of the MPPT is the PVG voltage reference. The voltage of the PVG is usually controlled instead of the current as the rate of change is much bigger in current than in voltage. This means that the PVG must be modeled as a current source in this case. As the source in conventional applications has usually been voltage

source, also PVG is still often modeled as a voltage source (Danyali et al., 2014; Villalva et al., 2010). However, also publications where the current source is used, are presented (Messo et al., 2012; Urtasun et al., 2013). In this thesis, the combined dynamics of the voltage-boosting converter and PVG is presented, and the developed small-signal model is used for analyzing the effect of dc-link voltage feedforward and input voltage control on double-line-frequency ripple attenuation.

The small-signal model of the voltage-boosting converter is different when the converter controls the dc-link voltage. Contrary to the input voltage control, the converter can be designed for stable operation only in CC or in CV region. In (Konstantopoulos and Alexandridis, 2013), nonlinear voltage regulator was used to solve this problem. In (Qin et al., 2015), the stability of output-voltage-controlled voltage-boosting converter was studied and it was verified that the converter cannot be stable in both of these regions with the same controller. However, explanation was not provided for this behavior. In Chapter 3 of this thesis, the small-signal model of output-voltage-controlled voltage-boosting converter is presented by modeling the PVG as current source and as voltage source. The difference between these models are explained. Using the developed models, the limiting factors affecting the control design and component selection are shown.

1.6 The objectives of the thesis

The aim was to study the component selection and control design of voltage-boosting dc-dc converter operating as a part of two-stage single-phase PV inverter. Operation in grid-feeding and grid-forming modes were both studied. In case of grid-feeding operation, the attenuation of double-line-frequency voltage ripple from the dc-link voltage to the voltage of the PVG was taken into account in the control design. During the studies, it was realized that this attenuation can be improved by adding dc-link voltage feedforward to the converter. Thus, one of the set targets was to find out the factors affecting the maximum available attenuation of double-line-frequency voltage ripple when using dc-link voltage feedforward. Finally, the effect of using saturating grid filter inductors in the grid-connected three-phase PV inverter on low-frequency and switching-frequency harmonics was studied. The intention was to find out if the low-frequency harmonics would be too high to be attenuated by the conventional control methods. Also, as the varying inductance in saturating grid filter inductors is never in their minimum value at the same time in all the three phases, it was considered if the three-phase inverter would offer any benefit over the single-phase inverter, when the saturating inductors are used.

1.7 Main scientific contributions

The main scientific contributions of this thesis can be summarized as

- The dynamic model of voltage-boosting dc-dc converter operating as a part of two-stage PV inverter is developed. Grid-feeding and grid-forming modes are both studied. When the inverter is operating in grid-forming mode, the dc-dc converter controls the dc-link voltage. It is explained, why the same controller cannot be used in the whole operating range of the PV generator. It is shown that the low-frequency RHP zero occurring in current region limits the bandwidth of the controller to a low value. High-bandwidth controller can be used only in voltage region. However, if the PV generator operating point goes from voltage region to current region, the voltage will collapse and the controller will not recover. Contrary to this, the current region controller is able to recover from the unstable region if the operating point enters into voltage region and back.

- It is shown that taking into account the properties of a PV generator, when designing a voltage-boosting dc-dc converter, yields smaller inductor size, smaller input capacitor and smaller heat sink compared to the conventional method, when the input voltage range of the converter is wide.

- The small-signal model is developed and used to study the attenuation of double-line-frequency voltage ripple in the voltage-boosting dc-dc converter using dc-link voltage feedforward and operating the converter in open loop. It is shown that the maximum attenuation is obtained by using as high dc-link voltage as possible, as small measurement error as possible, and by ensuring that the losses between the upper and lower switches are as equal as possible.

- Two different simulation models are developed and used to show that the saturation of grid filter inductors in grid-connected three-phase VSI introduces 5^{th} and 7^{th} harmonics to the grid current but they can be effectively attenuated by using conventional PI controllers in the dq-frame. Also an equation for approximating the amplitude of switching frequency current ripple in three-phase PV inverter having saturating grid filter is presented and validated.

1.8 Related publications and author's contribution

The author made the analysis, designed and built the prototype converters, made the measurements and was the main author in writing of [P1-P5]. In [P6], the author participated in the analysis and made the measurements. Prof. Suntio was supervising the research documented in [P1-6]. He also introduced valuable ideas and comments related to the conducted research and was the main author in [P6]. Dr.Tech. Jokipii helped with the analysis in [P2-P3] and with the proofreading in [P2-P6]. He gave also valuable support for building the prototype inverter used for the measurements in [P3]. Dr.Tech. Messo participated in the analysis and helped with the measurements in [P5]

and [P6]. M.Sc. Kivimäki and M.Sc. Hietalahti helped with the proofreading in [P4]. Prof. Kuperman gave support for writing of [P1], [P5] and [P6].

[P1] Viinamäki, J., Kuperman, A., Suntio, T. (2017). "Grid-forming-mode operation of boost-power-stage converter in PV-generator-interfacing applications", *Energies*, vol. 10, no. 7, pp. 1–23

[P2] Viinamäki, J., Jokipii, J., Suntio, T. (2016). "Improving double-line-frequency voltage ripple rejection capability of DC/DC converter in grid connected two-stage PV inverter using DC-link voltage feedforward", in *18th European Conference on Power Electronics and Applications, EPE'16 ECCE Europe*, pp. 1–10

[P3] Viinamäki, J., Jokipii, J., Suntio, T. (2015). "Effect of inductor saturation on the harmonic currents of grid-connected three-phase VSI in PV application", in *9th International Conference on Power Electronics - ECCE Asia, ICPE'16 ECCE Asia*, pp. 1–10

[P4] Viinamäki, J., Kivimäki, J., Suntio, T., Hietalahti, L. (2014). "Design of boost-power-stage converter for PV generator interfacing", in *16th European Conference on Power Electronics and Applications, EPE'14 ECCE Europe*, pp. 1–10

[P5] Viinamäki, J., Jokipii, J., Messo, T., Suntio, T., Sitbon, M., Kuperman, A. (2015)."'Comprehensive dynamic analysis of photovoltaic generator interfacing DC-DC boost power stage', *IET Renewable Power Generation*, vol. 9, no. 4, pp. 306–314

[P6] Suntio, T., Viinamäki, J., Jokipii, J., Messo, T., Kuperman, A. (2014). "Dynamic characterization of power electronic interfaces", *IEEE Journal of Emerging and Selected Topics in Power Electronics*, vol. 2, no. 4, pp. 949–961

1.9 The structure of the thesis

Chapter 2 focuses on the design of voltage-boosting dc-dc converter operating in grid-feeding mode. First, the small-signal model of the converter is presented. Next, the research on the component selection and control design of the converter is presented. Finally, the factors affecting the maximum attenuation of double-line-frequency voltage ripple, when using dc-link voltage feedforward are shown. Chapter 3 discusses the design of voltage-boosting dc-dc converter operating in grid-forming mode. After developing the small-signal model, the factors affecting the component selection and control design are presented. Chapter 4 discusses the effects of inductor saturation on the low-frequency and switching-frequency harmonics of the grid-connected three-phase PV inverter. Finally, the conclusions and suggested future topics are presented in Chapter 5.

2 DESIGN OF VOLTAGE-BOOSTING DC-DC CONVERTER OF TWO-STAGE PV INVERTER OPERATING IN GRID-FEEDING MODE

In this chapter, a small-signal model of voltage-boosting dc-dc converter operating as a part of two-stage PV inverter is developed. The properties of the PVG are taken into account in the model but the dc-ac inverter is neglected as the focus is on the dc-dc converter. The developed model is used in selecting the passive components of the converter as well as for studying the effect of using input-voltage control and dc-link voltage feedforward for attenuating double-line-frequency voltage ripple, which is present in single-phase PV inverter.

2.1 Small-signal modeling of switched-mode dc-dc converters

Small-signal model of a dc-dc converter can be developed using state space averaging method, which was introduced by Middlebrook in 70's (Cuk and Middlebrook, 1977; Middlebrook, 1988). In this method, the differential equations describing the averaged operation of the power circuit over a single switching period are linearized around a steady state operation point. The obtained model is accurate and valid up to half the switching frequency. The accuracy and simplicity are probably the main reasons for this method being so popular for modeling dc-dc converter dynamics. The linearized differential equations describing the power circuit can be presented in a general state-space form as

$$\begin{aligned} \frac{\mathrm{d}\hat{\boldsymbol{x}}(t)}{\mathrm{d}t} &= \mathbf{A}\hat{\boldsymbol{x}}(t) + \mathbf{B}\hat{\boldsymbol{u}}(t) \\ \hat{\boldsymbol{y}}(t) &= \mathbf{C}\hat{\boldsymbol{x}}(t) + \mathbf{D}\hat{\boldsymbol{u}}(t), \end{aligned} \tag{2.1}$$

where **A, B, C, D** are constant matrices, $\hat{\boldsymbol{u}}$ is the input vector, $\hat{\boldsymbol{y}}$ is the output vector and $\hat{\boldsymbol{x}}$ is the state vector. The linearized model can be transformed into the frequency domain by Laplace transform yielding

$$\begin{aligned} s\boldsymbol{X}(s) &= \mathbf{A}\boldsymbol{X}(s) + \mathbf{B}\boldsymbol{U}(s) \\ \boldsymbol{Y}(s) &= \mathbf{C}\boldsymbol{X}(s) + \mathbf{D}\boldsymbol{U}(s). \end{aligned} \tag{2.2}$$

The transfer function matrix $\mathbf{G}$ describing the relation between the input and output variables can be solved based on (2.2) as

$$\boldsymbol{Y}(s) = (\mathbf{C}(s\mathbf{I} - \mathbf{A})^{-1}\mathbf{B} + \mathbf{D})\boldsymbol{U}(s) = \mathbf{G}\boldsymbol{U}(s). \tag{2.3}$$

The inductor current and capacitor voltage are usually selected as state variables. The duty ratio is considered as control variable. The input variables are determined by the source and load of the converter. Those variables that do not belong in the above-mentioned groups are the output variables of the model. Thus, the input and output variables are application dependent. As shown in Fig. 2.1, four possible load/source configurations can be recognized: Voltage-fed voltage output (VF-VO), voltage-fed current output (VF-CO), current-fed current output (CF-CO) and current-fed voltage output (CF-VO) (Suntio, 2009; Suntio et al., 2014). The corresponding transfer function matrices are called G, Y, H, and Z-parameter sets, respectively.

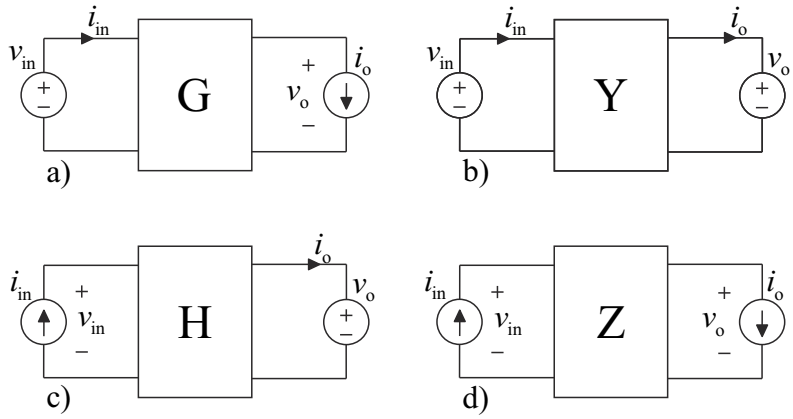

Fig. 2.1: Converter can be a) voltage-fed voltage output (VF-VO), b) voltage-fed current output (VF-CO), c) current-fed current output (CF-CO) and d) current-fed voltage output (CF-VO) .

When considering the VF-VO converter, the input voltage is determined by the voltage source and the load current is determined by the current sink. The value of the input voltage or output current cannot be affected by the duty cycle as they are determined externally. Thus, these variables are considered as inputs to the model, i.e., input vari-

ables. Input current and output voltage can be affected by varying the duty cycle or the input variables, so they are considered as output variables of the model.

G-parameters are used in conventional applications, where the converter is fed from a constant voltage source and the output voltage of the converter is to be regulated. In lighting application, the current of Light Emitting Diodes (LEDs) are controlled using dc-dc converter, which could be modeled using Y-parameter model. H-parameters are used in PV applications, where the PV generator voltage is to be controlled and the output voltage is determined by the battery or by the dc-ac inverter. Finally, Z-parameters can be used, when the PV interfacing converter is operating in grid-feeding mode, i.e., the dc-link voltage is controlled by the dc-dc converter instead of the dc-ac inverter.

2.2 H-parameter model of voltage-boosting dc-dc converter

The conventional voltage-boosting dc-dc converter can be used as PVG interfacing converter after addition of input capacitor as shown in Fig. 2.2. This topology can be used in medium-scale string-inverters when the galvanic isolation is not required. The main benefits of this topology are its reliability and ease of control due to low number of components. However, when the required voltage boosting capability is high or galvanic isolation is required, other topologies are commonly used (Forouzesh et al., 2017). The conventional voltage-boosting topology was used in this thesis due to its simplicity. In addition, the presented analysis can be used as a baseline for the analysis of more complicated topologies.

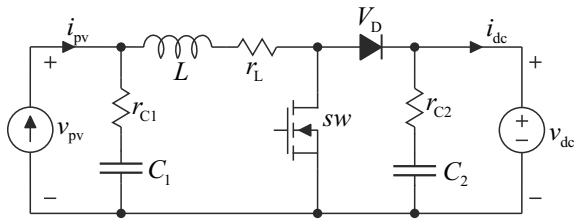

Fig. 2.2: voltage-boosting dc-dc converter

As the PVG is a nonlinear source having properties of voltage and current source, it might cause confusion which source type should be used in the small-signal model of the interfacing converter. The two-diode-model indicates that PVG is inherently a current source. In addition, as the PVG voltage is temperature dependent, it has much slower dynamics than the PVG current, which is directly dependent on solar irradiance. Because of this, usually the voltage of the PVG is controlled instead of the current. As the voltage is controlled, PVG shall be modeled as current source.

In the small-signal analysis of this thesis, it is assumed that the converter operates

at continuous conduction mode. In case of diode-switched converter, it means that the current of the energy transferring inductor is always higher than zero during the switching cycle. Using the symbols shown in Fig. 2.2, the linearized state-space model of the CF-CO voltage-boosting dc-dc converter is

$$\begin{bmatrix} \frac{\mathrm{d}\hat{i}_\mathrm{L}}{\mathrm{d}t} \\ \frac{\mathrm{d}\hat{v}_\mathrm{C1}}{\mathrm{d}t} \\ \frac{\mathrm{d}\hat{v}_\mathrm{C2}}{\mathrm{d}t} \end{bmatrix} = \begin{bmatrix} -\frac{R_\mathrm{eq}}{L} & \frac{1}{L} & 0 \\ -\frac{1}{C_1} & 0 & 0 \\ 0 & 0 & -\frac{1}{r_\mathrm{C2}C_2} \end{bmatrix} \begin{bmatrix} \hat{i}_\mathrm{L} \\ \hat{v}_\mathrm{C1} \\ \hat{v}_\mathrm{C2} \end{bmatrix} + \begin{bmatrix} \frac{r_\mathrm{C1}}{L} & -\frac{D'}{L} & \frac{V_\mathrm{eq}}{L} \\ \frac{1}{C_1} & 0 & 0 \\ 0 & \frac{1}{r_\mathrm{C2}C_2} & 0 \end{bmatrix} \begin{bmatrix} \hat{i}_\mathrm{pv} \\ \hat{v}_\mathrm{dc} \\ \hat{d} \end{bmatrix} \tag{2.4}$$

$$\begin{bmatrix} \hat{v}_\mathrm{pv} \\ \hat{i}_\mathrm{dc} \end{bmatrix} = \begin{bmatrix} -r_\mathrm{C1} & 1 & 0 \\ D' & 0 & \frac{1}{r_\mathrm{c2}} \end{bmatrix} \begin{bmatrix} \hat{i}_\mathrm{L} \\ \hat{v}_\mathrm{C1} \\ \hat{v}_\mathrm{C2} \end{bmatrix} + \begin{bmatrix} r_\mathrm{C1} & 0 & 0 \\ 0 & -\frac{1}{r_\mathrm{C2}} & -I_\mathrm{pv} \end{bmatrix} \begin{bmatrix} \hat{i}_\mathrm{pv} \\ \hat{v}_\mathrm{dc} \\ \hat{d} \end{bmatrix}, \tag{2.5}$$

where the constants R_eq and V_eq are given in (2.6) and (2.7). They are used to simplify the notation. The steady-state value of duty ratio D can be calculated as in (2.8). D' is the complement of the duty ratio and is calculated as $D' = 1 - D$.

$$R_\mathrm{eq} = r_\mathrm{C1} + r_\mathrm{L} + Dr_\mathrm{sw} + D'r_\mathrm{D} \tag{2.6}$$

$$V_\mathrm{eq} = [r_\mathrm{D} - r_\mathrm{sw}]\, I_\mathrm{pv} + V_\mathrm{dc} + V_\mathrm{D} \tag{2.7}$$

$$D' = \frac{V_\mathrm{pv} - (r_\mathrm{L} + r_\mathrm{sw})\, I_\mathrm{pv}}{V_\mathrm{D} + V_\mathrm{dc} + (r_\mathrm{D} - r_\mathrm{sw})\, I_\mathrm{pv}} \tag{2.8}$$

The transfer function set (2.9) describing the open-loop dynamics of the converter can now be solved by substituting the constant valued matrices from (2.4) and (2.5) to (2.3). The transfer functions are as given in (2.10)–(2.15) (Viinamäki, Jokipii, Messo, Suntio, Sitbon and Kuperman, 2015).

$$\begin{bmatrix} \hat{v}_\mathrm{pv} \\ \hat{i}_\mathrm{dc} \end{bmatrix} = \begin{bmatrix} Z^\mathrm{h}_\mathrm{in\text{-}o} & T^\mathrm{h}_\mathrm{oi\text{-}o} & G^\mathrm{h}_\mathrm{ci\text{-}o} \\ G^\mathrm{h}_\mathrm{io\text{-}o} & -Y^\mathrm{h}_\mathrm{o\text{-}o} & G^\mathrm{h}_\mathrm{co\text{-}o} \end{bmatrix} \begin{bmatrix} \hat{i}_\mathrm{pv} \\ \hat{v}_\mathrm{dc} \\ \hat{c} \end{bmatrix} \tag{2.9}$$

$$Z^{\mathrm{h}}_{\text{in-o}} = \frac{1}{\Delta}\frac{(R_{\mathrm{eq}} - r_{\mathrm{C1}} + sL)\,(1 + sr_{\mathrm{C1}}C_1)}{LC_1} \tag{2.10}$$

$$T^{\mathrm{h}}_{\text{oi-o}} = \frac{1}{\Delta}\frac{D'\,(1 + sr_{\mathrm{C1}}C_1)}{LC_1} \tag{2.11}$$

$$G^{\mathrm{h}}_{\text{ci-o}} = -\frac{1}{\Delta}\frac{V_{\mathrm{eq}}\,(1 + sr_{\mathrm{C1}}C_1)}{LC_1} \tag{2.12}$$

$$G^{\mathrm{h}}_{\text{io-o}} = \frac{1}{\Delta}\frac{D'\,(1 + sr_{\mathrm{C1}}C_1)}{LC_1} \tag{2.13}$$

$$Y^{\mathrm{h}}_{\text{o-o}} = \frac{D^{'2}s}{\Delta L} + \frac{sC_2}{1 + sr_{\mathrm{C2}}C_2} \tag{2.14}$$

$$G^{\mathrm{h}}_{\text{co-o}} = -\frac{I_{\mathrm{pv}}}{\Delta}\left(s^2 - s\left(\frac{D'V_{\mathrm{eq}}}{I_{\mathrm{pv}}L} - \frac{R_{\mathrm{eq}}}{L}\right) + \frac{1}{LC_1}\right), \tag{2.15}$$

where Δ is the denominator of the transfer functions and is given in (2.16). Roots of the denominator are the poles of the system and the number of the poles equals the degree of the system.

$$\Delta = s^2 + s\frac{R_{\mathrm{eq}}}{L} + \frac{1}{LC_1} \tag{2.16}$$

Ideal source and load are assumed in the presented small signal model. However, if the effect of the finite source or load impedance on the converter dynamics is of interest, they can be added to the model. In PV application, the output impedance of the PVG has significant effect on the dynamics of the converter suggesting that its effect shall be taken into account. The source-affected transfer functions are given in Appendix A. They are calculated by first adding the source admittance Y_{S} to the model as shown in Fig. A.1. Then, the input current is solved as $\hat{i}_{\mathrm{pv}} = \hat{i}_{\mathrm{pvS}} - Y_{\mathrm{S}}\hat{v}_{\mathrm{pv}}$ and it is substituted into (2.9).

The block diagram of the small-signal model of the converter operating under input-voltage control is presented for the input terminal in Fig. 2.3a and for the output terminal in Fig. 2.3b. $G^{\mathrm{h}}_{\text{se-in}}$ is the measurement gain, G_{a} is the modulator gain and G_{c} is the transfer function of the controller. When the controller is implemented digitally, e.g., by using Digital Signal Processor (DSP), the modulator and measurement gains can be manipulated to unity in in the code. However, as the measurement is usually filtered, its effect can be taken into account by including the filter pole into the measurement gain. The blocks inside the dashed line describe the dynamic model of the converter in open loop. The transfer function set describing the closed-loop small-signal model of the CF-CO converter is shown in Appedix A

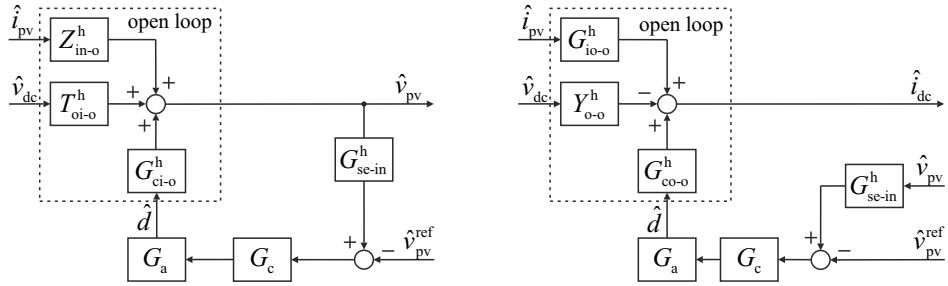

(a) Input terminal. **(b)** Output terminal.

Fig. 2.3: Control block diagram of the converter operating under input voltage control.

2.3 Hardware design of voltage-boosting dc-dc converter

The focus in this section is on the hardware design of voltage-boosting dc-dc converter operating as a part of two-stage PV inverter, when operating in grid-feeding mode. The design of the dc-ac inverter is left out from the analysis and the load of the converter is assumed to be constant voltage sink. First, the minimum and maximum values of the electrical quantities appearing at the terminals of the PVG are studied. Then, the selection of the passive components is studied by designing two example converters using different methods for calculating the input current. The calculated maximum input current and input voltage range of the converter are compared to the values given in the PV inverter manufacturer datasheets. Finally, the experimental evidence is provided by measuring the prototype converters.

2.3.1 Minimum and maximum values of the electrical quantities of a PVG

The SC current of the PVG can be approximated using (1.1) by neglecting the effect of series and parallel resistances and by taking into account that in SC the voltage in the terminals of the PVG is zero. In this case, the output current of the PVG equals the photocurrent I_{ph}. As the effect of ambient temperature on the SC current is very small, it can be neglected. Using the equation of photocurrent given in (Villalva et al., 2009) and the aforementioned assumptions, the SC current can be approximated as

$$I_{\mathrm{sc}} = I_{\mathrm{sc,stc}} \frac{G}{G_{\mathrm{stc}}}, \tag{2.17}$$

where $I_{\mathrm{sc,stc}}$ is the short-circuit current in STC, G is the solar irradiance on the surface of the panel, and G_{stc} is the solar irradiance in STC.

The OC voltage of the PVG can be approximated by using (1.1) by neglecting the effect of series and parallel resistances, the dependency of short-circuit current on temperature, and by recognizing that the current I_{pv} is zero at OC condition yielding

$$V_{\mathrm{oc}} = \ln\left(\frac{GI_{\mathrm{sc,stc}}}{G_{\mathrm{stc}}I_0} + 1\right)\frac{N_{\mathrm{s}}akT}{q}. \tag{2.18}$$

As the temperature T is in the numerator of (2.18), it might seem that higher temperature yields higher voltage. However, the temperature is also included in I_0 and actually lower temperature yields higher voltage as it was previously discussed. The calculation of the saturation current I_0 is presented in (Villalva et al., 2009).

The required maximum input voltage of the converter can be determined by calculating the maximum voltage present at the output terminals of the PVG using (2.18). The minimum input voltage can be determined by studying the MPP range of the PVG. The global MPP is located at the smallest voltage, when all other cell groups having bypass diode are shaded except one. In this case, other cell groups are bypassed by the bypass diode and only one cell group is producing power to the output terminal of the PVG. In this case, the minimum MPP voltage $V_{\mathrm{mpp,min}}$ can be calculated as

$$V_{\mathrm{mpp,min}} = \frac{V_{\mathrm{mpp,stc}} + (T_{\mathrm{max}} - T_{\mathrm{stc}})\,K_{\mathrm{v}}}{N_{\mathrm{bp}}} - (N_{\mathrm{BP}} - 1)\,V_{\mathrm{D}}, \tag{2.19}$$

where $V_{\mathrm{mpp,stc}}$ is the MPP voltage in STC, T_{max} is the maximum cell temperature, T_{stc} is the cell temperature in STC, K_{v} is the temperature coefficient of PVG voltage, V_{D} is the forward voltage drop of the bypass diode, and N_{bp} is the number of bypass diodes. According to (2.19), the minimum MPP voltage is obtained when the ambient temperature is at maximum value.

A single NP190GKg PV panel produced by NAPS was used as the source for both converters designed in this chapter. The electrical characteristics of the panel given in the datasheet are shown in Table 2.1. To calculate the values of the highest OC voltage and SC current, the values of solar irradiance and ambient temperature were collected from June 2011 to May 2012. The measurement system is located on the rooftop of the Department of Electrical Engineering at Tampere University of Technology. The highest peak in the OC voltage occurred on 5th of April 2012. The ambient temperature was 1.9 °C, solar irradiance 1400 W/m^2 and the calculated OC voltage was 35.4V. This was also the highest value of the solar irradiance during the measurement period. It was likely caused by the cloud enhancement and the result is consistent with the prior research (Luoma et al., 2012).

Table 2.1: Electrical characteristics of NAPS NP190GKg PV panel in STC.

Parameter	Value
$V_{\mathrm{oc,stc}}$	33.1 V
$I_{\mathrm{sc,stc}}$	8.02 A
$P_{\mathrm{mpp,stc}}$	190 W
$V_{\mathrm{mpp,stc}}$	25.9 V
$I_{\mathrm{mpp,stc}}$	7.33 A

The following parameter values were substituted into (2.19) to determine the minimum MPP voltage of NP190GKg PV panel: $T_{\max} = 60\,^{\circ}\mathrm{C}$, $N_{\mathrm{s}} = 54$, $N_{\mathrm{bp}} = 3$, $V_{\mathrm{D}} = 0.7$ V, $K_{\mathrm{v}} = -0.124$ V/°K. The value of temperature coefficient K_{v} was validated in the prior research (Maki and Valkealahti, 2012). The resulting voltage was 5.8 V. Finally, the maximum SC current was calculated using (2.17). As the highest peak in irradiance was 1400 W/m^2, the maximum SC current is approximately 1.4 times the SC current in STC, yielding 11 A.

As a summary, the relevant input voltage range for the interfacing converter connected to NP190GKg PV panel would be from 5.8 V to 36V when the target is to cover the whole MPP range. The maximum input current to the converter is 11 A.

2.3.2 Component sizing and design of input voltage controller

According to (Ho et al., 2012), the input current of interfacing converter in PV application is calculated by dividing the nominal power of the converter by minimum input voltage $V_{\mathrm{in,min}}$. Including the effect of the sizing factor determined in (1.3) yields

$$I_{\mathrm{in,max}} = \frac{P_{\mathrm{pvg,stc}} SR}{V_{\mathrm{in,min}}}. \tag{2.20}$$

Conventional rule-of-thumb is to downsize the inverter by setting the sizing factor to 0.7 (Chen et al., 2013). Using this value together with 5.8 V input voltage and 190 W power yields 23 A maximum input current. The calculated current is double the maximum value obtainable from the selected PV generator suggesting that this design method yields oversized components.

Several PV inverter datasheets were studied to find out how the input voltage range and maximum input current are selected in commercial devices. The maximum to minimum input voltage ratios are shown in Table 2.2. They are calculated by dividing the minimum input voltage by the maximum input voltage given in the datasheet. Also the normalized maximum input current is shown in Table 2.2. It is calculated by dividing the maximum current by the current obtained by dividing the nominal power of the

inverter by the minimum voltage. As it is shown, the PV inverter manufacturers seem to determine the maximum input current by dividing nominal power by the minimum input voltage, when the input voltage range is narrow. However, when the input voltage range is wide, a lower value of maximum current is used. The higher the voltage range, the lower the relative value of the maximum input current.

Table 2.2: Selection of input voltage and current range in commercial PV inverters.

	Micro inv 1	String inv 1	String inv 2
$V_{\mathrm{in,min}}$ (% of $V_{\mathrm{in,max}}$)	15	30	50
$I_{\mathrm{in,max}}$ (% of $P_{\mathrm{nom}}/V_{\mathrm{in,min}}$)	40	60	100

In order to study the effect of using (2.20) instead of the real maximum current of the PV panel in case of wide input voltage range, two converters were designed, the first one by using 23 A maximum input current and the second one by using 11 A maximum input current. They are named as conventional design (CD) and modified design (MD), respectively. This naming convention was selected as in conventional applications, where the converter is fed by a constant voltage source and the output voltage is regulated by the converter, the maximum input current of the converter is calculated by dividing the nominal power by the minimum input voltage. The input voltage range in both of the designed converters is from 5.8 V(16%) to 36V and the output voltage is 38 V. In practice, the dc-link voltage must be much higher. For example, in case of single-phase full-bridge inverter, the dc voltage must be higher than the peak of the grid voltage. However, as the voltage level does not affect the issues studied in this chapter, the low voltage level was used.

The inductor current ripple of voltage-boosting converter is maximized, when the input voltage is half the output voltage. Using this information together with the defining equation of the inductor, the required inductance can be approximated as

$$L \approx \frac{V_{\mathrm{dc}}}{4\Delta i_{\mathrm{L,pp}} f_{\mathrm{s}}}, \tag{2.21}$$

where $\Delta i_{\mathrm{L,pp}}$ is the peak-to-peak inductor current ripple, and f_{s} is the switching frequency. In most of the inductors used in power electronic devices, the inductance value is selected to limit the high-frequency ripple-current to a predefined value. However, also some alternative methods have been proposed (Reverter and Gasulla, 2017).

The inductance value was calculated using (2.21) to limit the current ripple to 10% of the maximum input current, when using 100 kHz switching frequency. The resulting values were 43 µH for conventional and 89 µH for modified designs. Metglas was used as a core material in both of the inductors. It is made of amorphous metal sheets having

high saturation flux density and low core losses. The inductors were designed following the procedure presented in (Bossche and Valchev, 2005). The summary of the main differences between the designed converters are shown in Table 2.3.

Table 2.3: Summary of the main differences between the designed converters.

	Conventional	Modified	Change (%)
Volume of the core (cm^3)	5.34	1.89	-65
Mass of the inductor copper (g)	29	31	7
Thermal resistance of the heat sink (K/W)	6.5	14.7	126
Capacitance of input capacitor (μF)	20	10	-50
Current rating of the connectors (A)	23	12	-48

The diode and the MOSFET were selected by calculating the total losses of several components and by selecting the type producing the lowest losses. The information about the losses was also used for sizing the heat sinks. In case of conventional design, the maximum power losses of the diode and the MOSFET were both calculated in the minimum input voltage condition (Ho et al., 2012). In reality, the power loss of the MOSFET is maximized in the minimum voltage condition, but the power loss of the diode is maximized at the MPP. This can be explained by considering the equation defining the RMS value of the diode current (Erickson and Maksimovic, 2006). At the MPP, the diode conducts longer than the MOSFET and the input current of the converter is large. When the input voltage decreases, the conduction time of the diode is also decreased and the power loss is smaller. For this reason, the power loss of the diode was calculated at the MPP in the modified design method.

As the input current is larger in conventional design compared to modified design, also the required heat sink of the MOSFET is larger. However, the size of the heatsink of the diode is the same in both designs. This is caused by the fact that in conventional design, the power loss of the diode is calculated incorrectly in minimum input voltage condition, whereas in modified design, the power loss is calculated at the MPP using more realistic value of current.

As shown in Table 2.3, the inductor core is much larger in the conventional design. The mass of the copper is slightly larger in modified design due to higher number of turns. The smaller thermal resistance means that the size of the heat sink is larger in the conventional design. The input capacitors were selected to have equal switching-frequency ripple component in the input voltage in both of the converters. As the difference in inductance is 50 %, also the difference in the input capacitance is 50 % in order to have equal HF ripple and resonance frequency. The capacitance value of the input capacitor was selected to be 10 μF and 20 μF in conventional and modified designs, respectively. These values are smaller than the recommended value (40 μF) in (Purhonen et al., 2012). However,

the measured switching-frequency ripple in the input voltage was 250 mV meaning that its effect on the MPPT efficiency is negligible.

The presented small-signal model of voltage-boosting converter was used for the control design and for selecting the input capacitor. The frequency response of the control-to-input-voltage transfer function including the effect of PV panel is shown in Fig. 2.4, when the parameters of the modified design are used. As it is shown, the peaking is stronger in CC region and the highest peaking occurs, when the input voltage is in minimum value.

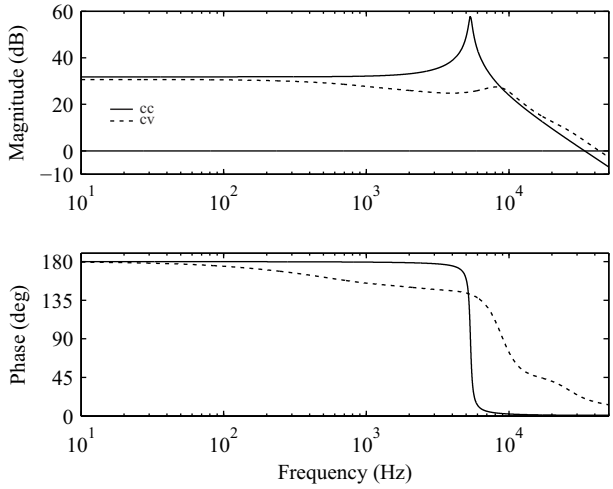

Fig. 2.4: Control-to-input-voltage transfer function including the effect of PV panel output impedance.

High resonant peaking is a consequence of small parasitic resistances in the circuit. On the other hand, the peaking is small in the CV region, because the small dynamic resistance of the PV panel attenuates the resonant peaking. A damping circuit consisting of series-connected resistor and capacitor was added in parallel with the input capacitor to enable stable operation also in CC region. According to Fig. 2.4, gain margin should be determined at the minimum input voltage and phase margin at the maximum input voltage to guarantee that the converter is stable at every operating point.

As it was previously discussed, the dc-link voltage of the two-stage single-phase inverter contains ripple component at double-line frequency. This ripple can be prevented from affecting the voltage of the PVG either by using dc-link voltage feedforward or input-voltage control in the voltage-boosting converter. The reverse voltage transfer ratio T_{oi} describes the relation between the dc-link voltage and the voltage of the PVG. In case of input-voltage-controlled converter, the reverse voltage transfer ratio is calculated as shown in (A.12). According to (A.12) the attenuation is high, when the loop gain is

high at double-line frequency.

The requirement for the control bandwidth of the input-voltage controller is determined by the MPPT. Fast MPPT requires high control bandwidth. In case of the converters designed in this chapter, it was assumed that the MPPT is slow and the control bandwidth can be below the resonant frequency. The shape of the loop gain is affected by the capacitance value of the input capacitor and by the controller. I-type controller was used and its parameters were selected by loop-shaping technique as a trade-off between high attenuation from output to input voltage, small capacitance of the input capacitor and adequate phase and gain margins.

2.3.3 Experimental evidence

The prototypes of the converters are shown in Fig. 2.5. As it is shown, the physical size of the conventional design is bigger than the modified design as expected. The size difference is clearest between the inductors, heatsinks of the MOSFET and the connectors. The circuit boards shown in Fig. 2.5 include only the power stage, driver and measurement circuit. The controller was placed on a separate circuit board and it was implemented by using digital signal processor TMS28335F from Texas Instruments.

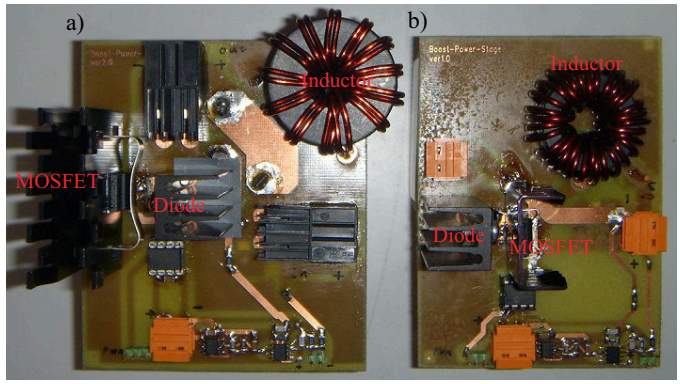

Fig. 2.5: The prototypes of a) conventional and b) modified designs.

The parameter values of the converters are presented in Table 2.4, where the symbols refer to Fig. 2.2. As shown, the capacitance of the input capacitor and the inductance of the inductor are dependent on the operating point, whereas other parameters are constant. The capacitance value of the input capacitor is dependent on input voltage, because ceramic capacitor was used. The inductance of the inductors dropped steeper as a function of bias current than it was expected based on datasheet. In order to have enough inductance at maximum current, two similarly designed inductors were connected in series. As the input current is much lower than the maximum current at the operating

points where the measurements were made, the inductance values in Table 2.4 are higher than the required values 43 µH and 89 µH. The dependency of the inductance on the bias current can be reduced by using discrete air gap.

Table 2.4: Parameter values of the prototype converters.

Parameter	L_1 (µH)	r_{L1} (mΩ)	C_1 (µF)	r_{C1} (mΩ)	C_2 (µF)	r_{C2} (mΩ)	V_D (V)	r_D (mΩ)	r_{sw} (mΩ)
Conventional (CC)	69	6.4	16	4	52	120	0.39	100	20
Conventional (CC)	85	6.4	6.6	4	52	120	0.39	100	20
Modified (CC)	110	19.7	8	4	52	120	0.39	100	20
Modified (CC)	173	19.7	3.3	4	52	120	0.39	100	20

The measurements were made by using Agilent E4360A Solar Array Simulator (SAS) as a source emulating single Naps NP190GKg PV panel. The accuracy of this emulator for emulating the dynamic behavior of the selected PV panel has been shown to be sufficient for these type of measurements in (Nousiainen et al., 2013). The load was series connection of three 12 V batteries parallel to Programmable DC load Chroma 63103A operating in current sink mode. The measurements were repeated in CC and CV regions and at the MPP. The corresponding operating points were 5V/7.98A, 31V/2.6A, and 25.9V/7.33A.

Thermal images of the converters operating at the MPP are shown in Fig. 2.6. These images were taken using NEC TH7800 Thermo Tracer. The temperature scales in the images are different from each other. The red color in Fig. 2.6a corresponds to white color in Fig. 2.6b.

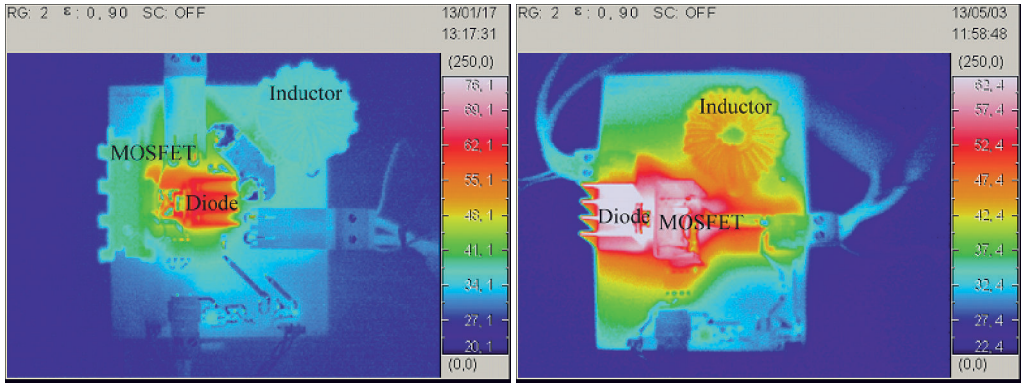

(a) Conventional design. **(b)** Modified design.

Fig. 2.6: Thermal images of the power stages, when operating at the MPP in STC.

According to Fig. 2.6, the temperature of the diode is around 62 °C in both of the converters as expected, because the heat sinks are identical. However, as the heat sink of

the MOSFET is much larger in the conventionally designed converter, it is running cooler similarly as the inductor. The temperature distribution is non-uniform in conventionally designed converter, because the diode is running much hotter than other components. On the other hand, the modified design method yields a more uniform temperature distribution having the same maximum value of the temperature as in the conventionally designed converter.

The higher temperature of the inductor in the modified design indicates that the power losses are higher compared to the conventional design. The total efficiency of the converter was measured and reported in (Viinamaki et al., 2014). According to the measurements, the efficiency is approximately 0.4 p.u. lower at the MPP in the modified design compared to the conventional design. This is the main disadvantage of the modified design method.

The measured input-voltage loop gain and the closed-loop reverse voltage transfer functions are shown in Figs. 2.7 and 2.8, respectively. They were measured by using the frequency response analyzer Model 3120 by Venable Instruments. According to Fig. 2.7, the minimum gain margin is 11 dB and the minimum phase margin is 82 ° in both of the converters. The resonance peak is sufficiently attenuated by the damping circuit.

According to Fig. 2.8, the attenuation at the double-line frequency is 13 to 25 dB depending on the operating point. Higher attenuation can be obtained by using PID controller having bandwidth over the resonance instead of low-bandwidth I controller. In this case, also the damping circuit can be removed. However, the crossover frequency should be approximately one decade higher than the resonant frequency to obtain adequate phase and gain margins. In addition, if the crossover frequency is close to resonance, the phase and gain margins are more dependent on the operating point, especially, when the parameter values are highly dependent on the operating point (see Table 2.4). In this case, it might be compulsory to increase the inductance value or capacitance value of the input capacitor to decrease the resonant frequency to obtain good gain and phase margins by using reasonably low crossover frequency.

As the phase and gain margins and attenuation at double-line frequency are equal in both converters, it can be concluded that the the same dynamic performance can be obtained using either of these design methods and still the modified design method yield material savings according to Table 2.3.

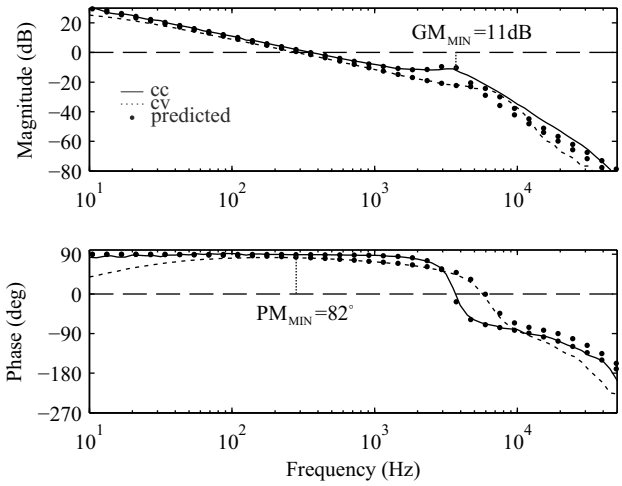

(a) Conventional design.

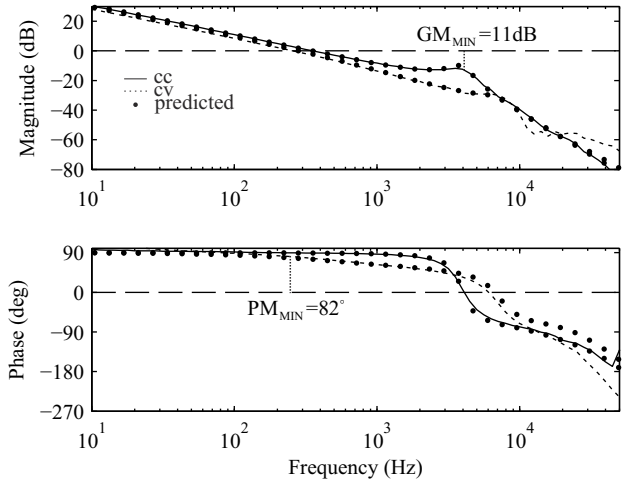

(b) Modified design.

Fig. 2.7: Measured and predicted loop gains of the converters.

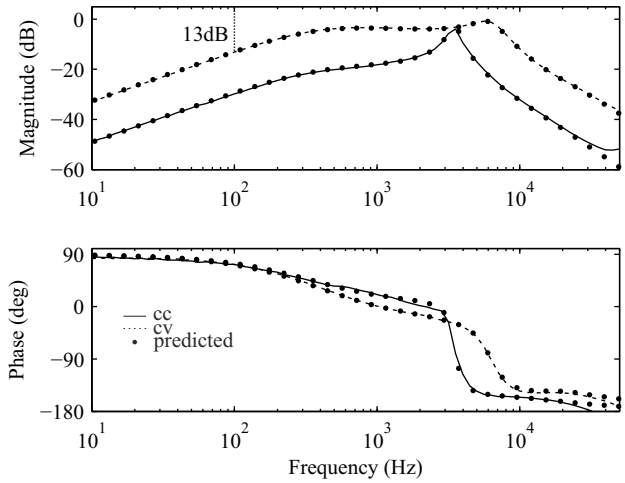

(a) Conventional design.

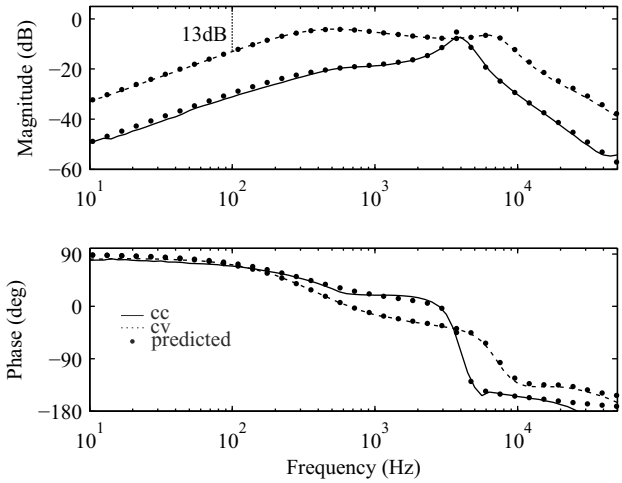

(b) Modified design.

Fig. 2.8: Measured and predicted closed-loop reverse voltage transfer ratios of the converters.

2.4 Using dc-link voltage feedforward to attenuate double-line-frequency voltage ripple

In this section, the effect of dc-link-voltage feedforward on dynamics of the voltage-boosting dc-dc converter is studied by using small signal model. The developed model is used to study the factors affecting the maximum obtainable attenuation of double-line-frequency ripple present in single-phase inverter. The following analysis was presented in (Viinamaki et al., 2016) by the author.

2.4.1 Effect of dc-link voltage feedforward on the dynamics of voltage-boosting dc-dc converter

The effect of dc-link voltage feedforward on the dynamic characteristics of voltage-boosting dc-dc converter can be studied by adding feedforward path to the block diagram of open loop small-signal model as shown in Fig. 2.9. $G^{\mathrm{h}}_{\mathrm{se\text{-}o}}$ is the measurement gain of dc-link voltage and G_{ff} is the feedforward gain. The control variable is now $\hat{v}_{\mathrm{co}}$ instead of $\hat{d}$.

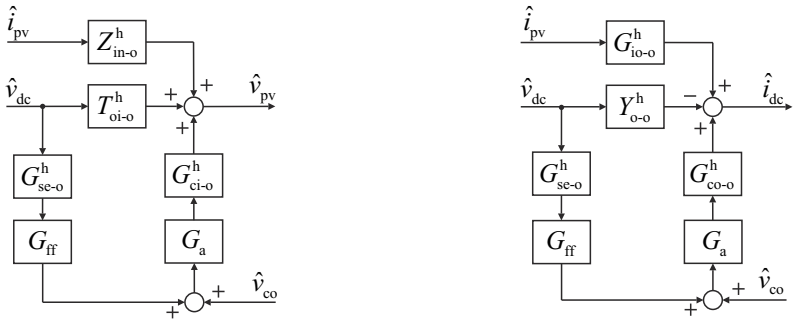

(a) Input terminal. **(b)** Output terminal.

Fig. 2.9: Control block diagram when using dc-link-voltage feedforward.

The transfer functions describing the feedforward-affected open-loop dynamics of the converter can be determined based on the block diagram shown in Fig. 2.9, as given in (2.22). The feedforward affects the reverse voltage transfer ratio and the output impedance. Control-to-input and control-to-output transfer functions are only scaled by the modulator gain.

$$\begin{bmatrix} \hat{v}_{\mathrm{pv}} \\ \hat{i}_{\mathrm{dc}} \end{bmatrix} = \begin{bmatrix} Z_{\mathrm{in\text{-}o}}^{\mathrm{h\text{-}ff}} & T_{\mathrm{oi\text{-}o}}^{\mathrm{h\text{-}ff}} & G_{\mathrm{ci\text{-}o}}^{\mathrm{h\text{-}ff}} \\ G_{\mathrm{io\text{-}o}}^{\mathrm{h\text{-}ff}} & -Y_{\mathrm{o\text{-}o}}^{\mathrm{h\text{-}ff}} & G_{\mathrm{co\text{-}o}}^{\mathrm{h\text{-}ff}} \end{bmatrix} \begin{bmatrix} \hat{i}_{\mathrm{pv}} \\ \hat{v}_{\mathrm{dc}} \\ \hat{v}_{\mathrm{co}} \end{bmatrix}$$
$$= \begin{bmatrix} Z_{\mathrm{in\text{-}o}}^{\mathrm{h}} & T_{\mathrm{oi\text{-}o}}^{\mathrm{h}} + G_{\mathrm{ci\text{-}o}}^{\mathrm{h}} G_{\mathrm{a}} G_{\mathrm{se\text{-}o}}^{\mathrm{h}} G_{\mathrm{ff}} & G_{\mathrm{ci\text{-}o}}^{\mathrm{h}} G_{\mathrm{a}} \\ G_{\mathrm{io\text{-}o}}^{\mathrm{h}} & Y_{\mathrm{o\text{-}o}}^{\mathrm{h}} - G_{\mathrm{co\text{-}o}}^{\mathrm{h}} G_{\mathrm{a}} G_{\mathrm{se\text{-}o}}^{\mathrm{h}} G_{\mathrm{ff}} & G_{\mathrm{co\text{-}o}}^{\mathrm{h}} G_{\mathrm{a}} \end{bmatrix} \begin{bmatrix} \hat{i}_{\mathrm{pv}} \\ \hat{v}_{\mathrm{dc}} \\ \hat{v}_{\mathrm{co}} \end{bmatrix} \tag{2.22}$$

The target is to prevent the double-line-frequency voltage ripple from affecting the PVG voltage. The attenuation from dc-link voltage to PVG voltage is maximized, when the magnitude of reverse voltage transfer ratio is zero as

$$T_{\mathrm{oi\text{-}o}}^{\mathrm{h}} + G_{\mathrm{ci\text{-}o}}^{\mathrm{h}} G_{\mathrm{a}} G_{\mathrm{se\text{-}o}}^{\mathrm{h}} G_{\mathrm{ff}} = 0. \tag{2.23}$$

The required feedforward gain can now be solved by substituting (2.11) and (2.12) to (2.23). When assuming unity modulator and measurement gains, the required feedforward gain is

$$G_{\mathrm{ff}} = \frac{V_{\mathrm{pv}}}{V_{\mathrm{dc}}^2} \frac{1 - \frac{(r_{\mathrm{L}}+r_{\mathrm{sw}})I_{\mathrm{pv}}}{V_{\mathrm{pv}}}}{1 + \frac{2V_{\mathrm{dc}}V_{\mathrm{D}} + 2V_{\mathrm{dc}}(r_{\mathrm{D}}-r_{\mathrm{sw}})I_{\mathrm{pv}} + V_{\mathrm{D}}^2 + 2V_{\mathrm{D}}(r_{\mathrm{D}}-r_{\mathrm{sw}})I_{\mathrm{pv}} + ((r_{\mathrm{D}}-r_{\mathrm{sw}})I_{\mathrm{pv}})^2}{V_{\mathrm{dc}}^2}}. \tag{2.24}$$

The feedforward gain is presented in (2.24) by separating the term $V_{\mathrm{pv}}/V_{\mathrm{dc}}^2$. This term is called here an ideal feedforward gain, because it would yield infinite attenuation in case of a lossless converter. The remaining part in (2.24) includes the parasitic elements. As it would be difficult to include all these parasitic elements in practical implementation of feedforward, ideal feedforward gain is used in practice. However, as the real converter includes losses, the resulting reverse voltage transfer function is not zero, i.e., the attenuation is not infinite. This loss-affected attenuation can be calculated by substituting the ideal feedforward gain, (2.11), and (2.12) into (2.22) yielding

$$T_{\mathrm{oi\text{-}o}}^{\mathrm{h\text{-}ff}} = T_{\mathrm{oi\text{-}o}}^{\mathrm{h}} + G_{\mathrm{ci\text{-}o}}^{\mathrm{h}} G_{\mathrm{ff}}^{\mathrm{h}} = \frac{1 + sr_{\mathrm{C1}}C_1}{\Delta L C_1} \left(D' - V_{\mathrm{eq}} \frac{V_{\mathrm{pv}}}{V_{\mathrm{dc}}^2} \right). \tag{2.25}$$

The effect of feedforward on the reverse-voltage transfer function can be studied in a frequency range from low frequencies up to half the switching frequency by using (2.25). It is useful as the dc-link voltage might include also higher frequency components to

be attenuated. The effect of parameter variation on double-line-frequency attenuation is studied in the next section. Thus, (2.25) is further simplified by approximating its low-frequency value by setting s=0 resulting (2.26).

$$\begin{aligned} T_{\text{oi-o}}^{\text{h-ff-lf}} &= D' - V_{\text{eq}} \frac{V_{\text{pv}}}{V_{\text{dc}}^2} \\ &= \frac{V_{\text{dc}}^2 \left(V_{\text{pv}} - (r_{\text{L}} + r_{\text{sw}})\, I_{\text{pv}}\right) - V_{\text{pv}} \left(V_{\text{dc}} + V_{\text{D}} + (r_{\text{D}} - r_{\text{sw}})\, I_{\text{pv}}\right)^2}{V_{\text{dc}}^2 \left(V_{\text{dc}} + V_{\text{D}} + (r_{\text{D}} - r_{\text{sw}})\, I_{\text{pv}}\right)} \end{aligned} \tag{2.26}$$

The effect of dc-link voltage feedforward on the output impedance of the converter is of interest as the output impedance affects the dc-link-voltage control loop in a two-stage PV inverter (Messo et al., 2014). The low-frequency value of the feedforward-affected output impedance can be calculated by first substituting the ideal feedforward gain, (2.14) and (2.15) to (2.22), then setting s=0 yielding

$$Y_{\text{o-o}}^{\text{h-ff-lf}} = \frac{I_{\text{pv}} V_{\text{pv}}}{V_{\text{dc}}^2} = \frac{I_{\text{pv}} D'}{V_{\text{dc}}} = \frac{I_{\text{dc}}}{V_{\text{dc}}} \implies Z_{\text{o-o}}^{\text{h-ff-lf}} = \frac{V_{\text{dc}}}{I_{\text{dc}}}. \tag{2.27}$$

As it was mentioned earlier, the output impedance of PV generator is operation-point dependent and it affects the dynamics of the interfacing converter. The equations for including the effect of source admittance on the h-parameter set are shown in Appendix A. The source-affected output admittance can be calculated as

$$Y_{\text{o}}^{\text{hS}} = \frac{1 + Y_{\text{s}} \left(Z_{\text{in}}^{\text{h}} + \frac{G_{\text{io}}^{\text{h}} T_{\text{oi}}^{\text{h}}}{Y_{\text{o}}^{\text{h}}}\right)}{1 + Y_{\text{s}} Z_{\text{in}}^{\text{h}}} Y_{\text{o}}^{\text{h}}, \tag{2.28}$$

where Y_{s} is the source admittance, which in this case is the output admittance of the PVG. When the dc-link feedforward is used, the magnitude of the reverse voltage transfer function is small, implicating that the factor multiplied with Y_{o}^{h} is close to unity and $Y_{\text{o}}^{\text{hS}} \approx Y_{\text{o}}^{\text{h}}$. Thus, according to (2.27), the source-affected output impedance depends only on the dc-link voltage and current, i.e., the converter has constant power output similarly as in case of input-voltage-controlled converter (Messo et al., 2012). This property of the converter effectively removes the right-half-plane (RHP) pole existing in the control dynamics of the dc-link-voltage control of the inverter caused by the PVG. As the RHP pole is removed, there is no lower limit for the crossover frequency of the dc-link voltage loop of the inverter. If no feedforward or input-voltage control is used, the stable operating range of the inverter is limited, because the crossover frequency of the dc-link-voltage control loop must be higher than the frequency of the RHP pole.

In case of voltage-boosting converter, the conventional method to implement dc-link voltage feedforward is based on the equation of steady-state duty cycle D. Instead of using constant values, when calculating the duty cycle, the measured value of the dc-link voltage is used. By neglecting the losses, the average value of the duty cycle is

$$d = 1 - \frac{\langle v_{\mathrm{c}} \rangle}{\langle v_{\mathrm{dc}} \rangle}, \tag{2.29}$$

where v_{c} is the desired value of the PVG voltage and v_{dc} is the measured dc-link voltage. Linearization of (2.29) yield

$$\hat{d} = -\frac{1}{V_{\mathrm{dc}}}\hat{v_{\mathrm{c}}} + \frac{V_{\mathrm{c}}}{V_{\mathrm{dc}}^2}\hat{v}_{\mathrm{dc}} = q_{\mathrm{o}}\hat{v_{\mathrm{c}}} + G_{\mathrm{ff}}\hat{v}_{\mathrm{dc}}. \tag{2.30}$$

By comparing (2.30) to (2.24) and the block digram in Fig. 2.9, it can be noted that the conventional method produces ideal feedforward gain and its dynamic effect is as in Fig. 2.9, when assuming unity modulator gain and when $v_{\mathrm{co}} = q_{\mathrm{o}} v_{\mathrm{c}}$. Thus, the presented analysis is valid, when using conventional implementation of voltage feedforward.

2.4.2 Effect of parameter variation on low-frequency ripple attenuation

The effect of parameter variation on the performance of dc-link-voltage feedforward was studied numerically using the parameter values of the converter designed in the previous chapter. The low-frequency magnitude of reverse-voltage transfer function is shown in Fig. 2.10 as a function of measurement gain $G_{\mathrm{se\text{-}o}}$.

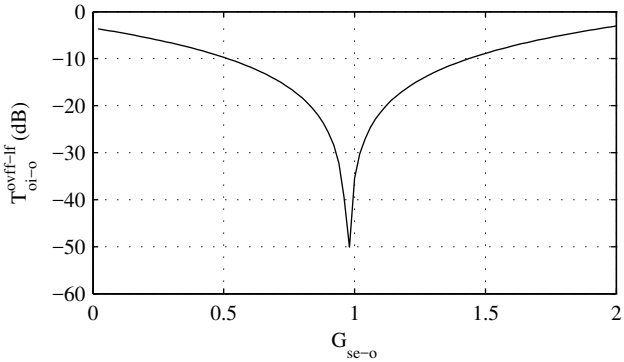

Fig. 2.10: The effect of measurement gain on the magnitude of reverse voltage transfer ratio, when $V_{\mathrm{pv}} = 25.9$ V and $V_{\mathrm{dc}} = 38$ V.

Fig. 2.10 is plotted using (2.26), when the operating point is at the MPP and the dc-link voltage is 38 V. The deviation from unity can be considered as a measurement error. The attenuation is approximately 35 dB, when there is no measurement error, i.e., measurement gain is unity. The attenuation might increase or decrease depending on the sign of the measurement error. This is caused by the fact that the measurement error can compensate the difference between (2.24) and the ideal feedforward gain. However, as the sign of the measurement error is usually not known, the error should be minimized.

The low-frequency magnitude of reverse-voltage transfer function is visualized in Figs. 2.11 and 2.12 as a function of parasitic resistances of the switch and the diode. The voltage levels of the PVG and the dc-link are higher in Fig. 2.12. As it is shown, the attenuation is clearly higher in the case of higher dc-link voltage. This is consistent with the fact that the exponent of of dc-link voltage in the denominator of (2.26) is larger than of the other terms in the equation. The shape of the surface is quite similar in Figs. 2.11 and 2.12.

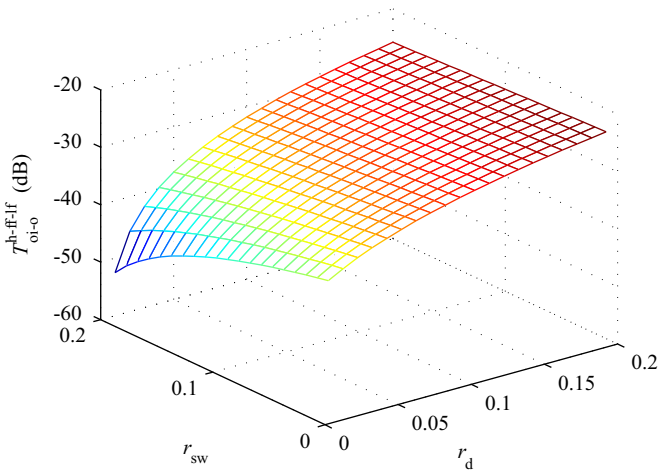

Fig. 2.11: The effect of parasitic resistances on the magnitude of reverse voltage transfer ratio, when $V_{\text{pv}} = 25.9$ V and $V_{\text{dc}} = 38$ V.

The presented small-signal model can also be used for studying the synchronous voltage-boosting converter. Assuming equal upper and lower switches ($V_{\text{D}} = 0$, $r_{\text{D}} = r_{\text{sw}}$), (2.26) reduces to

$$T_{\text{oi-o}}^{\text{ff-lf-sync}} = \frac{-\left(r_{\text{L}} + r_{\text{sw}}\right) I_{\text{pv}}}{V_{\text{dc}}}. \tag{2.31}$$

According to (2.31), the attenuation is maximized, when the dc-link voltage is maximized

and the parasitic resistances of the switches and inductor are minimized. The illustration is shown in Fig. 2.13, where (2.31) is used to plot the low-frequency magnitude of reverse voltage transfer function in case of synchronous converter and dc-link voltage of 700 V. As a conclusion, the highest attenuation for double-line frequency is obtained by using as high dc-link voltage as possible, by minimizing the parasitic resistances of the switches and inductor as well as using a synchronous converter instead of diode-switched converter.

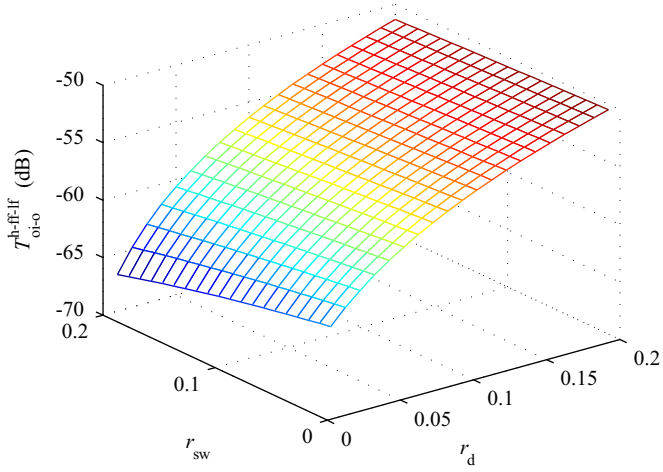

Fig. 2.12: The effect of parasitic resistances on the magnitude of reverse voltage transfer ratio, when $V_{pv} = 400$ V and $V_{dc} = 700$ V.

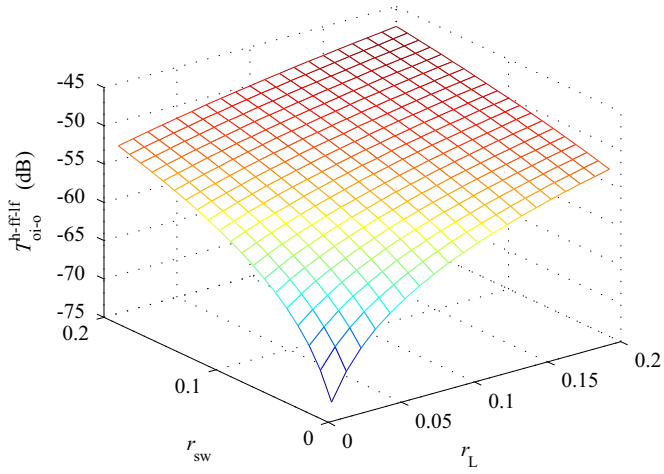

Fig. 2.13: The effect of parasitic resistances on the magnitude of reverse voltage transfer ratio, when $V_{pv} = 400$ V and $V_{dc} = 700$ V in case of synchronous converter.

2.4.3 Experimental evidence

The presented small-signal model was verified by measurements using the same converter hardware and measurement setup as in the previous section. However, the input voltage control was disabled and the dc-link-voltage feedforward was implemented digitally inside the DSP. Before feeding the measured dc-link voltage into the DSP, it was filtered by using a first-order low-pass filter having crossover frequency at 10.6 kHz. The effect of this filter was included in the model. The measurements were repeated in CC and CV regions and at the MPP. The corresponding operating points were 5V/7.98A, 31V/2.6A, and 25.9V/7.33A.

The measured and predicted reverse voltage transfer functions are as shown in Fig. 2.14, when operating at the MPP. The black curve is measured, when the feedforward is disabled and the red curve, when it is enabled. As shown, the magnitude is approximately 30 dB smaller at low frequencies, when the feedforward is enabled. At frequencies higher than 100 Hz, the low-pass filtering of the dc-link voltage starts to weaken the effect of feedforward. When the prediction is plotted without the effect of the filter, the attenuation does not decrease at high frequencies. It seems that the feedforward is sensitive to the phase difference caused by the filter. However, when using high enough crossover frequency in the filter, the attenuation at double-line frequency is not significantly affected.

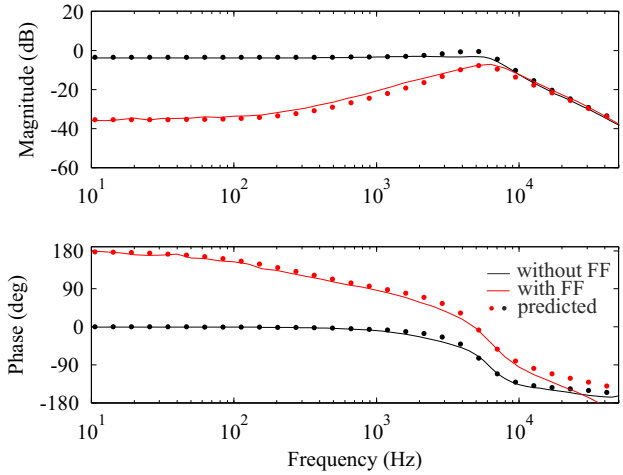

Fig. 2.14: Measured and predicted open-loop reverse voltage transfer ratio, when operating at the MPP with and without output-voltage feedforward.

The reverse voltage transfer function was measured also in CC and CV regions, when the feedforward was enabled and the result is shown in Fig. 2.15. As it is shown, the magnitude at double-line frequency is approximately -35 dB at all the measured operating points. There is also a good match between the measured and predicted curves. The difference in the phase curves at the high frequencies is caused by the control delay of the DSP, which was not modeled.

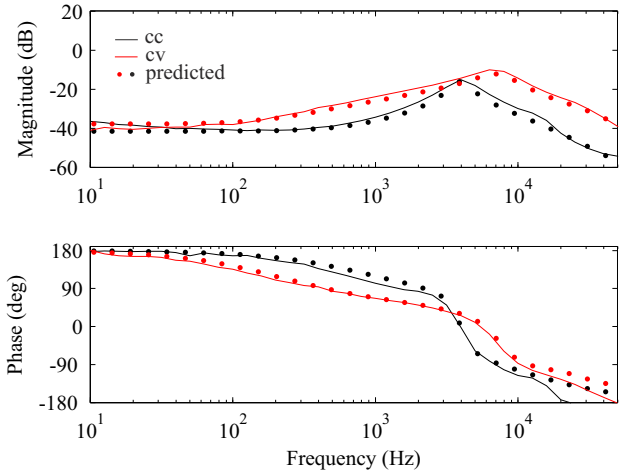

Fig. 2.15: Measured and predicted open-loop reverse voltage transfer ratio, when operating in CC and CV regions and using output-voltage feedforward.

The measured and predicted output impedances of the prototype converter are shown in Fig. 2.16. Black, blue and red lines indicate the operation in CC and CV regions and at the MPP, respectively. According to Fig. 2.16a, the output impedance of the converter is affected by the operating-point-dependent impedance of the PV generator, when operating in open loop. When the dc-link-voltage feedforward is enabled, the output impedance becomes a function of ouput power of the converter as shown in Fig. 2.16b. The output power is approximately 40 W, 80 W, and 190 W at the measured operating points in the CC and CV regions and at the MPP, respectively. Calculating the low-frequency output impedance values using (2.27) yields 36 Ω, 18 Ω and 7.6 Ω for CC, CV and MPP, respectively. These values match well with Fig. 2.16b verifying the analysis.

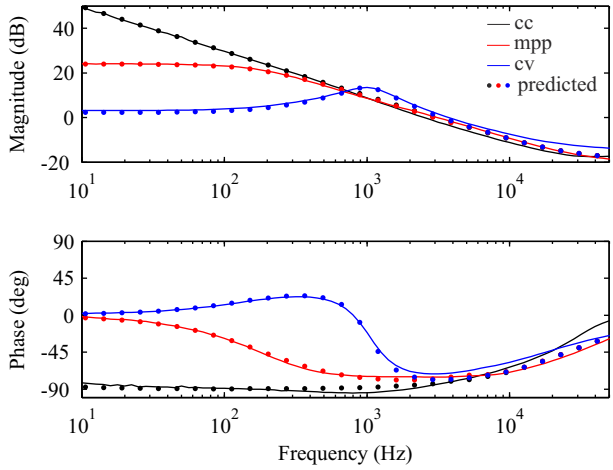

(a) Feedforward is not in use.

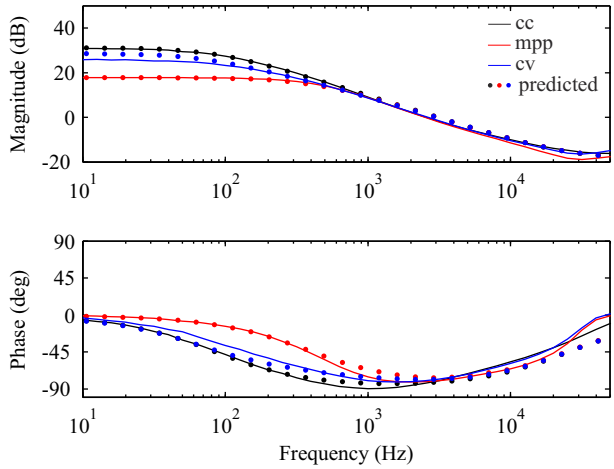

(b) Feedforward is in use.

Fig. 2.16: Measured and predicted output impedance of the converter.

Finally, the effect of voltage feedforward on the attenuation of double-line frequency voltage ripple was demonstrated by time-domain measurements. Sinusoidal voltage was summed to the dc-link voltage by connecting a linear amplifier in series with the load. The reference signal for the amplifier was generated by a signal generator. By comparing Figs. 2.17a and 2.17b, it can be seen that the addition of dc-link-voltage feedforward effectively prevents the double-line-frequency ripple of the dc-link voltage to affect the PVG voltage.

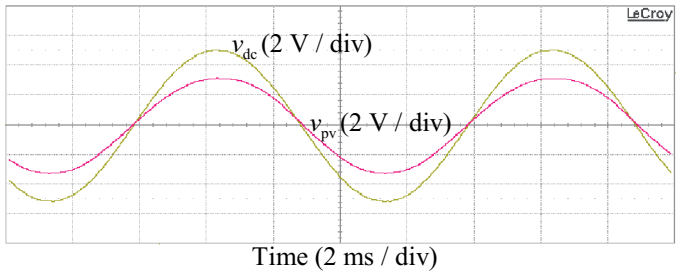

(a) Feedforward is not in use.

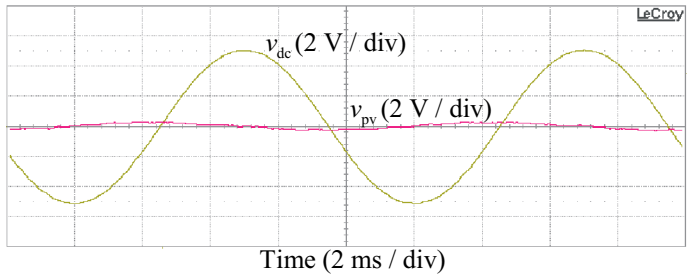

(b) Feedforward is in use.

Fig. 2.17: Measured low-frequency voltage ripple in dc-link and PV voltage.

2.5 Conclusions

The properties of the PVG were studied to find analytical equations for the maximum OC voltage, minimum MPP voltage and the maximum SC current. These equations, together with the measurement data on solar irradiance and ambient temperature, were used to calculate the required input voltage and current ranges of the interfacing converter. It was shown that the maximum SC current available from the PVG is approximately 1.4 times the SC current in STC. If the partial shading is taken into account, the minimum MPP voltage occurs, when only one PV cell group is producing current to the output and other groups are shaded. The maximum OC voltage was found to occur in April, when the ambient temperature was 1.9 °C and the solar irradiance was 1400 W/m^2. These values give good approximation, when the PVG is located in Finland or in other Nordic countries.

The design of the voltage-boosting dc-dc converter of two-stage PV inverter was studied. The PV inverter was assumed to operate in grid-feeding mode meaning that the dc-link voltage is controlled by the dc-ac inverter and the voltage of the PVG is controlled by the dc-dc converter. The dc-ac inverter was left out from the analysis as the focus was on the dc-dc converter.

Two interfacing converters were designed for Naps NP190GKg PV panel to study

the component sizing. In the conventionally designed converter, the maximum input current of the converter was calculated by dividing the nominal power of the converter by the minimum input voltage. In the other converter (modified design), the maximum input current was determined by using the real maximum current of the PV panel. In addition, the power losses of the diode were calculated in the minimum-input-voltage condition in case of conventional design, and at the MPP in case of the modified design. According to the investigations, using modified design instead of conventional design in case of wide input-voltage range yields smaller inductor core, smaller heat sink of the MOSFET, smaller input capacitor and more even temperature distribution.

A small-signal model of voltage-boosting converter having dc-link-voltage feedforward was developed. The developed model was used to study the effect of feedforward on the attenuation of double-line-frequency voltage ripple from the dc-link to the PVG. It was shown, that the highest attenuation is obtained by using as high dc-link voltage as possible, minimized parasitic resistances of the switches and inductor and using synchronous converter instead of diode-switched converter. In addition, when using dc-link-voltage feedforward, the output impedance of the converter depends only on the dc-link voltage and current, i.e., the converter has constant power output similarly as in case of input-voltage-controlled converter. When considering the two-stage PV inverter, this property of the converter removes the right-half-plane (RHP) pole existing in the control loop of the dc-ac inverter. As the control bandwidth of the inverter must be higher than the frequency of this RHP pole, there is no such restriction, when using dc-link-voltage feedforward.

3 DESIGN OF VOLTAGE-BOOSTING DC-DC CONVERTER OF TWO-STAGE PV INVERTER OPERATING IN GRID-FORMING MODE

In this chapter, a small-signal model of voltage-boosting dc-dc converter operating as a part of two-stage PV inverter is developed, when the inverter is operating in grid-forming mode. This means that the dc-link voltage is controlled by the dc-dc converter. The properties of the PVG are taken into account but the dc-ac inverter is neglected similarly as in the previous chapter. The model is used for studying the dynamic properties of the converter affecting the control design and component selection. The material presented in this chapter is based on (Viinamäki et al., 2017).

3.1 Small-signal modeling of the converter

In Chapter 2, the small-signal model of the voltage-boosting converter was developed for grid-feeding operation. In this case, the PVG was modeled as a current source, because the voltage of the PVG was controlled. Furthermore, as the dc-link voltage was controlled by the inverter, the load was modeled as constant voltage sink. Contrary to this, in grid-forming operation, the load of the converter is modeled as a constant current sink, because the dc-link voltage is controlled by the converter. Another major difference is that the voltage or current of the PVG is not controlled by the converter. This suggests that the PVG can be modeled either as a current source or a voltage source for determining the control-to-output transfer function used in the control design. For this reason, the small-signal model of the converter is developed by using current source (z-parameter model) and voltage source (g-parameter model) and their differences are studied.

The topology of the studied converter is the same as in Chapter 2. Only the source and load are different due to different control schemes as shown in Fig. 3.1. The developed small-signal models are used for studying the dynamics of the converter in grid-forming operation. Special attention is paid to the existence of RHP zeros as they have major effect on the control design. According to control engineering principles, the bandwidth of the control loop must be limited to lower than the frequency of the RHP zero or zeros to obtain stable control loop.

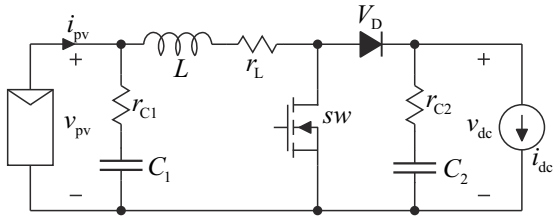

Fig. 3.1: Voltage-boosting dc-dc converter in grid-forming mode.

3.1.1 G-parameter model

The g-parameter model of the converter is shown in Appendix B. The open-loop transfer functions together with the steady-state operating point are presented in symbolic form in (B.1)-(B.14) when assuming ideal voltage source. The effect of nonzero impedance of the source can be included into the model by calculating as shown in (B.15)-(B.23). The transfer functions describing the dynamics after closing the dc-link-voltage control loop can be calculated using (B.24)-(B.32). According to (B.7), the numerator of the control-to-output transfer function is

$$G^{\mathrm{g}}_{\text{co-o-num}} = \frac{I_{\mathrm{pv}}}{LC_2}\left(\frac{D'V^{\mathrm{g}}_{\mathrm{eq}}}{I_{\mathrm{pv}}} - R^{\mathrm{g}}_{\mathrm{eq}} - sL\right)(1 + sr_{\mathrm{C2}}C_2)\,, \tag{3.1}$$

when assuming ideal voltage source. As it is shown, there is one RHP zero at

$$\omega^{\mathrm{g}}_{\mathrm{RHP-zero1}} = \frac{D'V^{\mathrm{g}}_{\mathrm{eq}} - I_{\mathrm{pv}}R^{\mathrm{g}}_{\mathrm{eq}}}{I_{\mathrm{pv}}L}. \tag{3.2}$$

By neglecting the parasitic elements, (3.2), simplifies to

$$\omega^{\mathrm{g}}_{\text{RHP-zero1}} \approx \frac{\frac{V_{\mathrm{pv}}}{I_{\mathrm{pv}}}}{L} = \frac{R_{\mathrm{pv}}}{L}. \tag{3.3}$$

When considering the shape of the IV curve of the PVG in general, it can be concluded that the static resistance R_{pv} is lower in the CC region than in the CV region and is dependent on the operating point. According to (3.3), the same applies to the RHP zero. In the CV region, the frequency of the zero is lowest when the operating point is close to the MPP and highest when it is close to the OC condition. In the analysis above the source was assumed to be ideal. In reality, the PVG is a highly nonlinear source and it has been shown to have major effect on the dynamics of the interfacing converter. For

this reason, also the source-affected control-to-output transfer function was determined symbolically. The impedance of the PVG is approximated using the dynamic resistance r_{pv} in the following equations for simplicity. For a more exact model, the measured output impedance of the PVG can be included directly in the model. However, the dynamic resistance offers adequate approximation for the following analysis.

The ideal (infinite bandwidth) input admittance $Y_{\text{in-}\infty}$ was first calculated by substituting (B.2),(B.5),(B.4), and (B.7) into (B.23) resulting

$$Y^{\mathrm{g}}_{\text{in-}\infty} = Y^{\mathrm{g}}_{\mathrm{in}} - \frac{G^{\mathrm{g}}_{\mathrm{io}} G^{\mathrm{g}}_{\mathrm{ci}}}{G^{\mathrm{g}}_{\mathrm{co}}} = \frac{LC_1\left(s^2 - s\left(\frac{D'V^{\mathrm{g}}_{\mathrm{eq}}}{LI_{\mathrm{pv}}} - \frac{R^{\mathrm{g}}_{\mathrm{eq}}+r_{\mathrm{C1}}}{L}\right) + \frac{1}{LC_1}\right)}{\left(sL - \frac{D'V^{\mathrm{g}}_{\mathrm{eq}}}{I_{\mathrm{pv}}} + R^{\mathrm{g}}_{\mathrm{eq}}\right)(1 + sr_{\mathrm{C1}}C_1)}. \tag{3.4}$$

Next, (3.4) was substituted together with (B.2) and (B.7) into (B.21). The resulting source-affected control-to-output transfer function can be presented by dividing it into the following equations

$$G^{\mathrm{g}}_{\text{co-oS}} = -\frac{I_{\mathrm{pv}}}{C_2}\frac{\left(s^2 - sA^1 - A^0\right)(1 + sr_{\mathrm{C2}}C_2)}{s^3 + s^2B^2 + sB^1 + B^0} \tag{3.5}$$

$$A^1 = \frac{D'V^{\mathrm{g}}_{\mathrm{eq}}}{I_{\mathrm{pv}}L} - \frac{r_{\mathrm{C1}}r_{\mathrm{pv}} + R^{\mathrm{g}}_{\mathrm{eq}}(r_{\mathrm{C1}} + r_{\mathrm{pv}})}{L(r_{\mathrm{C1}} + r_{\mathrm{pv}})} - \frac{1}{C_1(r_{\mathrm{C1}} + r_{\mathrm{pv}})} \tag{3.6}$$

$$A^0 = \frac{D'V^{\mathrm{g}}_{\mathrm{eq}} - I_{\mathrm{pv}}\left(R^{\mathrm{g}}_{\mathrm{eq}} + r_{\mathrm{pv}}\right)}{I_{\mathrm{pv}}LC_1(r_{\mathrm{C1}} + r_{\mathrm{pv}})} \tag{3.7}$$

$$B^2 = \frac{C_1\left(R^{\mathrm{g}}_{\mathrm{eq}}(r_{\mathrm{C1}} + r_{\mathrm{pv}}) + r_{\mathrm{C1}}r_{\mathrm{pv}}\right) + L}{LC_1(r_{\mathrm{C1}} + r_{\mathrm{pv}})} \tag{3.8}$$

$$B^1 = \frac{C_2\left(R^{\mathrm{g}}_{\mathrm{eq}} + r_{\mathrm{pv}}\right) + C_1D'^2(r_{\mathrm{C1}} + r_{\mathrm{pv}})}{LC_1C_2(r_{\mathrm{C1}} + r_{\mathrm{pv}})} \tag{3.9}$$

$$B^0 = \frac{D'^2}{LC_1C_2(r_{\mathrm{C1}} + r_{\mathrm{pv}})}. \tag{3.10}$$

By neglecting the parasitic elements, $G^{\mathrm{g}}_{\text{co-oS}}$ simplifies to

$$G^{\mathrm{g}}_{\text{co-oS}} \approx -\frac{I_{\mathrm{pv}}}{C_2}\frac{s^2 - s\left(\frac{R_{\mathrm{pv}}}{L} - \frac{1}{r_{\mathrm{pv}}C_1}\right) + \frac{1-\frac{R_{\mathrm{pv}}}{r_{\mathrm{pv}}}}{LC_1}}{s_3 + s_2\frac{1}{r_{\mathrm{pv}}C_1} + s\frac{C_2+D'^2C_1}{LC_1C_2} + \frac{D'^2}{LC_1C_2r_{\mathrm{pv}}}}. \tag{3.11}$$

The roots of the numerator of (3.11) can be presented in general form as

$$G_{\text{num-gen}} = (s-a)(s-b) = s^2 - s(a+b) + ab \tag{3.12}$$

When assuming that the roots are well separated, i.e. $a >> b$, (3.12) simplifies to

$$G_{\text{num-gen}} \approx s^2 - sa + ab. \tag{3.13}$$

Now, by comparing (3.13) and the numerator of (3.11) it can be concluded that there are two RHP zeros in (3.11), approximately at

$$\omega_{\text{RHP-zero1}}^{\text{gS}} \approx \frac{R_{\text{pv}}}{L} - \frac{1}{r_{\text{pv}} C_1} \tag{3.14}$$

and

$$\omega_{\text{RHP-zero2}}^{\text{gS}} \approx \frac{1 - \frac{R_{\text{pv}}}{r_{\text{pv}}}}{C_1 R_{\text{pv}} - \frac{L}{r_{\text{pv}}}}. \tag{3.15}$$

As it is shown, the difference between $\omega_{\text{RHP-zero1}}^{\text{g}}$ and $\omega_{\text{RHP-zero1}}^{\text{gS}}$ is the latter term of $\omega_{\text{RHP-zero1}}^{\text{gS}}$. The effect of this latter term increases, when the operating point moves closer to the OC condition, because r_{pv} is increasing. However, its effect is quite small and $\omega_{\text{RHP-zero1}}^{\text{g}}$ offers good approximation as will be demonstrated later.

As in the CC region, $r_{\text{pv}} > R_{\text{pv}}$, according to the numerator of (3.15), the second zero is on the RHP. When the operating point moves towards the MPP, this zero moves towards the origin. Because at the MPP $r_{\text{pv}} = R_{\text{pv}}$, $\omega_{\text{RHP-zero2}}^{\text{gS}}$ is at the origin. In the CV region, $r_{\text{pv}} < R_{\text{pv}}$, which means that the second zero is on the LHP. As a conclusion, there are two RHP zeros in the CC region, but only one RHP zero in the CV region. The output impedance of the PVG must be included into the g-parameter set to be able to predict both of these zeros.

The low-frequency behavior of the control-to-output transfer function can be approximated by setting $s = 0$ in (3.11) yielding

$$G_{\text{co-oS-lf}}^{\text{g}} \approx -I_{\text{pv}} \frac{r_{\text{pv}} - R_{\text{pv}}}{D'^2}. \tag{3.16}$$

As in the CV region $r_{\text{pv}} < R_{\text{pv}}$, the sign of $G_{\text{co-oS-lf}}^{\text{g}}$ is positive indicating that the low-

frequency phase starts at zero. As an opposite, in CC region the sign of $G^{\mathrm{g}}_{\text{co-oS-lf}}$ is negative indicating that the low-frequency phase will change by 180°. Thus, the same controller cannot be used in both of these operating regions. If the aim is to design a controller, which is stable in the CC region, the dc gain of the controller must be negative. If the controller is designed to be stable in the CV region, the dc gain of the controller must be positive.

3.1.2 Z-parameter model

The z-parameter model of voltage-boosting dc-dc converter is presented in Appendix C similarly as the g-parameter model in Appendix B. According to (B.7), the numerator of the control-to-output transfer function is

$$G^{\mathrm{z}}_{\text{co-o-num}} = -\frac{I_{\mathrm{pv}}}{C_2}\left(s^2 - s\frac{D'V^{\mathrm{z}}_{\mathrm{eq}} - R^{\mathrm{z}}_{\mathrm{eq}}I_{\mathrm{pv}}}{I_{\mathrm{pv}}L} + \frac{1}{LC_1}\right)(1 + sr_{\mathrm{C2}}C_2)\,. \tag{3.17}$$

By making similar assumption of well separated roots and using (3.13) as in the previous section, it can be concluded that $G^{\mathrm{z}}_{\text{co-o}}$ includes two RHP zeros at

$$\omega^{\mathrm{z}}_{\text{RHP-zero1}} \approx \frac{D'V^{\mathrm{z}}_{\mathrm{eq}} - R^{\mathrm{z}}_{\mathrm{eq}}I_{\mathrm{pv}}}{I_{\mathrm{pv}}L} \tag{3.18}$$

and

$$\omega^{\mathrm{z}}_{\text{RHP-zero2}} \approx \frac{I_{\mathrm{pv}}}{C_1\left(D'V^{\mathrm{z}}_{\mathrm{eq}} - R^{\mathrm{z}}_{\mathrm{eq}}I_{\mathrm{pv}}\right)}. \tag{3.19}$$

By neglecting the parasitic elements, (3.18) and (3.19) are simplifed to

$$\omega^{\mathrm{z}}_{\text{RHP-zero1}} \approx \frac{R_{\mathrm{pv}}}{L} \tag{3.20}$$

and

$$\omega^{\mathrm{z}}_{\text{RHP-zero2}} \approx \frac{1}{R_{\mathrm{pv}}C_1}. \tag{3.21}$$

By neglecting the parasitic elements, $\omega^{\mathrm{z}}_{\text{RHP-zero1}}$ is exactly the same as $\omega^{\mathrm{g}}_{\text{RHP-zero1}}$, which was predicted by the g-parameter model. The second RHP zero existing only in

the CC region was not predicted by the g-parameter model without the effect of the source impedance. However, the z-parameter model is able to produce approximation also of this second RHP zero even if the source impedance is not taken into account.

The ideal input impedance $Z_{\text{in-}\infty}$ can be calculated by substituting (C.2),(C.5),(C.4), and (C.7) into (C.26) resulting

$$Z^{\text{z}}_{\text{in-}\infty} = Z^{\text{g}}_{\text{in}} - \frac{G^{\text{z}}_{\text{io}} G^{\text{z}}_{\text{ci}}}{G^{\text{z}}_{\text{co}}} = \frac{\left(sL - \frac{D' V^{\text{z}}_{\text{eq}}}{I_{\text{pv}}} + R^{\text{z}}_{\text{eq}} - r_{\text{C1}}\right)(1 + s r_{\text{C1}} C_1)}{L C_1 \left(s^2 - s\left(\frac{D' V^{\text{z}}_{\text{eq}}}{L I_{\text{pv}}} - \frac{R^{\text{z}}_{\text{eq}}}{L}\right) + \frac{1}{L C_1}\right)}. \tag{3.22}$$

The source-affected control-to-output transfer function can now be calculated by substituting (3.22) together with (C.2) and (C.7) into (C.24) resulting following group of equations

$$G^{\text{z}}_{\text{co-oS}} = -\frac{I_{\text{pv}}}{C_2} \frac{\left(s^2 - sA^1 - A^0\right)(1 + s r_{\text{C2}} C_2)}{s^3 + s^2 B^2 + sB^1 + B^0} \tag{3.23}$$

$$A^1 = \frac{D' V^{\text{z}}_{\text{eq}}}{I_{\text{pv}} L} - \frac{R^{\text{z}}_{\text{eq}}(r_{\text{C1}} + r_{\text{pv}}) - r^2_{\text{C1}}}{L(r_{\text{C1}} + r_{\text{pv}})} - \frac{1}{C_1(r_{\text{C1}} + r_{\text{pv}})} \tag{3.24}$$

$$A^0 = \frac{D' V^{\text{z}}_{\text{eq}} - I_{\text{pv}}\left(R^{\text{z}}_{\text{eq}} + r_{\text{pv}} - r_{\text{C1}}\right)}{I_{\text{pv}} L C_1 (r_{\text{C1}} + r_{\text{pv}})} \tag{3.25}$$

$$B^2 = \frac{C_1\left(R^{\text{z}}_{\text{eq}}(r_{\text{C1}} + r_{\text{pv}}) - r^2_{\text{C1}}\right) + L}{L C_1 (r_{\text{C1}} + r_{\text{pv}})} \tag{3.26}$$

$$B^1 = \frac{C_2\left(R^{\text{z}}_{\text{eq}} + r_{\text{pv}} - r_{\text{C1}}\right) + C_1 D'^2 (r_{\text{C1}} + r_{\text{pv}})}{L C_1 C_2 (r_{\text{C1}} + r_{\text{pv}})} \tag{3.27}$$

$$B^0 = \frac{D'^2}{L C_1 C_2 (r_{\text{C1}} + r_{\text{pv}})}. \tag{3.28}$$

Similarly as $G^{\text{g}}_{\text{co-oS}}$, also $G^{\text{z}}_{\text{co-oS}}$ can be simplified by neglecting the parasitic elements as

$$G^{\text{z}}_{\text{co-oS}} \approx -\frac{I_{\text{pv}}}{C_2} \frac{s^2 - s\left(\frac{R_{\text{pv}}}{L} - \frac{1}{r_{\text{pv}} C_1}\right) + \frac{1 - \frac{R_{\text{pv}}}{r_{\text{pv}}}}{L C_1}}{s_3 + s_2 \frac{1}{r_{\text{pv}} C_1} + s \frac{C_2 + D'^2 C_1}{L C_1 C_2} + \frac{D'^2}{L C_1 C_2 r_{\text{pv}}}}. \tag{3.29}$$

By comparing (3.5)-(3.10) and (3.23)-(3.28) it can be noted, that there are small differences. These differences can be explained by the fact that r_{C1} is included in R^{z}_{eq} but not in R^{g}_{eq}. If this detail is taken into account, it can be noted that g- and z-parameter models produce exactly the same source-affected control-to-output transfer function. As also approximated transfer functions (3.11) and (3.29) are equal, the zeros in (3.14) and

(3.15) can be predicted either by g- or z-parameter models.

3.1.3 Small-signal stability of the interface between the PVG and the converter

The closed-loop transfer functions of g- and h-parameter models are shown in Appendix B and C, when the dc-link-voltage control loop is closed. According to (B.25) and (C.28), the closed-loop input admittance and impedance can be calculated as

$$Y^{\mathrm{g}}_{\text{in-c}} = \frac{Y^{\mathrm{g}}_{\text{in-o}}}{1 + L^{\mathrm{g}}_{\text{out}}} + \frac{L^{\mathrm{g}}_{\text{out}}}{1 + L^{\mathrm{g}}_{\text{out}}} Y^{\mathrm{g}}_{\text{in-}\infty} \tag{3.30}$$

$$Z^{\mathrm{z}}_{\text{in-c}} = \frac{Z^{\mathrm{z}}_{\text{in-o}}}{1 + L^{\mathrm{z}}_{\text{out}}} + \frac{L^{\mathrm{z}}_{\text{out}}}{1 + L^{\mathrm{z}}_{\text{out}}} Z^{\mathrm{z}}_{\text{in-}\infty}. \tag{3.31}$$

At the frequencies below the crossover frequency of the controller, it can be assumed that the loop gain $L_{\text{out}} >> 1$. In this case, according to (3.31), the closed-loop input impedance of the converter can be approximated by the ideal input impedance $Z^{\mathrm{z}}_{\text{in-}\infty}$ or by the inverse of the ideal input admittance $Y^{\mathrm{g}}_{\text{in-}\infty}$. The low-frequency value of the ideal input impedance can be approximated by setting $s = 0$ in (3.22) yielding

$$Z^{\mathrm{z}}_{\text{in-c-lf}} = -\frac{DV^{\mathrm{z}}_{\text{eq}}}{I_{\text{pv}}} + R^{\mathrm{z}}_{\text{eq}} - r_{\text{C2}}. \tag{3.32}$$

By neglecting parasitic elements, (3.32) simplifies to

$$Z^{\mathrm{z}}_{\text{in-c-lf}} \approx -R_{\text{pv}}. \tag{3.33}$$

When the controller is designed to have stable operation in the CV region, the conventional minor loop gain ($Z_{\text{pv}}/Z_{\text{in-c}}$) must be used in the stability analysis (Middlebrook, 1978). When using the low-frequency approximation without parasitic elements, the minor loop gain is $-r_{\text{pv}}/R_{\text{pv}}$. As in the CV region $r_{\text{pv}} < R_{\text{pv}}$, the absolute value of the minor loop gain is always less than unity. According to the Nyquist stability criterion, the system is stable in this case. At the MPP, $r_{\text{pv}} = R_{\text{pv}}$ yielding a minor loop gain of -1, which means that the system is unstable. In addition, the system is unstable in the CC region, where $r_{\text{pv}} > R_{\text{pv}}$. In the CV region the duty cycle must be increased to increase the dc-link voltage. When the operating point moves into the CC region, the duty ratio should be decreased to increase the dc-link voltage. As the controller is designed for stable operation in the CV region, the voltage will collapse and the control system will

not recover even if the overload condition is removed.

According to (Suntio and Leppäaho, 2010), the inverse minor loop gain ($Z_{\text{in-c}}/Z_{\text{pv}}$) shall be used in the impedance-based-stability analysis of CF converters. When using inverse minor loop gain, the system is stable only in the CC region as $r_{\text{pv}} > R_{\text{pv}}$ and becomes unstable when the operating point is moved into MPP or CV region. This would require that the controller gain is negative as it was explained in the previous chapter. In case of instability, the voltage will collapse forcing the converter back into the CC region. If the instability is caused by the permanent overload, the converter will stay unstable. However, if the overload is caused by the transitory overload, the controller will continue its normal operation right after the overload condition is removed.

Based on the previous discussion, the impedance ratio to be used in impedance-based-stability analysis is different, when the converter is designed for stable operation in the CV region or the CC region. For stable operation in the CC region the correct impedance ratio is obtained by using the z-parameter model (VF-CO), and for stable operation in the CV region the correct ratio is obtained by using the g-parameter model (CF-CO). Thus, it is recommended to use z-parameter model for the converter designed for CC operation and g-parameter model for the converter designed for CV operation, in order to avoid mistakes in impedance-based-stability analysis.

3.2 DC-link-voltage control design

The presented theoretical findings were verified by designing a prototype converter employing dc-link voltage control. The converter hardware was the same as in Chapter 2. However, the inductor, input capacitor and output capacitor were changed and different PV panel was used. The reason for changing the PV panel was that that we wanted to use a real PV panel instead of the PV emulator. The only artificial light unit that was available was for the PV panel having lower power level. By using the real PV panel, it was ensured that the dynamics of the laboratory setup was as close as possible to the real system.

The PV panel used in this study was SR30-36 manufactured by Raloss. It consist of 36 series connected PV cells, and the rated MPP power is 30 W at the STC. The artificial light unit used for lighting the PV panel was able to produce 500 W/m^2 solar irradiance, yielding approximately 15W power at the MPP. As the same PV panel and artificial light unit were used in the prior research by Leppäaho et al. the existing data of output impedance and IV curve of the panel was used for plotting Figs. 3.2-3.5.

The measured IV curve is shown in Fig. 3.2. The dynamic resistance of the PV panel was extracted from the measured output impedance in several operating points. The extracted dynamic resistance and static resistance are shown in Fig. 3.2 below the IV curve. The dots represent measured/calculated values and the solid line is the trend

line. As it is shown, the SC current and OC voltage are approximately 1 A and 19 V, respectively. As expected, the dynamic resistance is higher than the static resistance in the CC region and vice versa in the CV region.

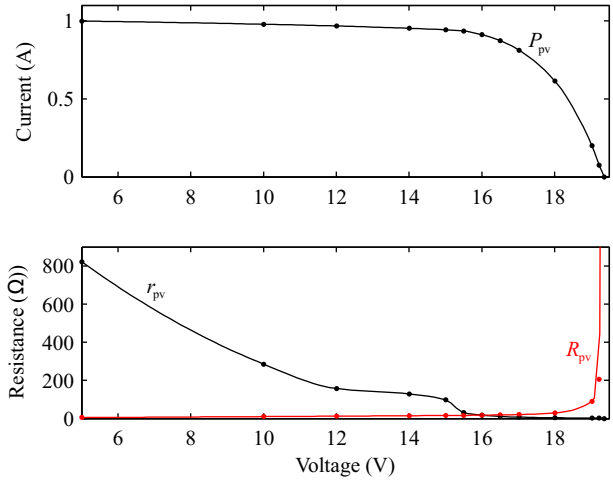

Fig. 3.2: Current, dynamic resistance and static resistance of the PV panel.

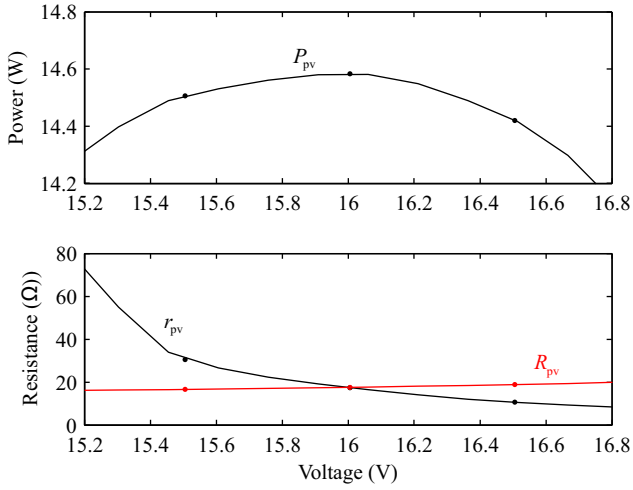

Fig. 3.3: Power, dynamic resistance and static resistance of the PV panel around the MPP.

A closer view on the behavior of dynamic and static resistances around the MPP is shown in Fig. 3.3. The output power of the PV panel is shown above as a function of voltage. As it is shown, the dynamic and static resistances are equal at the MPP as expected. When the operating point moves away from the MPP, the difference between

these resistances increases steeply. Thus the dynamics of the system changes instantly, when the operating point moves through the MPP. However, as there are tolerances, e.g., in the PWM modulator gain and measurements, it is difficult to verify the dynamic operation of the converter exactly at the MPP. The operating point is varying between the CV and CC regions around the MPP due to these tolerances. As a consequence, it is relevant to study the dynamics only in the CC and CV regions, not at the MPP.

The inductor of the converter was selected by limiting the maximum ripple to 20 % of the maximum input current (1 A) yielding 325 μH inductance. The target in selecting the capacitance values of capacitors C_1 and C_2 was to enable the design of stable controllers in the CC and CV regions using the same converter hardware. The comparison between these two controllers and operating regions is more relevant, when the converter hardware is fixed. The controllers designed for stable operation in the CC and CV regions are named here as CCR controller and CVR controller, respectively.

The lower limit for the capacitance of C_2 was found by setting the resonant frequency of the LC circuit consisting of L and C_2 to one decade lower than the lowest frequency of the first RHP zero in CV region using (3.3). The lowest frequency of this zero in the CV region is approximately at 8.6 kHz, yielding $C_2 > 107$ μF. If the capacitance of C_2 is, e.g., multiplied by ten, the shape of the control-to-output transfer function changes. The gain curve has lower gradient after the resonance, yielding lower gain margin and lower attenuation at high frequencies in case of the CVR controller. Based on these constrains, good compromise value for the capacitance of C_2 was found to be 120 μF.

The frequency of the first RHP zero is shown in Fig. 3.4 as a function of the PV voltage. The circles and asterisks denote the values calculated by using (3.14) and (3.3), respectively. The solid lines are trend lines. As shown in Fig. 3.4, the values calculated using (3.14) and (3.3) are very close to each other suggesting that the contribution of the latter term in (3.14) is very low and it can be neglected even in CV region. The red and black colors are for SC currents of 1 A and 0.5 A, respectively. When taking into account the dependency of SC current on solar irradiance, it can be said that the first RHP zero moves to the lowest frequency when the irradiance is highest. In another words, highest solar irradiance is the worst case for the CVR controller stability due to the first RHP zero.

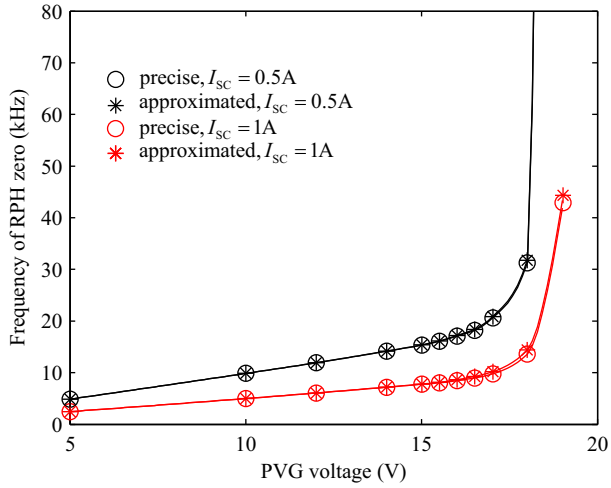

Fig. 3.4: Frequency of the first RHP zero as a function of PV voltage.

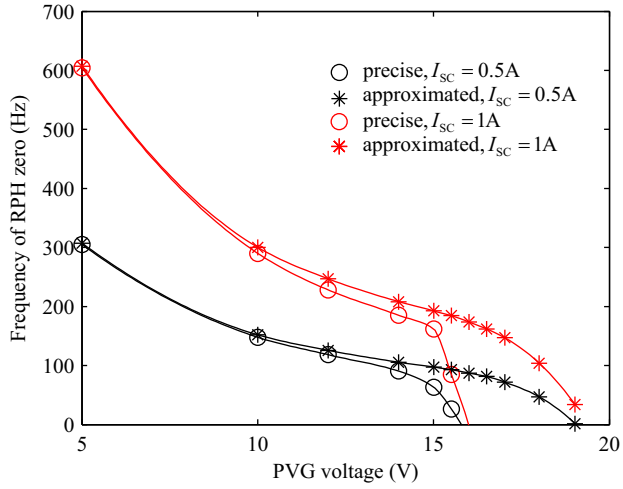

Fig. 3.5: Frequency of the second RHP zero as a function of PV voltage.

Both capacitors C_1 and C_2 affect the frequency of the resonance visible in the control-to-output transfer function but the effect of C_1 is dominant. In case of the CVR controller, capacitance of C_1 should be as large as possible to obtain low resonant frequency, yielding good phase and gain margins. Contrary to this, the capacitance of C_1 should be as small as possible in the case of the CCR controller. This is caused by the fact that according to (3.21), the frequency of the second RHP zero is inversely proportional to the capacitance of C_1. As the control bandwidth must be limited below the frequency of this zero, the smaller the capacitance, the higher the control bandwidth. As this zero is on the RHP

only in the CC region, this limitation apply only for the CCR controller. The capacitance of C_1 was set to 57 µF as it is a good compromise value between these contradictory limitations.

The frequency of the second RHP zero is shown in Fig. 3.5 as a function of the PV voltage. The circles and asterisks denote the values calculated by using (3.15) and (3.21), respectively. Solid lines are trend lines, and the red and black colors are for SC currents of 1 A and 0.5 A, respectively.

As shown in Fig. 3.5, the approximated values calculated using (3.21) match quite well with the more precise values calculated using (3.15) in the CC region. However, in the vicinity of the MPP and in the CV region, (3.21) yields incorrect values. Thus, it should be used only for approximation in the CC region but not close to MPP. The frequency of the second RHP zero goes to zero at the MPP as it was concluded in the prior analysis. The dependency on SC current is inverse compared to the first RHP zero. As the SC current is directly proportional to solar irradiance, the worst case is the lowest solar irradiance. By comparing Figs. 3.4 and 3.5, it can be noted that the second RHP zero locates at much lower frequency than the first RHP zero and thus, the effect of the second RHP zero is dominant, when designing CCR controller.

3.2.1 Stable operation in CV region

The measured (solid lines) and predicted (dots) control-to-output transfer function is shown in Fig. 3.6. The red and blue curves are measured in the CV region and the black curve is measured in the CC region. As it was predicted by studying the low-frequency behavior of the control-to-output transfer function in the prior analysis, the phase starts at zero in the CV region and at $-180°$ in the CC region. This verifies the conclusion that the controller gain must be positive in the CVR controller and negative in the CCR controller. In addition, the change in the slope of the red gain curve from -40 dB/dec to -20dB/dec approximately at 8 kHz and decrease in phase at the same frequency indicate that there is RHP zero as it was expected.

The target for the crossover frequency of the dc-link voltage control loop in the CV region was 2 kHz. As the target is above the resonant frequency shown in Fig. 3.6, the phase of the control loop must be increased by the controller in the vicinity of the resonance. Thus, PID controller having one additional pole was used as a CVR controller. Its transfer function is as

$$G_{\mathrm{c}}^{\mathrm{PID}} = \frac{K_{\mathrm{c}}\left(1+\frac{s}{\omega_{\mathrm{z1}}}\right)\left(1+\frac{s}{\omega_{\mathrm{z2}}}\right)}{s\left(1+\frac{s}{\omega_{\mathrm{p1}}}\right)\left(1+\frac{s}{\omega_{\mathrm{p2}}}\right)}, \tag{3.34}$$

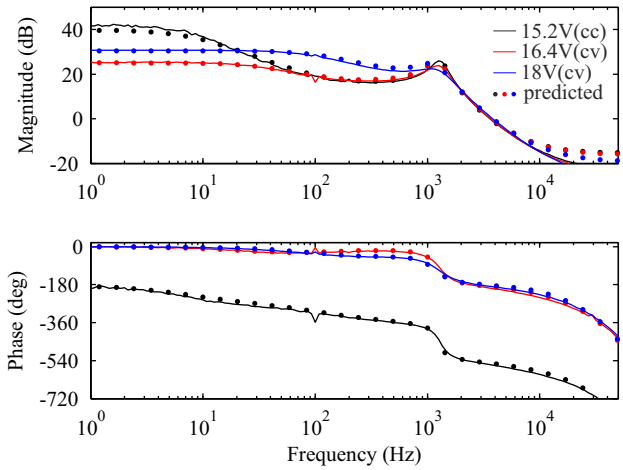

Fig. 3.6: Measured and predicted source-affected control-to-output transfer function of the VF converter.

where $\omega_{z1} = 2\pi 600$ Hz, $\omega_{z2} = 2\pi 600$ Hz, $\omega_{p1} = 2\pi 12$ kHz, $\omega_{p1} = 2\pi 50$ kHz, and $K_c = 251$. The delay caused by the sampling and processing was approximated to be 1.5 times the switching cycle and it was included in the loop gain by using a second-order Padé approximation. The measured (solid lines) and predicted (dots) control loop gain is shown in Fig. 3.7. The black curve is measured at 16.4 V close to MPP and red curve is measured at 18 V close to OC condition.

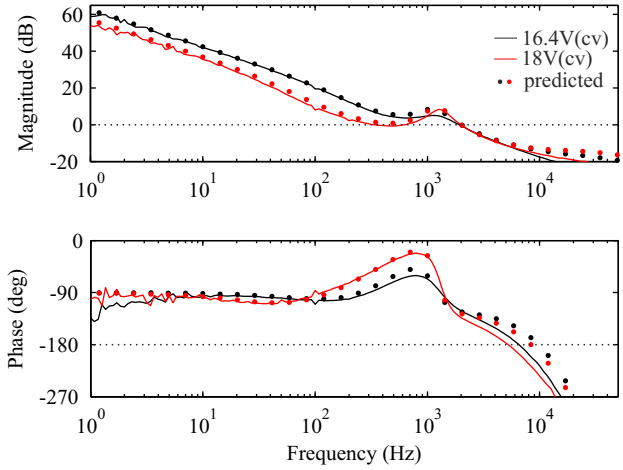

Fig. 3.7: Measured and predicted loopgain in case of CVR controller.

As shown in Fig. 3.7, the smallest gain margin is approximately 11 dB and the phase margin is 50°. According to the red curve in Fig. 3.7, the magnitude is approximately unity in the frequency range from 200 Hz to 1 kHz when the input voltage is 18V. The gain can be increased by moving the resonance to slightly lower frequency, e.g., by increasing the capacitance value of C_1. Now the resonant frequency and crossover frequency of the control loop are a bit too close to each other. The decrease of the phase after 2 kHz is caused by the delay of the controller and it implies that higher crossover frequency with sufficient phase margin is difficult to obtain.

The measured (solid lines) and predicted (dots) closed-loop output output impedances of the converter are shown in Fig. 3.8. The output impedance was measured at the same operating points as the loop gain. As the magnitude of the impedance is relatively small, it implies that the transient performance is good.

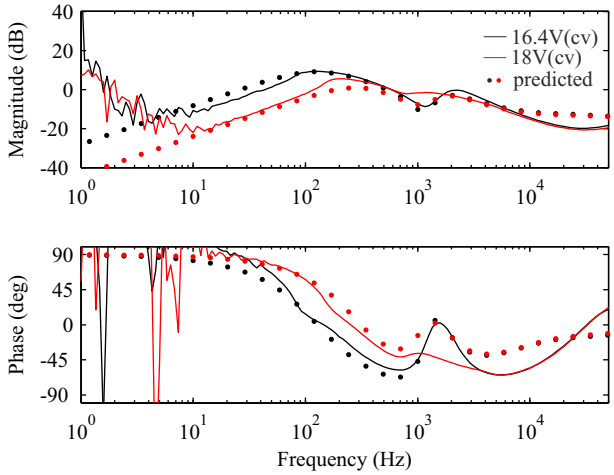

Fig. 3.8: Measured and predicted closed-loop output impedances of the converter when using CVR controller.

3.2.2 Stable operation in the CC region

The measured (solid lines) and predicted (dots) control-to-output transfer functions multiplied by -1 are shown in Fig. 3.9. The black and red curves are measured in the CC region and the blue curve is measured in the CV region. Due to the multiplication by -1, the phase starts now from zero in the CC region and from $-180°$ in the CV region. Thus, using negative gain in the controller, the control loop is stable in the CC region and unstable in the CV region. The exact locations of the RHP zeros are quite difficult to determine from Fig. 3.9. Thus, the pole-zero map was used to extract the exact locations of the poles and zeros by using the same model, which was used to calculate the values

in Fig. 3.9. The frequencies of the RHP zeros at 15.2 V were 120 Hz and 7.5 kHz. The corresponding values at 8 V were 400 Hz and 3.3 kHz. These values are consistent with Figs. 3.4 and 3.5. In addition, as the predicted and measured curves in Figs. 3.6 and 3.9 match well, the analysis and equations predicting the locations of the RHP zeros are valid.

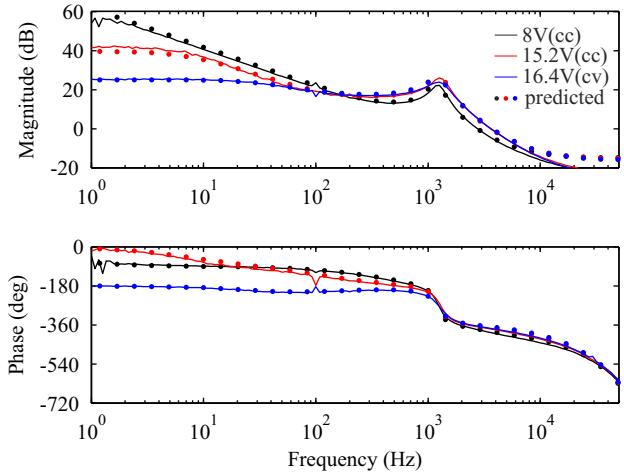

Fig. 3.9: Measured and predicted source-affected control-to-output transfer function of the converter when using negative controller gain.

According to Fig. 3.5, the frequency of the second RHP zero varies approximately from 100 Hz to 600 Hz in the CC region when the voltage is varying from 5 to 15 V and the 50% change in the solar irradiance is taken into account. Thus, the control bandwidth should be limited below 100 Hz. The basic PI controller having an additional pole was used. The purpose of the additional pole is to attenuate the high-frequency noise caused by the switching action. The transfer function of the controller is

$$G_{\mathrm{c}}^{\mathrm{PI}} = \frac{K_{\mathrm{c}}\left(1+\frac{s}{\omega_{\mathrm{z}}}\right)}{s\left(1+\frac{s}{\omega_{\mathrm{p}}}\right)}, \tag{3.35}$$

where $\omega_{\mathrm{z}} = 2\pi 10$ Hz, $\omega_{\mathrm{p}} = 2\pi 300$ Hz, and $K_{\mathrm{c}} = -2$.

The measured (solid lines) and predicted (dots) control loop gains are shown in Fig. 3.10. The black curve is measured at 8 V (current region) and red curve is measured at 15.2 V, close to MPP. As it is shown, the crossover frequency decreases, when the operating point moves towards the MPP. The lowest crossover frequency is approximately 15 Hz and the highest crossover frequency is 36 Hz. The phase margin is varying approxi-

mately from 65° to 80° and gain margin from 15 dB to 17 dB indicating stable control loop. However, as the crossover frequency is low and the phase margin relatively high, it implies that the load transient response is poor as discussed more in detail in (Kivimaki et al., 2017).

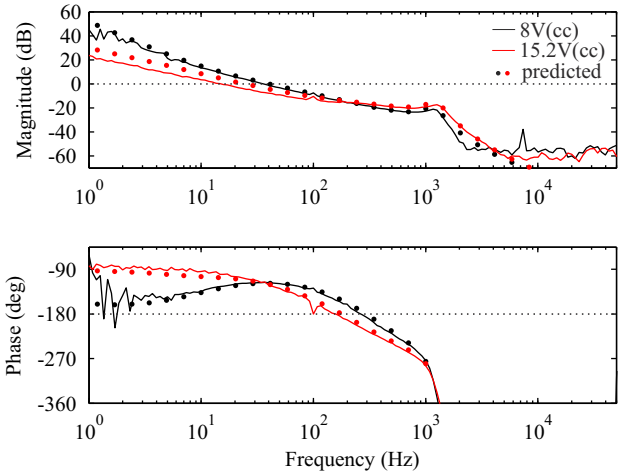

Fig. 3.10: Measured and predicted loopgain in case of CCR controller.

The measured (solid lines) and predicted (dots) closed-loop output impedances of the converter are shown in Fig. 3.11. The black curve is measured at 8 V (current region) and red curve is measured at 15.2 V close to MPP. By comparing Figs. 3.11 and 3.8, it can be noted that the output impedance is much higher when using the CCR controller compared to the CVR controller. The high output impedance implies poor transient response.

3.3 Experimental evidence

The impedance ratio (minor loop gain) can be presented in the complex frequency plane by the Nyquist diagram and it can be used for studying the stability of the interconnected system. As the PVG and the converter are stable subsystems, there are no RHP poles in the minor loop gain. Thus, according to the Nyquist stability criterion, the system is stable if the critical point (-1,0) is not encircled.

The input impedance of the converter and the output impedance of the panel was measured in several operating points in the CC and CV regions. The measured impedance ratios ($Z_{\text{pv}}/Z_{\text{in-c}}$) in the CV region are shown in Fig. 3.12. The black, red and blue curves are measured at 16.3 V, 17 V and 18 V, respectively. None of these curves encircle the critical point indicating that the system is stable. However, as the operating point moves

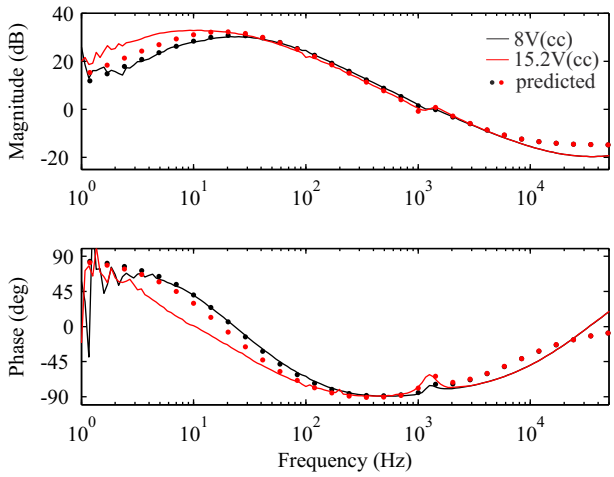

Fig. 3.11: Measured and predicted closed-loop output impedances of the converter, when using CCR controller.

closer to the MPP, the curve gets closer to the critical point. If the voltage would be further decreased, the Nyquist contour would encircle the critical point into clockwise direction meaning that the system would be unstable.

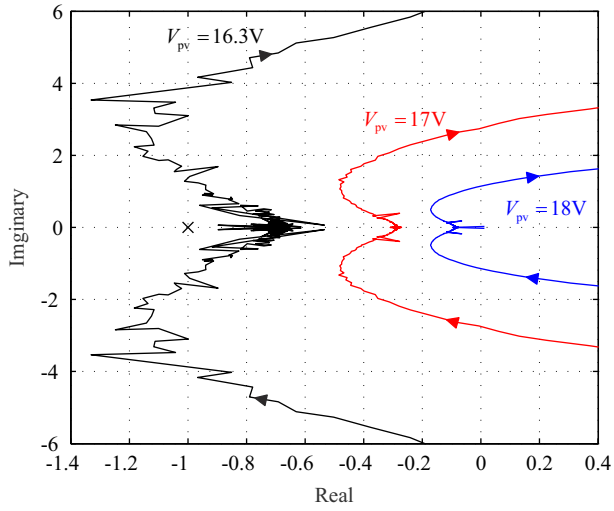

Fig. 3.12: The measured ratios of the impedances in complex plane when the operating point moves towards the MPP in CV region.

The time-domain behavior is demonstrated in Fig. 3.13, when using the CVR con-

troller and the operating point is changed from CV region to MPP. The change of the operating point is implemented by changing the the load current at time instant t_1. Fig. 3.13 shows that the MOSFET will stay permanently on due to the instability. Even if the load current goes to zero, the converter will not recover from the instability. It is also visible that the load step of 0.4 A causes only a small dip into output voltage as it was expected based on low magnitude of closed-loop output impedance, which was shown in Fig. 3.13.

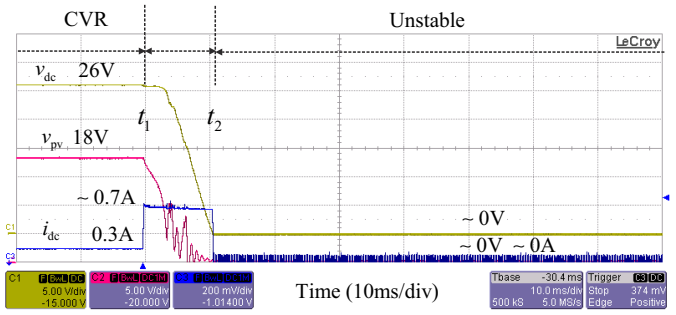

Fig. 3.13: The operation of the converter, when using CVR controller and the operation point is changed from CV region to MPP.

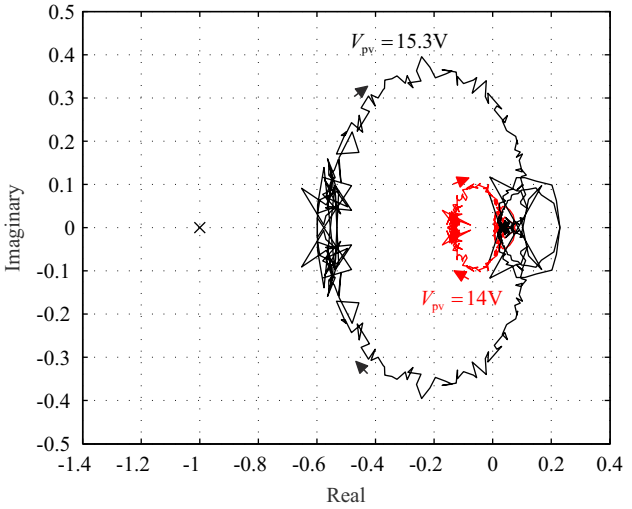

Fig. 3.14: The measured ratios of the impedances in complex plane, when the operating point moves towards the MPP in CC region.

The measured impedance ratios ($Z_{\text{in-c}}/Z_{\text{pv}}$) in the CC region are shown in Fig. 3.14. The black and red curves are measured at 15.3 V, and 14 V, respectively. As it is shown, either one of these curves encircles the critical point implying that the system is stable at the measured operating points. However, if the voltage of the PVG would be further

increased, the resulting curve would encircle the critical point into clockwise direction indicating instability.

The time-domain behavior of the CCR controller was demonstrated by changing the operating point from CC region to the MPP and back using a load step. As shown in Fig. 3.15, the load current was stepped up at time instant t_1. After the voltage of the PVG reaches the MPP at time instant t_2, the MOSFET will stay permanently off due to the instability. Between the time instants t_1 and t_2, the output voltage is determined by the PVG and load current. After the load current is changed back to the lower value at time instant t_3, the operating point moves automatically back to the CC region and the converter continues its normal operation. It is also visible that during the load step at time instant t_1, the dip in the output voltage is large as it was expected based on large closed-loop output impedance. This dip is much higher compared to the converter controlled by the CVR controller.

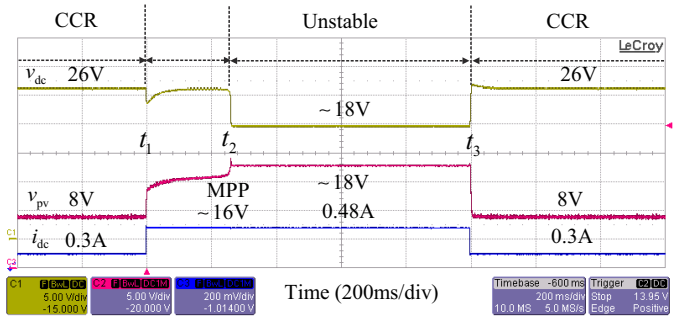

Fig. 3.15: Operation of the CF converter, when the operation point is changed from CC region to MPP and back.

3.4 Conclusions

The dynamics, control design, and component selection of the voltage-boosting dc-dc converter operating in grid-forming mode was studied. In the case of the two-stage PV inverter operating in grid-feeding mode, the dc-link voltage is controlled by the dc-dc converter. Contrary to grid-feeding operation, a single controller cannot be stable in both the CC and CV regions. Instead, the controller can have stable operation only in one of these regions. If the converter is designed to have stable operation in the CV region, it is possible to obtain high-bandwidth controller and thus, good transient performance. In order to obtain high bandwidth, the dc-link capacitor cannot have very large capacitance and the large value of input capacitor is preferable. However, also the performance demands in grid-feeding operation affect the optimum value of the input capacitor. In addition, if the operating point slips to the MPP or the CC region, the

converter will stay permanently unstable. The only way to continue stable operation is to first decrease the load and then to reset the controller.

The clearest benefit of designing the converter to have stable operation in the CC region is its ability to automatically recover after instability caused by moving the operating point into the MPP or CV region. It was shown that the converter is able to continue its normal operation right after the overload condition is over. However, the control bandwidth must be limited to very low level due to the low-frequency RHP zero in the control loop. Thus the transient performance is very poor. The performance could be somewhat improved by using small capacitance value in the input capacitor. However, the selected value should be suitable for grid-feeding operation as well. The usage of adaptive control methods is probably compulsory in practical implementations if the converter is required to operate in the CC region, when operating in grid-forming mode.

It was also shown that the control-to-output dynamics of the dc-link-voltage controlled converter can be described correctly either by the z-parameter or g-parameter model as long as the output impedance of the PVG is taken into account in the model. If the correct impedance ratio for impedance-based stability analysis is not known, it can be found explicitly by selecting the z-parameter or g-parameter model, when designing the controller for operation in the CC or CV region, respectively.

4 SATURATING GRID-FILTER INDUCTORS IN THREE-PHASE PV INVERTER

In this chapter, a simulation model of the single-stage grid-connected three-phase PV inverter having saturating L-filter inductors is developed. The developed model is used for studying the effect of saturating filter inductors on the low-frequency and switching-frequency current harmonics flowing into the grid. Also an equation for estimating the peak value of the switching-frequency current ripple is presented. Finally, all the presented results are verified by measurements using a laboratory prototype.

4.1 Modeling

The main circuit of the single-stage grid-connected three-phase PV inverter is shown in Fig. 4.1. As it was previously mentioned, it is common to use LCL-type filter as it provides the same amount of attenuation in smaller size compared to L-filter. In this thesis, it is assumed that the inverter-side inductor has varying inductance and the grid-side inductor has constant inductance. As the focus is on the inverter-side inductor, the CL-part is left out from the analysis. The L and CL-parts can be analyzed separately if the inductance of the grid-filter inductor is high enough compared to the grid-side inductance and the grid side inductor is linear. Usually this assumption is valid as the inductance of the grid-filter inductor is selected to limit the maximum current ripple for preventing excessive power losses, and the value of grid-side inductor can be much smaller to obtain adequate attenuation at the switching frequency. If necessary, the linear CL part can be added into the presented model.

The effect of grid-filter inductor saturation on the low-frequency harmonics was studied by comparing two cases: The three-phase PV inverter shown in Fig. 4.1 having linear, i.e., constant valued-inductors and the same inverter having saturating inductors. The parameters of the inverter are shown in Table 4.1. The maximum switching-frequency current ripple was selected to be 10 % of the peak current, yielding an inductance of 2.5 mH in the linear case. The inductance of the saturating inductor is varying between 1 mH and 2.4 mH during the grid period. The saturating inductor was designed to have wide inductance range in order to have clear effect on low-frequency harmonics. Only a case of three individual inductors in each phase legs was studied.

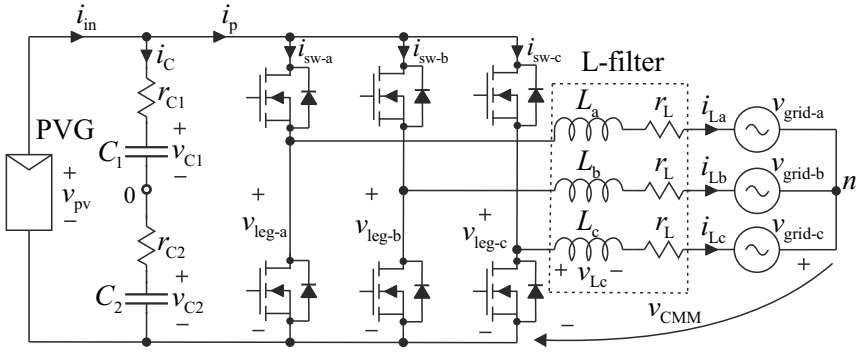

Fig. 4.1: Grid-connected three-phase PV inverter.

Table 4.1: Parameters of the studied inverter.

Symbol	Quantity	Value	Unit
P_n	Nominal power	2.7	kW
V_{in}	Input voltage	414	V
I_{in}	Input current	6.6	A
f_s	Switching frequency	20	kHz
f_g	Grid frequency	60	Hz
L	Filter inductance	2.5	mH
V_{ph}	Grid phase voltage	120	Vrms
I_{ph}	Nominal phase current	7.6	Arms
C_{in}	Total capacitance of input capacitor	1.95	mF

4.1.1 Simulation model of the three-phase inverter having saturating grid-filter inductors

The effect of hysteresis of the core material on the low-frequency harmonic currents of the inductor is negligible compared to the effect of saturation. Thus, the effect of hysteresis can be neglected. This simplifies the model significantly and offers the possibility to use behavioral model. One good alternative for this purpose was presented in (Mastromauro et al., 2008), where the model of the saturating inductor was implemented by using Volterra series expansion. The truncated series expansion was fitted to the measured flux-current data by extracting five model parameters using trial-and-error procedure. The extracting of these parameters might be time consuming.

In (Di Capua and Femia, 2016), the current of saturating inductor was reconstructed by using an algorithm, which was based on the defining equation of the inductor. In this method, also the effect of temperature on the flux-current dependency was taken into account. The developed algorithm was shown to predict the inductor current of buck

converter accurately, which was operating at switching frequency of 485 kHz . The main drawback of the presented method is its complexity.

As the complete model of the three-phase inverter is complex, it is important that the sub models of the grid-filter inductors are as simple as possible to prevent unnecessary long simulation time. For this reason, neither of the previously mentioned models were used. Instead, two different simulation models were developed, which were both based on the measured current-inductance curve of the saturating inductor. In the first of these two models the inductance-current data is included directly in the model, and in the second model the flux-current data is calculated by integrating the current-inductance data. The flux-current data is then included in the model as a table. Thus, extraction of model parameters is not required in either of these models offering clear benefit. The current-inductance curve is usually available as it is commonly measured to verify the inductor design. Depending on the data provided by the manufacturer of the inductor core, the dependency of the flux or inductance on current can also be calculated.

Usually the simulator-based model of the saturating inductor is implemented using a controllable current source (Liu et al., 2012; Mastromauro et al., 2008; Ngo, 2002). In the case of the three-phase inverter without a neutral conductor, the model will contain three controllable current sources connected to the same circuit node. As this causes problems for the solver of the simulator, usually a resistor is connected from the star point to the center of the dc-link capacitors. Another option is to connect a resistor parallel to some of the current sources, or a resistor parallel to each current sources. Depending on the parameter values of the model, these additional resistors might affect too much the simulation, causing incorrect simulation results. An example of such model can be found from (Viinamaki, Jokipii and Suntio, 2015).

To avoid the problems caused by these additional resistors, the first of the two developed simulation models was implemented by solving the differential equations of the inverter. As the impedances of the inductors are time-varying, the filter acts as an asymmetric load for the switching bridge and therefore, solving the common-mode voltage is challenging. For this reason, the model was transformed into alpha-beta frame. The common-mode voltages cancel out, when this transformation is made. It should be noted that this model can be used only for studying balanced three-phase system. The model together with simulation results and measurements was presented in (Viinamaki, Jokipii and Suntio, 2015). However, at the time the paper was written, it was not realized that the measured inductance-current data is actually differential inductance. Thus, the measurement data can be directly included into the model and it is not necessary to calculate effective inductance as it was claimed. As the effective inductance was calculated by using the measured data, the predicted switching-frequency ripple was higher than in reality. Despite this error, the main conclusions made in the paper are correct and

consistent with the analysis presented in this thesis.

The second simulation model was implemented by using three controllable current sources and by connecting a resistor from the star point to the center of the dc-link capacitors. As the equations used to implement the first simulation model were already shown in (Viinamaki, Jokipii and Suntio, 2015), they are not repeated here. Instead, the second of the developed simulation models is presented in the following.

Both of the developed simulation models were implemented in MATLAB® Simulink. This simulation software was selected, because the control system can be easily included in the model. Also a PV generator model based on (Villalva et al., 2009) and verified for Naps NAPS NP190GKg PV panel in (Maki and Valkealahti, 2012), was included in the simulation model. If the presented simulation model is used to study the operation of the inverter only at a certain operating point, the PV generator model can be replaced by a constant-valued current source. However, when the PV generator model is included, the simulator operates closer to the real system, where the current of the PV generator is dependent on voltage.

The inductance of the saturating inductor in phase a was measured as a function of current and a polynomial curve was fitted to the measured values as shown in Fig. 4.2. The inductance was measured for different DC bias current levels with the step of 1 A. The inductance was extracted by first measuring the impedance of the inductor by a frequency response analyzer and then fitting the measured impedance to the mathematical representation of a RL-circuit.

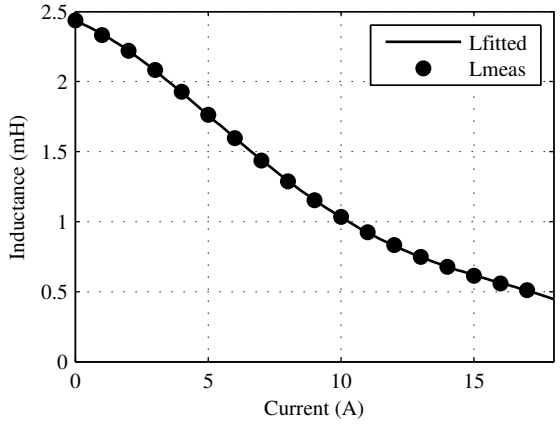

Fig. 4.2: Measured inductance and fitted polynomial.

The aforementioned measurement assumes that the inductance is linear around each measurement point. This kind of inductance is also called differential inductance L_{d}, which is the derivative of the flux linkage Ψ with respect to current. On the other hand,

the flux linkage can be solved as

$$L_{\mathrm{d}} = \frac{\mathrm{d}\Psi(i)}{\mathrm{d}i} \Leftrightarrow \Psi(i) = \int L_{\mathrm{d}}\,\mathrm{d}i + \Psi_0. \tag{4.1}$$

The fitted polynomial in Fig. 4.2, was integrated with respect to current yielding the flux linkage shown in Fig. 4.3. The negative values of the flux linkage were mirrored from the positive values. The flux linkage-current pairs can now be substituted into a lookup table. When the y and x axes are interchanged, the table gives the current value for any given flux linkage value. The flux linkage can be solved from the basic equation of the voltage across inductor as

$$v_{\mathrm{L}} = r_{\mathrm{L}} i_{\mathrm{L}} + \frac{\mathrm{d}\Psi}{\mathrm{d}t} \Leftrightarrow \Psi = \int (v_{\mathrm{L}} - r_{\mathrm{L}} i_{\mathrm{L}})\,\mathrm{d}t, \tag{4.2}$$

where v_{L} = inductor voltage, r_{L} = effective series resistance of the inductor, i_{L} = inductor current and Ψ is the flux linkage in the inductor.

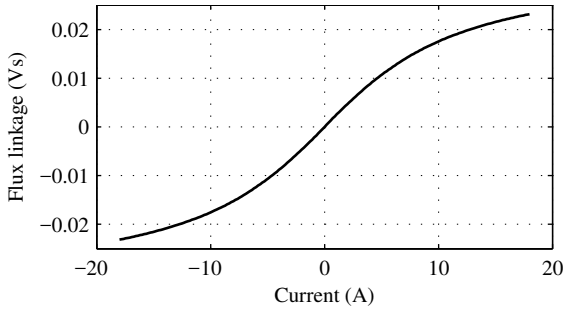

Fig. 4.3: Calculated flux linkage.

The simplified behavioral model of a saturating inductor was implemented based on (4.2) and flux linkage table in MATLAB® Simulink using SimPowerSystems component library, as shown in Fig. 4.4. This inductor model was included in the simulation model of the three-phase grid connected inverter.

In order to avoid algebraic loops caused by three individual controlled current sources connected into the same circuit node, an additional 1 kΩ resistor was connected from the star point of the three-phase voltage source into the center point of the input capacitors. As the selection of a proper resistor value might be difficult if the simulation parameters are not favorable, it is clearly one of the biggest drawbacks of the this model. The complete simulation model is shown in Appendix D.

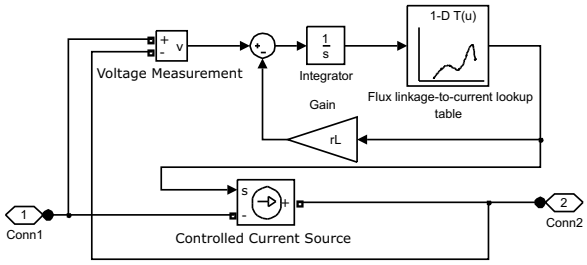

Fig. 4.4: Simulation model of single saturating inductor.

4.1.2 High-frequency current ripple of the grid-filter inductor

In two-stage three-phase inverter, the amplitude of switching-frequency current ripple through the grid-filter inductor is changing during the grid period. When linear grid-filter inductors are used, two local maximums of current ripple occur: At the peak value and zero crossing of the line-frequency component. Which of these local maximums is the global maximum, depends on the operating point and parameter values of the inverter.

When saturating grid-filter inductors are used, the inductance is minimized and as a result, the current ripple is maximized at the peak of the grid current. This happens, when the length of the zero state of the switches is highest. All inverter legs are connected either to the positive or negative rail during the zero state. In this time instant, the inverter can be presented by the equivalent circuit shown in Fig. 4.5a by assuming that the fundamental-frequency component of the inductor voltage is small compared to the grid voltage, power factor is unity, and the parasitic elements are small enough to be neglected. The equivalent circuit can be further simplified to a single-phase circuit shown in Fig. 4.5b.

(a) Three-phase equivalent circuit. **(b)** Single-phase equivalent circuit.

Fig. 4.5: Equivalent circuits of the inverter when the current in phase a is at maximum value.

The simulated signals of the modulator are shown in Fig. 4.6, when the control voltage of phase a is at maximum value and sinusoidal pulse width modulation (SPWM) having

centered pulses is used. The control signals of phase a, b, c are v_{a}, v_{b}, v_{c}, respectively and the triangular carrier signal is v_{tri}. t_{s} is the switching time period and $\hat{v}_{\mathrm{tri}}$ is the peak value of the carrier signal. According to Fig. 4.6, the maximum length of zero state is $t_{\mathrm{zc}} = \left(\frac{\hat{v}_{\mathrm{tri}}}{2\hat{v}_{\mathrm{tri}}} - \frac{\hat{v}_{\mathrm{a}}}{4\hat{v}_{\mathrm{tri}}}\right) t_{\mathrm{s}}$. On the other hand, the modulation index $m = \frac{\hat{v}_{\mathrm{a}}}{\hat{v}_{\mathrm{tri}}}$. By combining these two equations, the maximum length of zero state t_{zc} can be expressed as

$$t_{\mathrm{zc}} = \frac{1}{2}\left(1 - \frac{1}{2}m\right) t_{\mathrm{s}}. \tag{4.3}$$

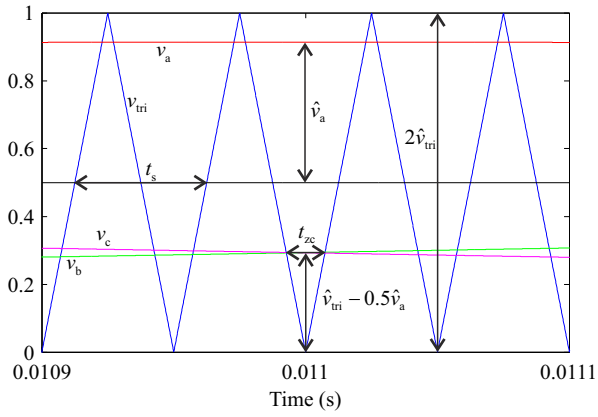

Fig. 4.6: SPWM signals at peak of the grid current when using centered PWM.

By substituting the information provided in Fig. 4.5b and (4.3) into defining equation of the inductor, the maximum peak-to-peak current ripple through the saturating inductor can be approximated as

$$\Delta i_{\mathrm{Lp\text{-}p}} = t_{\mathrm{zc}} \frac{v_{\mathrm{L0}}}{L} = \frac{1}{2}\left(1 - \frac{1}{2}m\right) t_{\mathrm{s}} \frac{3\sqrt{2}V_{\mathrm{ph}}}{2L_1 + L_2}, \tag{4.4}$$

where v_{L0} is the voltage across the inductor during zero state, V_{ph} is the rms value of the grid voltage, L_1 is the inductance when the current is at the peak value and L_2 is the inductance when the current is half of the peak value. In case of linear inductors, L_2 equals L_1.

The amplitude of the switching-frequency current ripple is also dependent on the selected PWM scheme. The simulated signals of the modulator are shown in Fig. 4.7, when trailing edge modulation is used. As shown, there are two zero states t_{zt1} and t_{zt2}.

As t_{zt1} comes right after t_{zt2}, there are two zero states next to each other. Thus, the total length of zero state is the sum of both of these two zero states.

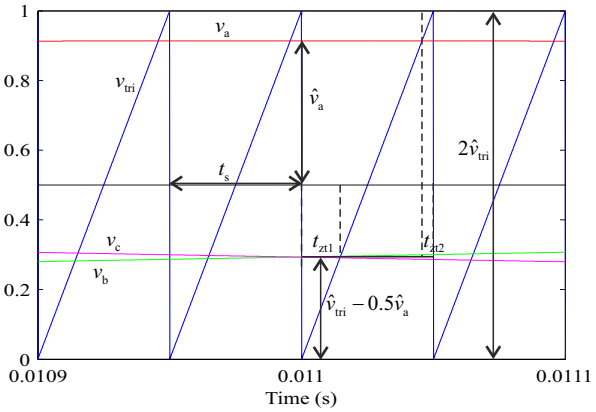

Fig. 4.7: SPWM signals at peak of the grid current when using trailing edge PWM.

According to the illustration in Fig. 4.7, the total length of the zero state t_{zt} in case of trailing edge modulation can be calculated as

$$\begin{aligned} t_{zt} &= t_{zt1} + t_{zt2} = \left(\frac{\hat{v}_{tri}}{2\hat{v}_{tri}} - \frac{\hat{v}_a}{4\hat{v}_{tri}}\right) t_s + \left(\frac{2\hat{v}_{tri}}{2\hat{v}_{tri}} - \frac{\hat{v}_{tri}}{2\hat{v}_{tri}} - \frac{\hat{v}_a}{2\hat{v}_{tri}}\right) t_s \\ &= \left(\frac{1}{2} - \frac{3}{4}m\right) t_s. \end{aligned} \tag{4.5}$$

The equation for approximating the maximum peak-to-peak current ripple in case of trailing edge modulation can be solved by substituting (4.5) together with the information in Fig. 4.5b into the defining equation of the inductor yielding

$$\Delta i_{Lp\text{-}p} = t_{zt}\frac{v_{L0}}{L} = \left(\frac{1}{2} - \frac{3}{4}m\right) t_s \frac{3\sqrt{2}V_{ph}}{2L_1 + L_2}. \tag{4.6}$$

It can be noted by comparing (4.4) and (4.6) that trailing edge PWM yields higher current ripple compared to centered pulse PWM.

The grid-current peak value in the studied inverter was 10.7 A. Thus, according to Fig. 4.2, L_1=0.95 mH and L_2=1.72 mH. Substituting these values together with the other inverter parameters in Table 4.1 into (4.4) gives the maximum peak-to-peak ripple of 2 A. For comparison, the ripple is 1 A in linear 2.5-mH inductor. On the other hand, if the linear inductance is decreased from 2.5 mH to 1.2 mH, the current ripple would be

2 A, similarly as with the saturating inductors. However, when the power is smaller, the saturating inductor would offer smaller current ripple compared to the linear inductor. For example, if the inverter is operating at half the nominal power, the current ripple is 1.3 A whereas for 1.2 mH linear inductors the ripple would be still 2 A.

According to the previous discussions, the power produced by the PV generator is directly dependent on the solar irradiance, which is varying throughout the day. For this reason, the inverter is usually selected to have smaller nominal power than the power of the PVG in STC. Despite of this, the PV inverter is operating considerable part of the day at less than nominal power. Thus, the high-frequency current ripple fed to the grid would be smaller in the case of saturating inductor of the previous example. Smaller current ripple improves the total harmonic distortion (THD) of the inverter at lower power levels compared to linear inductors.

4.1.3 Control system of the inverter

The control system of the inverter was implemented by using cascaded-control scheme in dq-frame as shown in Fig. 4.8. The basic idea in this control method, is to present the instantaneous values of phase currents using a space vector in rotating reference frame. The instantaneous values of phase currents are first presented as a space vector in stationary reference frame using Clarke's transformation. The resulting vector is rotating at grid frequency. This vector is then transformed into rotating reference frame using Park's transformation. The resulting vector appears now as it is stationary. This means that conventional control methods as PI controllers can be used. The angle of the grid voltage is required for making the Park's transformation and phase-locked loop (PLL) is used for extracting the angle from measured grid voltages. Conventional synchronous reference frame phase-locked loop (SRF-PLL) was used in this thesis.

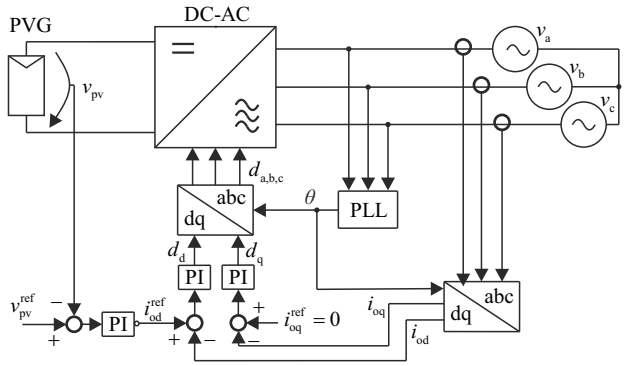

Fig. 4.8: Block diagram of the control system.

Contrary to the practical implementation of a PV inverter, MPPT is neglected and the PV generator voltage reference is set manually to the MPP of the PV generator. The control design was performed by first solving the system transfer functions from the small-signal model presented in (Puukko and Suntio, 2012) and then applying the loop shaping technique for each control loop. The inductors were assumed to be linear, when selecting the control parameters. PI-controllers having an additional high-frequency pole were used similarly as in the controller of the dc-dc converter designed in the previous chapter. The parameters of the controllers are shown in Table 4.2, where ω_z, ω_p, and K_c refer to (3.35). In addition, the predicted crossover frequencies and the phase margins are given in Table 4.2. These values were not verified by measurements, because the small-signal model used for control design was already verified in Puukko and Suntio (2012).

Table 4.2: Control system parameters.

	V_{in} control loop	i_d control loop	i_q control loop	PLL
ω_z	2π2 Hz	2π150 Hz	2π150 Hz	2π0.5 Hz
ω_p	2π500 Hz	2π10000 Hz	2π10000 Hz	2π50 Hz
K_c	-2.51	35.48	35.48	-0.12
Crossover frequency	10 Hz	1 kHz	1 kHz	1 Hz
Phase margin	75°	82°	82°	64°

4.2 Simulation results

The simulated switching-frequency current ripple is shown in Fig. 4.9 when using the model presented in Appendix D. The maximum value of the ripple is approximately 1A peak-to-peak when the filter inductors are linear and 2 A peak-to-peak when the saturating inductors are used. Thus, the simulated current ripple equals the values predicted by (4.4). As the ripple current in the saturating inductor is twice the current in the linear inductor, also the attenuation capability of the CL-part is required to be doubled compared to the linear case.

The low-frequency harmonics of the inverter were simulated by using both of the developed simulation models. The simulation result is shown in Fig. 4.10, when using the model presented in Fig. 4.9 and in Fig. 4.11, when using the model presented in (Viinamaki, Jokipii and Suntio, 2015). As it is shown, there is a small amount of 3rd harmonic component in Fig. 4.10b but not in Fig. 4.11b. The existence of these components might be caused by the additional resistor, which was used in the model implemented by controllable current sources. However, the magnitude of these components is negligible.

The simulated harmonics of phase a current are shown in Figs. 4.10a and 4.11a, when the controllers are not connected i.e. the inverter is operating in open loop. It is clearly

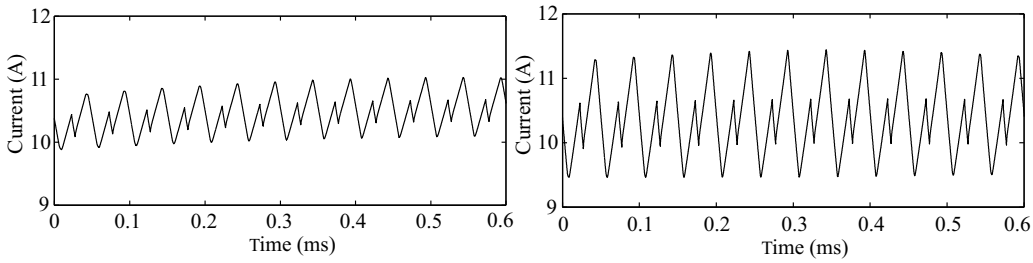

(a) Linear L-filter.

(b) Saturating L-filter.

Fig. 4.9: Simulated switching-frequency current ripple.

visible, that 5^{th} harmonic component is increased, when the saturating inductors are used. The increase in 7^{th} harmonic is quite small. However, when the controllers are connected, the difference between linear and saturating inductors is decreasing significantly as shown in Figs. 4.10b and 4.11b.

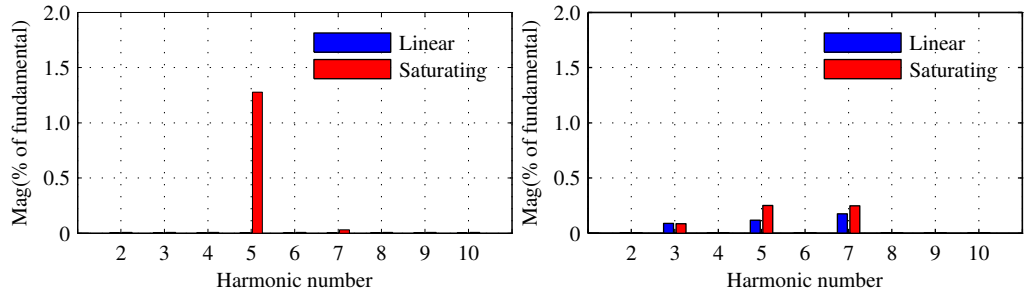

(a) Inverter is operating in open loop.

(b) Inverter is operating in closed loop.

Fig. 4.10: Simulated inductor-current harmonics in phase a in case of SimPowerSystems-based model.

4.3 Experimental evidence

The saturating inductors were implemented by winding 170 rounds of copper wire on toroidal shaped inductor core manufactured by Magnetics. The type number of the core is 0077907A7. It is made of sendust metal powder and it has no discrete air gap. When discrete air gap is not used, the magnetic flux stays better inside the core and the losses are more uniformly distributed compared to an inductor with discrete air gap. In addition, the derivative of the inductance-current curve is smaller, i.e. the inductor is soft saturating.

The ability of the saturating-inductor simulation model to predict the low-frequency current harmonics was tested by feeding sinusoidal voltage across a single saturating

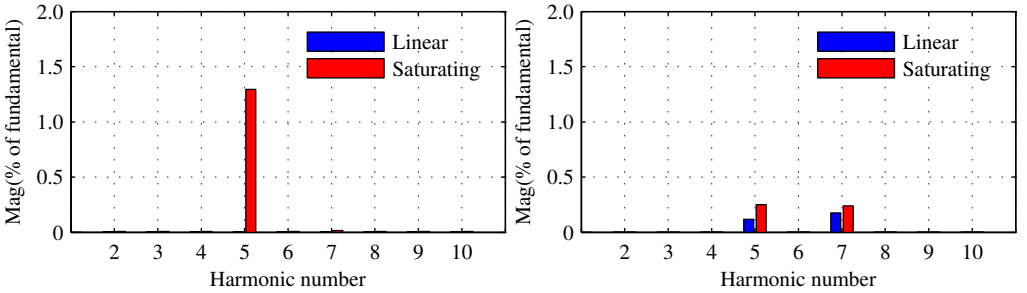

(a) Inverter is operating in open loop. **(b)** Inverter is operating in closed loop.

Fig. 4.11: Simulated inductor-current harmonics in phase a in case of model implemented in alpha-beta frame.

inductor and measuring the current harmonics. The test was repeated for the system having three inductors and a three-phase voltage source. It should be noted that a linear amplifier was used in this test, because only the inductor model was verified at this point. The measured and simulated current harmonics are shown in Fig. 4.12. As it is shown, the saturating-inductor simulation model predicts quite well the amount of low-frequency current harmonics. It is also visible that the 3$^{\text{rd}}$ harmonic component cancels out in three-phase system as expected due to the phase difference of 120° between the phase currents.

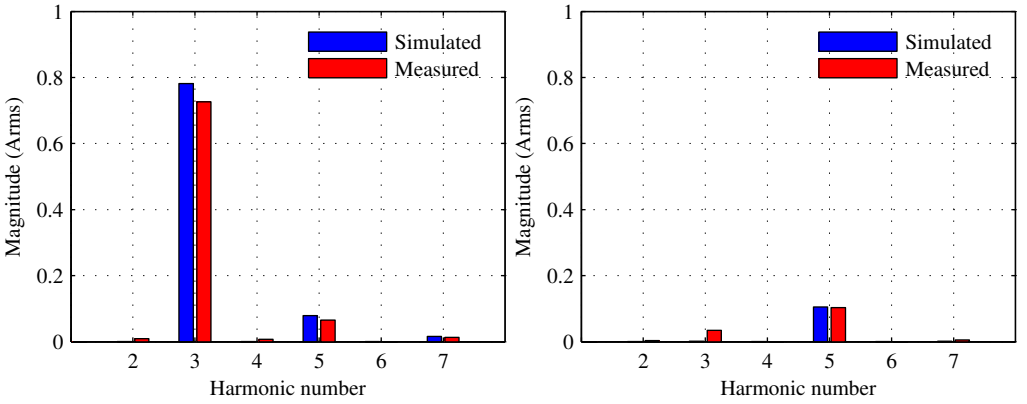

(a) Single-phase system. **(b)** Three-phase system.

Fig. 4.12: Simulated and measured current harmonics of saturating inductor.

The measured current through the single inductor and the voltage across the inductor are shown in Fig. 4.13. The effect of the 3$^{\text{rd}}$ harmonic component in the inductor current in single-phase system is clearly visible in Fig. 4.13a. The current is much more sinusoidal

in Fig. 4.13b. This offers a clear benefit for the three-phase inverter compared to the single-phase inverter, when the inductor saturation is considered. The amount of low-frequency harmonics that the control system must be able to attenuate is much smaller in the case of the three-phase inverter.

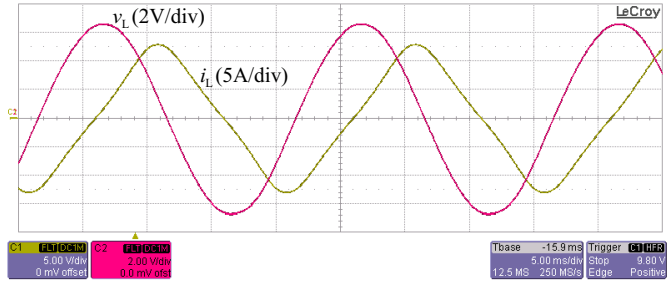

(a) Single-phase system.

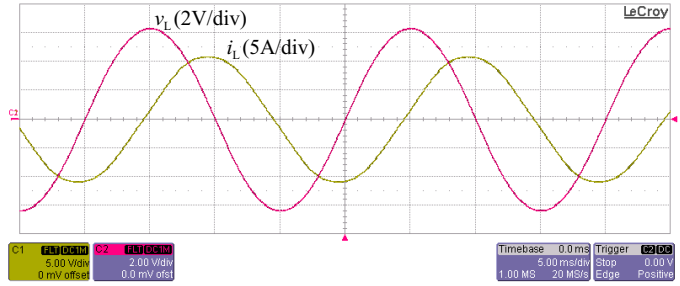

(b) Three-phase system.

Fig. 4.13: Measured current of the saturating inductor.

The simulated current harmonics in the line current of the inverter were verified by measuring the prototype inverter having parameters shown Table 4.1. The control system was implemented with a dSPACE DS 1103 controller board, which was connected to a Myway MWINV-1044-SIC-inverter. The Spitzenberger & Spies PVS 7000 solar array simulator (SAS) was used as a source and a programmable voltage source together with an isolation transformer was used to emulate the grid. The inverter was operating at the maximum power point (MPP) of the PV generator emulated by SAS with the voltage and current values of 414 V and 6.6 A. The emulated PV generator consisted of 16 pcs series connected NP190Kg solar panels having a short circuit current of 7.2 A and an open circuit voltage of 525.9 V, when the solar irradiance is 900 W/m^2. The harmonic currents were measured using a CF-5220 frequency analyzer manufactured by Ono Sokki. The measurement setup is shown in Appendix E.

The measured current harmonics in phase a are shown in Fig. 4.14. As it is shown, the 5$^{\text{th}}$ harmonic component increases as it was predicted by the simulation model,

but it decreases, when the controllers are connected and the inverter is operating with closed loop. All harmonics are slightly higher than predicted by the simulation model, even with linear inductors. However, the difference between the linear inductor and the saturating inductor is approximately the same as in the simulated results. The low-frequency harmonics produced by the saturating inductors seems not to be a problem, as the control system attenuates them effectively.

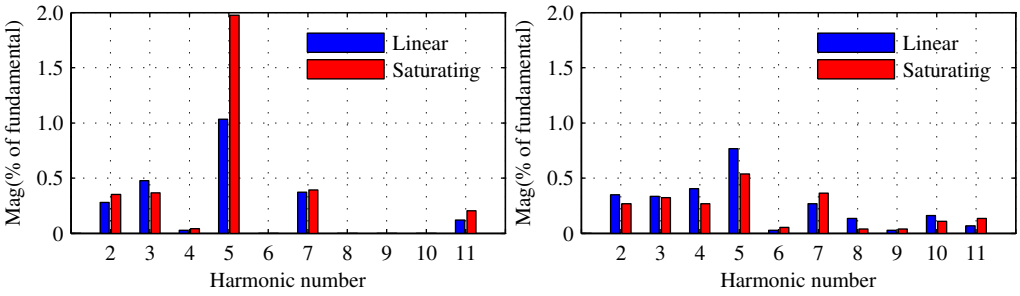

(a) Inverter is operating in open loop. **(b)** Inverter is operating in closed loop.

Fig. 4.14: Measured inductor-current harmonics in phase a.

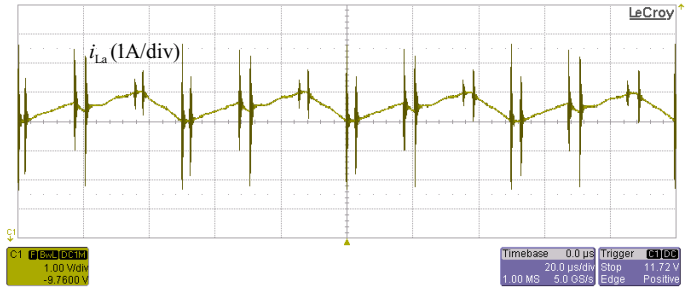

(a) Linear L-filter.

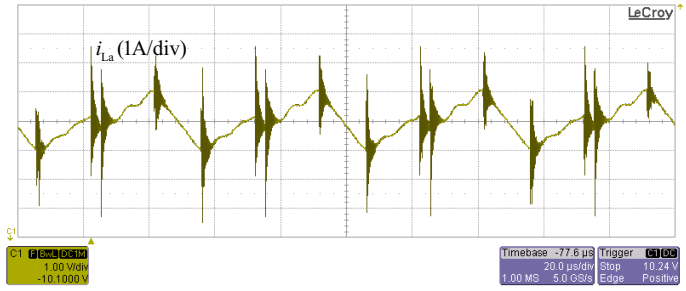

(b) Saturating L-filter.

Fig. 4.15: Measured switching-frequency current ripple in phase a.

The measured switching-frequency current ripple is shown in Fig. 4.15a, when linear inductors are used and in Fig. 4.15b, when saturating inductors are used. As it is shown, the ripple is 1 A for linear and 2 A for saturating inductors. These values are consistent with the developed analytical equation (4.4) and the simulation results. Centered PWM was used in this measurement. The test was repeated for a few different operating points to verify that the equation is valid also for different values of modulation index. Eq. (4.6) developed for approximating the switching-frequency current ripple in case of trailing edge PWM was verified in (Viinamaki, Jokipii and Suntio, 2015) by the author using small-scale prototype.

Finally, the measured current in phase a is shown in Fig. 4.16, when the control loops are connected. The switching-frequency ripple is higher, when saturating inductors are used due to lower inductance. The ripple is maximized in the peak of the grid period as it was expected.

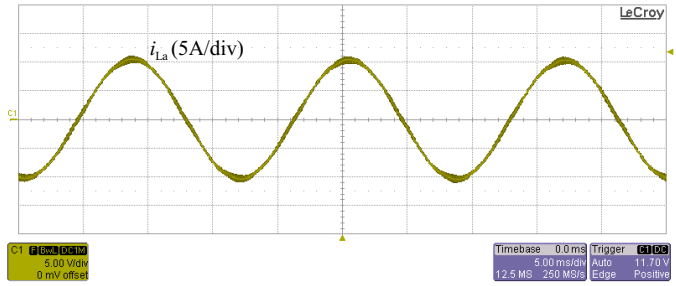

(a) Linear L-filter.

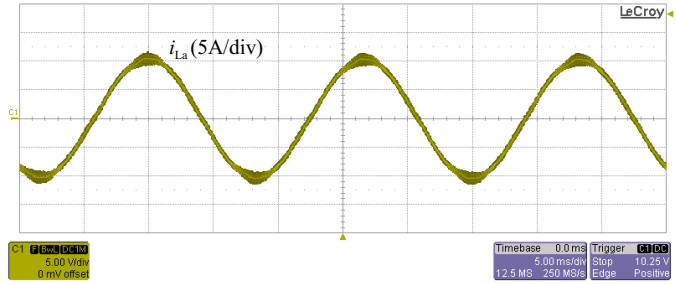

(b) Saturating L-filter.

Fig. 4.16: Measured current in phase a when the inverter is operating with closed loop.

4.4 Conclusions

The effect of inductor saturation on the harmonic currents produced by a grid-connected three-phase PV inverter was studied by simulations and measurements. The proposed model was shown to be accurate enough in predicting current harmonics caused by the saturating inductors. It was shown that the saturating L-filter inductor produces 5^{th} and 7^{th} harmonics in the line current, when the inverter is operating with open loop. These low-frequency harmonics are effectively attenuated when the control loops are closed. The conventional control method having basic PI controllers in the dq domain seems to offer adequate attenuation for these harmonics. Thus, the appearance of low-frequency harmonics is not limiting the use of saturating inductors in the studied case.

An analytical equation was proposed for evaluating the maximum magnitude of the switching-frequency current ripple in the case of saturating inductors. The proposed equation differs from the models presented in the literature in that the inductor saturation was taken into account. The accuracy of the equation was verified by using a 2.7 kW prototype and comparing the ripple of saturating and linear L-filter inductors. The inductance value of the saturating inductor was selected to be the same as in the linear inductor at low current level. In this case, the maximum current ripple is higher in the saturating inductor compared to linear inductor. When considering LCL-filter having the aforementioned L-filter as the switching bridge-side inductor, the attenuation capability of the CL-part must be higher, when saturating inductor is used.

It was also observed that as the magnitude of the switching-frequency current ripple is affected by the inductance in all three phases, the effect of saturation is not as high as might be expected by just considering a single inductor. If a linear inductor producing certain maximum amplitude of current ripple is compared with a saturating inductor offering the same current ripple, the latter option would offer smaller ripple and THD at lower power level. This would be advantageous in PV plants, where the inverter operates for significant part of the time below the maximum power rating. Thus, inductor saturation can be applied for minimizing the inductor size or the low-power current ripple.

5 CONCLUSIONS

5.1 Final conclusions

The component sizing and control design of the voltage-boosting dc-dc converter operating as a part of single-stage single-phase PV inverter was studied. The operation in grid-feeding and grid-forming modes were both investigated separately. The dc-ac inverter was left out from the analysis as the focus was on the dc-dc converter. The load of the dc-dc converter was modeled as constant voltage sink in the case of grid-feeding mode and as constant current sink in the case of grid-forming mode.

First, the design of the dc-dc converter was studied by assuming grid-feeding operation. Two interfacing converters were designed for a single 190 W PV panel to study the component sizing. In the first converter, the maximum input current of the converter was calculated by dividing the nominal power of the converter by the minimum input voltage. As this method originates from the systems having voltage-type sources, it was named as conventional design method. In the second converter, the maximum input current was assumed to equal the maximum SC current of the PV panel. Other major difference between these two designs was, that the power losses of the diode were calculated in the minimum input voltage condition in the case of conventional design, and at the MPP in the case of the modified design. According to the investigations, using the modified design method instead of the conventional one in case of wide input-voltage range yields smaller inductor core, smaller heat sink of the MOSFET, smaller input capacitor and more even temperature distribution.

By investigating the datasheets of the commercial PV inverters, it was noticed that it is common to use conventional design method in the case of narrow input voltage range, yielding reasonably small input current. In the case of high input voltage range, the maximum input current is selected to be smaller than the value resulting from the conventional design method. Thus, it seems that the manufacturers of the PV inverters are familiar with the aforementioned issues. However, the fact that conventional design method yields oversized components in the case of wide input-voltage range, needs to be mentioned also in the design manuals for interfacing converters.

A small-signal model of voltage-boosting converter having dc-link-voltage feedforward was developed. Grid-feeding operation was assumed in this study. The developed model

was used to study the effect of feedforward on the attenuation of double-line-frequency voltage ripple from the dc-link to the PVG. It was shown, that the highest attenuation is obtained by using as high dc-link voltage as possible, minimized parasitic resistances of the switches and inductor and using synchronous instead of diode-switched converter. Even if open-loop operation was assumed in this study, the presented results can be applied also for closed-loop operation. In this case, the attenuation of the double-line-frequency voltage ripple would be a sum of the effects of input voltage controller and the dc-link-voltage feedforward.

Next, the design of the dc-dc converter was studied by assuming grid-forming operation. Contrary to grid-feeding operation, a single controller cannot be stable both in CC and CV regions. Instead, the controller can have stable operation only in one of these regions. If the converter is designed to have stable operation in the CV region, it is possible to obtain high-bandwidth controller and good transient performance. In order to obtain high bandwidth, the dc-link capacitor cannot have very large capacitance, and the large value of input capacitor is preferable. However, also the performance requirements in grid-feeding operation affect the optimum value of the input capacitor. In addition, if the operating point slips to MPP or CC region, the converter will stay permanently unstable. The only way to continue stable operation is to first decrease the load and then to reset the controller.

The clearest benefit of designing the converter to have stable operation in the CC region is its ability to automatically recover after instability caused by moving the operating point into the MPP or CV region. It was shown that the converter is able to continue its normal operation right after the overload condition is over. However, the control bandwidth must be limited to very low level due to the low-frequency RHP zero in the control loop. Thus, the transient performance would be very poor.

Finally, the effect of inductor saturation on the harmonic currents produced by a grid-connected three-phase PV inverter was studied by simulations and measurements. The proposed model was shown to be accurate enough in predicting current harmonics caused by saturating inductors. It was shown that the saturating L-filter inductor produces 5^{th} and 7^{th} harmonics in the line current, when the inverter is operating with open loop. These low-frequency harmonics are effectively attenuated, when the control loops are closed. The conventional control method having basic PI controllers in the dq domain seems to offer adequate attenuation for these harmonics. Thus, the appearance of low-frequency harmonics is not limiting the use of saturating inductors.

5.2 Future research topics

The following research topics provide an interesting continuation for the research presented in this thesis.

- As it was shown, robust control design with adequate dynamics is very hard to obtain, when designing a conventional voltage-boosting dc-dc converter for stable operation in the CC region for grid-forming operation. On the other hand, if the converter is designed for stable operation in the CV region, the controller will not recover without reset when the operation point has slipped to the MPP or into the CC region. Thus, it would be interesting to study the applicability of other topologies for this application. The modified superbuck-converter reported in Agamy et al. (2013), might be a good alternative, because the low-frequency RHP zero limiting the control bandwidth in the CC region can be eliminated by selecting the input-terminal capacitors properly (Leppäaho and Suntio, 2011).

- The effect of inductor saturation on the harmonic currents produced by a grid-connected three-phase PV inverter was studied by simulations and measurements in this thesis. It was concluded that the appearance of low-frequency harmonics is not limiting the use of saturating inductors. However, the study should be extended to higher power levels to be certain that the result is applicable also in those cases. As the control bandwidth is lower in higher power level devices, the ability to attenuate the low-frequency harmonics is not that good and it might cause problems.

- The study on saturating inductors in grid-connected three-phase PV inverter was focusing only on the mitigation of low-frequency current harmonics and prediction of switching-frequency current harmonics. Also the effect of increased switching-frequency ripple on the size of the electromagnetic interference (EMI) filters should be studied. It is not yet answered if the saturating grid filter has too many negative effects on increased EMI noise (or filter size), power losses and heat for it to be used in practice.

- In this thesis, the component sizing of voltage-boosting dc-dc converter was studied separately when operating in grid-feeding and grid-forming modes. It would be interesting to continue the research by designing a two-stage PV inverter having minimized size and cost and able to operate in grid-forming, grid-feeding and grid-supporting operating modes. The results presented in this thesis could be utilized for this kind of study.

- Energy storage unit seems to be essential, when the share of intermittent renewable power generation increases. Cheap and ecological ways to store the electrical energy must be developed. Using of different technology for short-term storage and long-term storage might be economically profitable also in the future.

REFERENCES

Agamy, M. S., Chi, S., Elasser, A., Harfman-Todorovic, M., Jiang, Y., Mueller, F. and Tao, F. (2013). A high-power-density DC-DC converter for distributed PV architectures, *IEEE J. Photovolt.* **3**(2): 791–798.

Bacha, S., Picault, D., Burger, B., Etxeberria-Otadui, I. and Martins, J. a. (2015). Photovoltaics in microgrids: an overview of grid integration and energy management aspects, *IEEE Ind. Electron. Mag.* **9**(1): 33–46.

Beres, R. N., Wang, X., Blaabjerg, F., Liserre, M. and Bak, C. L. (2016). Optimal design of high-order passive-damped filters for grid-connected applications, *IEEE Trans. Power Electron.* **31**(3): 2083–2098.

Blaabjerg, F., Chen, Z. and Kjaer, S. B. (2004). Power electronics as efficient interface in dispersed power generation systems, *IEEE Trans. Power Electron.* **19**(5): 1184–1194.

Bose, B. K. (2010). Global warming: energy, environmental pollution, and the impact of power electronics, *IEEE Ind. Electron. Mag.* **4**(1): 6–17.

Bossche, A. V. and Valchev, V. C. (2005). *Inductors and transformers for power electronics*, Taylor & Francis.

Boztepe, M., Guinjoan, F., Velasco-Quesada, G., Silvestre, S., Chouder, A. and Karatepe, E. (2014). Global MPPT scheme for photovoltaic string inverters based on restricted voltage window search algorithm, *IEEE Trans. Ind. Electron.* **61**(7): 3302–3312.

Burger, B. and Rüther, R. (2006). Inverter sizing of grid-connected photovoltaic systems in the light of local solar resource distribution characteristics and temperature, *Solar Energy* **80**(1): 32–45.

Cai, H., Xiang, J. and Wei, W. (2016). Modelling, analysis and control design of a two-stage photovoltaic generation system, *IET Renewable Power Generation* **10**(8): 1195–1203.

Channegowda, P. and John, V. (2010). Filter optimization for grid interactive voltage source inverters, *IEEE Trans. Ind. Electron.* **57**(12): 4106–4114.

Chen, S., Li, P., Brady, D. and Lehman, B. (2011). Optimum inverter sizing in consideration of irradiance pattern and PV incentives, *Applied Power Electronics Conference and Exposition (APEC)*, pp. 982–988.

Chen, S., Li, P., Brady, D. and Lehman, B. (2013). Determining the optimum grid-connected photovoltaic inverter size, *Solar Energy* **87**(1): 96–116.

Cuk, S. and Middlebrook, R. D. (1977). A general unified approach to modelling switching DC-to-DC converters in discontinuous conduction mode, *Power Electronics Specialists Conference*, pp. 36–57.

Danyali, S., Hosseini, S. H., Gharehpetian, G. B. and Member, S. (2014). New extendable single-stage multi-input DC - DC/AC boost converter, *IEEE Trans. Power Electron.* **29**(2): 775–788.

Datasheet of ABB string inverter PRO-33.0 (2016).
URL: *https://library.e.abb.com/public/619bf289f98f44d2be6cbeaaf27761ad/17315_String_inverter_PRO-33.0-TL-OUTD_flyer_EN_3AUA0000164968_RevF.pdf [Date accessed: 27.12.2016]*

Datasheet of Sunny Tripower 10000TLEE-JP (2016).
URL: *http://files.sma.de/dl/22279/STP10000TLEE-JP-10-11-MOW-DEN1651-V31web.pdf [Date accessed: 27.12.2016]*

Datasheet of Vacon 8000 solar inverter series (2014).
URL: *http://www.vacon.com/ImageVaultFiles/id_3122/cf_2/Vacon-8000-Solar-Brochure-BC00414F-EN.PDF?634852861613100000/ [Date accessed: 27.12.2016]*

Di Capua, G. and Femia, N. (2016). A novel method to predict the real operation of ferrite inductors with moderate saturation in switching power supply applications, *IEEE Trans. Power Electron.* **31**(3): 2456–2464.

Donescu, V., Charette, A., Yao, Z. and Rajagopalan, V. (1999). Modeling and simulation of saturated induction motors in phase quantities, *IEEE Trans. Energy Convers.* **14**(3): 386–393.

Erickson, R. W. and Maksimovic, D. (2006). *Fundamentals of power electronics*, Springer.

Esram, T. and Chapman, P. L. (2007). Comparison of photovoltaic array maximum power point tracking techniques, *IEEE Trans. Energy Convers.* **22**(2): 439–449.

Femia, N., Petrone, G., Spagnuolo, G. and Vitelli, M. (2009). A technique for improving P&O MPPT performances of double-stage grid-connected photovoltaic systems, *IEEE Trans. Ind. Electron.* **56**(11): 4473–4482.

Forouzesh, M., Siwakoti, Y. P., Gorji, S. a., Blaabjerg, F. and Lehman, B. (2017). Step-up DC-DC Converters: a comprehensive review of voltage-boosting techniques, topologies, and applications, *IEEE Trans. Power Electron.* **32**(12): 9143–9178.

Grainger, B. M., Reed, G. F., Sparacino, A. R. and Lewis, P. T. (2014). Power electronics for grid-scale energy storage, *Proc. IEEE* **102**(6): 1000–1013.

Gu, B., Dominic, J., Zhang, J., Zhang, L., Chen, B. and Lai, J.-S. (2014). Control of electrolyte-free microinverter with improved MPPT performance and grid current quality, *Applied Power Electronics Conference and Exposition (APEC)*, pp. 1788–1792.

Ho, C. N.-M., Breuninger, H., Pettersson, S., Escobar, G. and Canales, F. (2013). A comparative performance study of an interleaved boost converter using commercial Si and SiC diodes for PV applications, *IEEE Trans. Power Electron.* **28**(1): 289–299.

Ho, C. N.-m., Breuninger, H., Pettersson, S., Escobar, G., Serpa, L. A. and Coccia, A. (2012). Practical design and implementation procedure of an interleaved boost converter using SiC diodes for PV applications, *IEEE Trans. Power Electron.* **27**(6): 2835–2845.

Hu, H., Harb, S., Kutkut, N., Batarseh, I. and Shen, Z. J. (2013). A Review of power decoupling techniques for microinverters with three different decoupling capacitor locations in PV systems, *IEEE Trans. Power Electron.* **28**(6): 2711–2726.

International Energy Agency (2016a). Key world energy statistics 2016, *Technical report*, International Energy Agency.
URL: *https://www.iea.org/publications/freepublications/publication/KeyWorld2016.pdf [Date accessed: 30.9.2016]*

International Energy Agency (2016b). Snapshot of global photovoltaic markets 2015, *Technical report*, International Energy Agency.
URL: *http://www.iea-pvps.org/ [Date accessed: 23.9.2016]*

Karshenas, H. R. and Saghafi, H. (2006). Basic criteria in designing LCL filters for grid connected converters, *International Symposium on Industrial Electronics*, pp. 1996–2000.

Kazimierczuk, M. and Starman, L. (1999). Dynamic performance of PWM DC-DC boost converter with input voltage feedforward control, *IEEE Trans. Circuits Syst. I, Fundam. Theory Appl.* **46**(12): 1473–1481.

Kivimaki, J., Kolesnik, S., Sitbon, M., Suntio, T. and Kuperman, A. (2017). Design guidelines for multi-loop perturbative maximum power point tracking algorithms, *IEEE Trans. Power Electron.* **PP**(99): 1–1.

Kjaer, S. B., Pedersen, J. K. and Blaabjerg, F. (2005). A review of single-phase grid-connected inverters for photovoltaic modules, *IEEE Trans. Ind. Appl.* **41**(5): 1292–1306.

Konstantopoulos, G. C. and Alexandridis, A. T. (2013). Non-linear voltage regulator design for DC/DC boost converters used in photovoltaic applications: analysis and experimental results, *IET Renewable Power Generation* **7**(3): 296–308.

Kouro, S., Leon, J. I., Vinnikov, D. and Franquelo, L. G. (2015). Grid-connected photovoltaic systems: an overview of recent research and emerging PV converter technology, *IEEE Ind. Electron. Mag.* **9**(1): 47–61.

Koutroulis, E. and Blaabjerg, F. (2011). Methods for the optimal design of grid-connected PV inverters, *International Journal of Renewable Energy Research* **1**(2): 54–64.

Lang, Y., Xu, D., S. R., H. and Ma, H. (2005). A novel design method of LCL type utility interface for three-phase voltage source rectifier, *Power Electronics Specialists Conference (PESC)*, pp. 313–317.

Leppäaho, J. and Suntio, T. (2011). Dynamic characteristics of current-fed superbuck converter, *IEEE Trans. Power Electron.* **26**(1): 200–209.

Liserre, M., Blaabjerg, F. and Dell'Aquila, A. (2004). Step-by-step design procedure for a grid-connected three-phase PWM voltage source converter, *Int. J. Electron.* **91**(8): 445–460.

Liserre, M., Blaabjerg, F. and Hansen, S. (2005). Design and control of an LCL -filter-based tree-phase active rectifier, *IEEE Trans. Ind. Appl.* **41**(5): 1281–1291.

Liu, Z., Abou-Alfotouh, A. and Wilkowski, M. (2012). Nonlinear inductor modeling for power converter, *Applied Power Electronics Conference and Exposition (APEC)*, Ieee, pp. 1868–1871.

Luoma, J., Kleissl, J. and Murray, K. (2012). Optimal inverter sizing considering cloud enhancement, *Solar Energy* **86**(1): 421–429.

Maki, A. and Valkealahti, S. (2012). Power losses in long string and parallel-connected short strings of series-connected silicon-based photovoltaic modules due to partial shading conditions, *IEEE Trans. Energy Convers.* **27**(1): 173–183.

Mastromauro, R. A. (2014). Voltage control of a grid-forming converter for an AC microgrid : a real case study, *Renewable Power Generation Conference (RPG)*, pp. 1–6.

Mastromauro, R. A., Liserre, M. and Dell'Aquila, A. (2008). Study of the effects of inductor nonlinear behavior on the performance of current controllers for single-phase PV grid converters, *IEEE Trans. Ind. Electron.* **55**(5): 2043–2052.

Mayer, J. N., Philipps, S., Hussein, N. S., Schlegl, T. and Senkpiel, C. (2015). Current and future cost of photovoltaics: long-term scenarios for market development, system prices and LCOE of utility-scale PV systems, *Technical report*, Fraunhofer-Institute for Solar Energy Systems.

Messo, T., Jokipii, J., Puukko, J. and Suntio, T. (2014). Determining the value of DC-link capacitance to ensure stable operation of a three-phase photovoltaic inverter, *IEEE Trans. Power Electron.* **29**(2): 665–673.

Messo, T., Jokipii, J. and Suntio, T. (2012). Steady-state and dynamic properties of boost-power-stage converter in photovoltaic applications, *International Symposium on Power Electronics for Distributed Generation Systems (PEDG)* pp. 34–40.

Middlebrook, R. (1978). Design techniques for preventing input-filter oscillations in switched-mode regulators, *National Solid-State Power Conversion Conference*, pp. 153–168.

Middlebrook, R. D. (1988). Small-signal modeling of pulse-width modulated switched-mode power converters, *Proc. IEEE* **76**(4): 343–354.

Mirzahosseini, R. and Tahami, F. (2012). A lifetime improved single phase grid connected photovoltaic inverter, *Power Electronics and Drive Systems Technology (PEDSTC)*, pp. 234–238.

Mondol, J. D., Yohanis, Y. G. and Norton, B. (2006). Optimal sizing of array and inverter for grid-connected photovoltaic systems, *Solar Energy* **80**(12): 1517–1539.

Muhlethaler, J., Schweizer, M., Blattmann, R., Kolar, J. W. and Ecklebe, A. (2013). Optimal design of LCL harmonic filters for three-phase PFC rectifiers, *IEEE Trans. Power Electron.* **28**(7): 3114–3125.

Nandi, S. (2004). A detailed model of induction machines with saturation extendable for fault analysis, *IEEE Trans. Ind. Appl.* **40**(5): 1302–1309.

Neves, F. A. S., Carrasco, M., Mancilla-David, F., Azevedo, G. M. S. and Santos, V. S. (2016). Unbalanced grid fault ride-through control for single-stage photovoltaic inverters, *IEEE Trans. Power Electron.* **31**(4): 3338–3347.

Ngo, K. (2002). Subcircuit modeling of magnetic cores with hysteresis in PSpice, *IEEE Trans. Aerosp. Electron. Syst.* **38**(4): 1425–1434.

Notton, G., Lazarov, V. and Stoyanov, L. (2010). Optimal sizing of a grid-connected PV system for various PV module technologies and inclinations, inverter efficiency characteristics and locations, *Renewable Energy* **35**(2): 541–554.

Nousiainen, L., Puukko, J., Maki, A., Messo, T., Huusari, J., Jokipii, J., Viinamaki, J., Lobera, D. T., Valkealahti, S. and Suntio, T. (2013). Photovoltaic generator as an input source for power electronic converters, *IEEE Trans. Power Electron.* **28**(6): 3028–3038.

Pan, D., Ruan, X., Bao, C., Li, W. and Wang, X. (2014). Magnetic integration of the LCL filter in grid-connected inverters, *IEEE Trans. Power Electron.* **29**(4): 1573–1578.

Perdigao, M. S., Alonso, J. M., Dalla Costa, M. A. and Saraiva, E. S. (2008). A variable inductor MATLAB/simulink behavioral model for application in magnetically-controlled electronic ballasts, *International Symposium on Power Electronics, Electrical Drives, Automation and Motion (SPEEDAM)*, pp. 349–354.

Purhonen, M., Hannonen, J., Strom, J.-P. and Silventoinen, P. (2012). Step-up DC-DC converter passive component dimensioning in photovoltaic applications, *Convention of Electrical and Electronics Engineers in Israel (ICSEE)*, pp. 1–5.

Puukko, J. and Suntio, T. (2012). Dynamic properties of a voltage source inverter-based three-phase inverter in photovoltaic application, *IET Renew. Power Gen.* **6**(6): 381–391.

Qin, L., Xie, S., Hu, M. and Yang, C. (2015). Stable operating area of photovoltaic cells feeding DC-DC converter in output voltage regulation mode, *IET Renewable Power Generation* **9**(8): 970–981.

Redl, R. and Sokal, N. O. (1986). Near-optimum dynamic regulation of DC-DC converters using feed-forward of output current and input voltage with current-mode control, *IEEE Trans. Power Electron.* **PE-1**(3): 181–192.

Reverter, F. and Gasulla, M. (2017). Optimal inductor current in boost DC/DC converters regulating the input voltage applied to low-power photovoltaic modules, *IEEE Trans. Power Electron.* **32**(8): 6188–6196.

Rocabert, J., Luna, A., Blaabjerg, F. and Rodriguez, P. (2012). Control of power converters in AC microgrids, *IEEE Trans. Power Electron.* **27**(11): 4734–4749.

Romero-Cadaval, E., Spagnuolo, G., Franquelo, L. G., Ramos-Paja, C. A., Suntio, T. and Xiao, W. M. (2013). Grid-connected photovoltaic generation plants, *IEEE Ind. Electron. Mag.* **7**(3): 6–20.

Sadowski, N., Batistela, N., Bastos, J. and Lajoie-Mazenc, M. (2002). An inverse Jiles-Atherton model to take into account hysteresis in time-stepping finite-element calculations, *IEEE Trans. Magn.* **38**(2): 797–800.

Sangwongwanich, A., Yang, Y. and Blaabjerg, F. (2016). High-performance constant power generation in grid-connected PV systems, *IEEE Trans. Power Electron.* **31**(3): 1822–1825.

Sulaiman, S. I., Rahman, T. K. A., Musirin, I., Shaari, S. and Sopian, K. (2012). An intelligent method for sizing optimization in grid-connected photovoltaic system, *Solar Energy* **86**(7): 2067–2082.

Sullivan, C. R., Awerbuch, J. J. and Latham, A. M. (2013). Decrease in photovoltaic power output from ripple: simple general calculation and the effect of partial shading, *IEEE Trans. Power Electron.* **28**(2): 740–747.

Sun, Y., Liu, Y., Su, M., Xiong, W. and Yang, J. (2016). Review of active power decoupling topologies in single-phase systems, *IEEE Trans. Power Electron.* **31**(7): 4778–4794.

Suntio, T. (2009). *Dynamic profile of switched-mode converter: modeling, analysis and control*, Wiley-VCH, Germany.

Suntio, T. and Leppäaho, J. (2010). Issues on solar-generator interfacing with current-fed MPP-tracking converters, *IEEE Trans. Power Electron.* **25**(9): 2409–2419.

Suntio, T., Viinamaki, J., Jokipii, J., Messo, T. and Kuperman, A. (2014). Dynamic characterization of power electronics interfaces, *Journal of Emerging and Selected Topics in Power Electronics* **2**(4): 949–961.

Tang, Y. and Blaabjerg, F. (2015). Power decoupling techniques for single-phase power electronics systems - an overview, *Energy Conversion Congress & Exposition (ECCE)*, pp. 2541–2548.

Tonkoski, R. and Lopes, L. A. (2011). Impact of active power curtailment on overvoltage prevention and energy production of PV inverters connected to low voltage residential feeders, *Renewable Energy* **36**(12): 3566–3574.

Tonkoski, R., Lopes, L. A. C. and El-Fouly, T. H. M. (2011). Coordinated active power curtailment of grid connected PV inverters for overvoltage prevention, *IEEE Trans. Sustain. Energy* **2**(2): 139–147.

Urtasun, A., Sanchis, P. and Marroyo, L. (2013). Adaptive voltage control of the DC/DC boost stage in PV converters with small input capacitor, *IEEE Trans. Power Electron.* **28**(11): 5038–5048.

Van De Sype, D. M., Gusseme, K. D., Van Den Bossche, A. and Melkebeek, J. A. (2005). Duty-ratio feedforward for digitally controlled boost PFC converters, *IEEE Trans. Ind. Electron.* **52**(1): 108–115.

Viinamäki, J., Jokipii, J., Messo, T., Suntio, T., Sitbon, M. and Kuperman, A. (2015). Comprehensive dynamic analysis of photovoltaic generator interfacing DC-DC boost power stage, *IET Renewable Power Generation* **9**(4): 306–314.

Viinamaki, J., Jokipii, J. and Suntio, T. (2015). Effect of inductor saturation on the harmonic currents of grid-connected three-phase VSI in PV application, *International Conference on Power Electronics(ICPE-ECCE Asia)*, pp. 1209 – 1216.

Viinamaki, J., Jokipii, J. and Suntio, T. (2016). Improving double-line-frequency voltage ripple rejection capability of DC/DC converter in grid connected two-stage PV inverter using DC-link voltage feedforward keywords, *European Conference on Power Electronics and Applications (EPE)*, pp. 1–10.

Viinamaki, J., Kivimaki, J., Suntio, T. and Hietalahti, L. (2014). Design of boost-power-stage converter for PV generator interfacing, *European Conference on Power Electronics and Applications (EPE)*, pp. 1–10.

Viinamäki, J., Kuperman, A. and Suntio, T. (2017). Grid-forming-mode operation of boost-power-stage converter in PV-generator-interfacing applications, *Energies* **10**(7): 1–23.

Villalva, M. G., de Siqueira, T. G. and Ruppert, E. (2010). Voltage regulation of photovoltaic arrays: small-signal analysis and control design, *IET Power Electronics* **3**(6): 869–880.

Villalva, M. G., Gazoli, J. R. and Ruppert, E. (2009). Comprehensive approach to modeling and simulation of photovoltaic arrays, *IEEE Trans. Power Electron.* **24**(5): 1198–1208.

Wang, J., Chang, N. C. P., Feng, X. and Monti, A. (2015). Design of a generalized control algorithm for parallel inverters for smooth microgrid transition operation, *IEEE Trans. Ind. Electron.* **62**(8): 4900–4914.

Wölfle, W. H. and Hurley, W. G. (2003). Quasi-active power factor correction with a variable inductive filter: theory, design and practice, *IEEE Trans. Power Electron.* **18**(1): 248–255.

Wyatt, J. L. and Chua, L. O. (1983). Nonlinear resistive maximum power theorem with solar cell application, *IEEE Trans. Circuits Syst.* **30**(11): 824–828.

Yang, Y., Enjeti, P., Blaabjerg, F. and Wang, H. (2015). Wide-scale adoption of photovoltaic energy: grid code modifications are explored in the distribution grid, *IEEE Ind. Appl. Mag.* **21**(5): 21–31.

Yang, Y., Wang, H., Blaabjerg, F. and Kerekes, T. (2014). A hybrid power control concept for PV inverters with reduced thermal loading, *IEEE Trans. Power Electron.* **29**(12): 6271–6275.

Zheng, X., Xiao, L., Meng, X., Zhang, F. and Tian, Y. (2013). Optimization of LCL filter based on THD estimation model, *Energy Conversion Congress and Exposition (ECCE)*, pp. 428–433.

Zhu, J., Brundlinger, R., Muhlberger, T., Betts, T. and Gottschalg, R. (2011). Optimised inverter sizing for photovoltaic systems in high-latitude maritime climates, *IET Renewable Power Generation* **5**(1): 58–66.

A H-PARAMETER MODEL

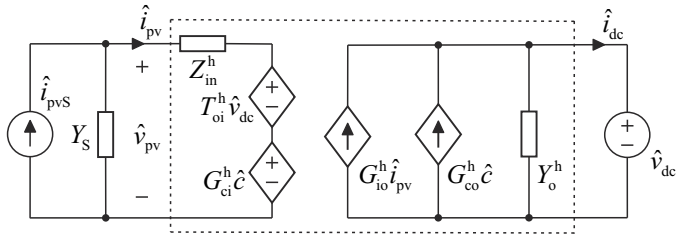

Fig. A.1: Two-port model of current-to-current converter having nonideal source

Source affected h-parameter model

$$\begin{bmatrix} \hat{v}_{\mathrm{pv}} \\ \hat{i}_{\mathrm{dc}} \end{bmatrix} = \begin{bmatrix} Z^{\mathrm{hS}}_{\mathrm{in}} & T^{\mathrm{hS}}_{\mathrm{oi}} & G^{\mathrm{hS}}_{\mathrm{ci}} \\ G^{\mathrm{hS}}_{\mathrm{io}} & -Y^{\mathrm{hS}}_{\mathrm{o}} & G^{\mathrm{hS}}_{\mathrm{co}} \end{bmatrix} \begin{bmatrix} \hat{i}_{\mathrm{pvS}} \\ \hat{v}_{\mathrm{dc}} \\ \hat{c} \end{bmatrix} \tag{A.1}$$

$$Z^{\mathrm{hS}}_{\mathrm{in}} = \frac{Z^{\mathrm{h}}_{\mathrm{in}}}{1 + Y_{\mathrm{s}} Z^{\mathrm{h}}_{\mathrm{in}}} \tag{A.2}$$

$$T^{\mathrm{hS}}_{\mathrm{oi}} = \frac{T^{\mathrm{h}}_{\mathrm{oi}}}{1 + Y_{\mathrm{s}} Z^{\mathrm{h}}_{\mathrm{in}}} \tag{A.3}$$

$$G^{\mathrm{hS}}_{\mathrm{ci}} = \frac{G^{\mathrm{h}}_{\mathrm{ci}}}{1 + Y_{\mathrm{s}} Z^{\mathrm{h}}_{\mathrm{in}}} \tag{A.4}$$

$$G^{\mathrm{hS}}_{\mathrm{io}} = \frac{G^{\mathrm{h}}_{\mathrm{io}}}{1 + Y_{\mathrm{s}} Z^{\mathrm{h}}_{\mathrm{in}}} \tag{A.5}$$

$$Y^{\mathrm{hS}}_{\mathrm{o}} = \frac{1 + Y_{\mathrm{s}} Z^{\mathrm{h}}_{\text{in-oco}}}{1 + Y_{\mathrm{s}} Z^{\mathrm{h}}_{\mathrm{in}}} Y^{\mathrm{h}}_{\mathrm{o}} \tag{A.6}$$

$$G^{\mathrm{hS}}_{\mathrm{co}} = \frac{1 + Y_{\mathrm{s}} Z^{\mathrm{h}}_{\text{in-}\infty}}{1 + Y_{\mathrm{s}} Z^{\mathrm{h}}_{\mathrm{in}}} G^{\mathrm{h}}_{\mathrm{co}}, \tag{A.7}$$

$$Z^{\mathrm{h}}_{\text{in-oco}} = Z^{\mathrm{h}}_{\text{in}} + \frac{G^{\mathrm{h}}_{\text{io}} T^{\mathrm{h}}_{\text{oi}}}{Y^{\mathrm{h}}_{\text{o}}} \tag{A.8}$$

$$Z^{\mathrm{h}}_{\text{in}-\infty} = Z^{\mathrm{h}}_{\text{in}} - \frac{G^{\mathrm{h}}_{\text{io}} G^{\mathrm{h}}_{\text{ci}}}{G^{\mathrm{h}}_{\text{co}}}. \tag{A.9}$$

Closed-loop transfer functions under input voltage control

$$\begin{bmatrix} \hat{v}_{\text{pv}} \\ \hat{i}_{\text{dc}} \end{bmatrix} = \begin{bmatrix} Z^{\mathrm{h}}_{\text{in-c}} & T^{\mathrm{h}}_{\text{oi-c}} & G^{\mathrm{h}}_{\text{ri}} \\ G^{\mathrm{h}}_{\text{io-c}} & -Y^{\mathrm{h}}_{\text{o-c}} & G^{\mathrm{h}}_{\text{ro}} \end{bmatrix} \begin{bmatrix} \hat{i}_{\text{pv}} \\ \hat{v}_{\text{dc}} \\ \hat{v}^{\text{ref}}_{\text{dc}} \end{bmatrix} \tag{A.10}$$

$$Z^{\mathrm{h}}_{\text{in-c}} = \frac{Z^{\mathrm{h}}_{\text{in-o}}}{1 + L^{\mathrm{h}}_{\text{in}}} \tag{A.11}$$

$$T^{\mathrm{h}}_{\text{oi-c}} = \frac{T^{\mathrm{h}}_{\text{oi-o}}}{1 + L^{\mathrm{h}}_{\text{in}}} \tag{A.12}$$

$$G^{\mathrm{h}}_{\text{ri}} = \frac{L^{\mathrm{h}}_{\text{in}}}{1 + L^{\mathrm{h}}_{\text{in}}} \frac{1}{G^{\mathrm{h}}_{\text{se-in}}} \tag{A.13}$$

$$G^{\mathrm{h}}_{\text{io-c}} = \frac{G^{\mathrm{h}}_{\text{io-o}}}{1 + L^{\mathrm{h}}_{\text{in}}} + \frac{L^{\mathrm{h}}_{\text{in}}}{1 + L^{\mathrm{h}}_{\text{in}}} G^{\mathrm{h}}_{\text{io-}\infty} \tag{A.14}$$

$$Y^{\mathrm{h}}_{\text{o-c}} = \frac{Y^{\mathrm{h}}_{\text{o-o}}}{1 + L^{\mathrm{h}}_{\text{in}}} + \frac{L^{\mathrm{h}}_{\text{in}}}{1 + L^{\mathrm{h}}_{\text{in}}} Y^{\mathrm{h}}_{\text{o-}\infty} \tag{A.15}$$

$$G^{\mathrm{h}}_{\text{ro}} = \frac{L^{\mathrm{h}}_{\text{in}}}{1 + L^{\mathrm{h}}_{\text{in}}} \frac{G^{\mathrm{h}}_{\text{co-o}}}{G^{\mathrm{h}}_{\text{ci-o}}} \frac{1}{G^{\mathrm{h}}_{\text{se-in}}}, \tag{A.16}$$

where

$$L^{\mathrm{h}}_{\text{in}} = G^{\mathrm{h}}_{\text{se-in}} G_{\mathrm{c}} G_{\mathrm{a}} G^{\mathrm{h}}_{\text{ci-o}} \tag{A.17}$$

$$G^{\mathrm{h}}_{\text{io-}\infty} = G^{\mathrm{h}}_{\text{io-o}} - \frac{Z^{\mathrm{h}}_{\text{in-o}} G^{\mathrm{h}}_{\text{co-o}}}{G^{\mathrm{h}}_{\text{ci-o}}} \tag{A.18}$$

$$Y^{\mathrm{h}}_{\text{o-}\infty} = Y^{\mathrm{h}}_{\text{o-o}} + \frac{T^{\mathrm{h}}_{\text{oi-o}} G^{\mathrm{h}}_{\text{co-o}}}{G^{\mathrm{h}}_{\text{ci-o}}} \tag{A.19}$$

B G-PARAMETER MODEL OF THE VOLTAGE-BOOSTING DC-DC CONVERTER

$$\begin{bmatrix} \hat{i}_{\mathrm{pv}} \\ \hat{v}_{\mathrm{dc}} \end{bmatrix} = \begin{bmatrix} Y^{\mathrm{g}}_{\text{in-o}} & T^{\mathrm{g}}_{\text{oi-o}} & G^{\mathrm{g}}_{\text{ci-o}} \\ G^{\mathrm{g}}_{\text{io-o}} & -Z^{\mathrm{g}}_{\text{o-o}} & G^{\mathrm{g}}_{\text{co-o}} \end{bmatrix} \begin{bmatrix} \hat{v}_{\mathrm{pv}} \\ \hat{i}_{\mathrm{dc}} \\ \hat{c} \end{bmatrix} \tag{B.1}$$

$$Y^{\mathrm{g}}_{\text{in-o}} = \frac{1}{\Delta^{\mathrm{g}}} \left(\frac{s}{L} + \frac{sC_1}{1 + sr_{\mathrm{C1}}C_1} \Delta^{\mathrm{g}} \right) \tag{B.2}$$

$$T^{\mathrm{g}}_{\text{oi-o}} = \frac{1}{\Delta^{\mathrm{g}}} \frac{D'}{LC_2} \left(1 + sr_{\mathrm{C2}}C_2\right) \tag{B.3}$$

$$G^{\mathrm{g}}_{\text{ci-o}} = \frac{1}{\Delta^{\mathrm{g}}} \left(\frac{D' I_{\mathrm{pv}}}{LC_2} + s\frac{V^{\mathrm{g}}_{\mathrm{eq}}}{L} \right) \tag{B.4}$$

$$G^{\mathrm{g}}_{\text{io-o}} = \frac{1}{\Delta^{\mathrm{g}}} \frac{D'}{LC_2} \left(1 + sr_{\mathrm{C2}}C_2\right) \tag{B.5}$$

$$Z^{\mathrm{g}}_{\text{o-o}} = \frac{1}{\Delta^{\mathrm{g}}} \frac{1}{LC_2} \left(R^{\mathrm{g}}_{\mathrm{eq}} - r_{\mathrm{C2}}D'^2 + Ls \right) \left(1 + sr_{\mathrm{C2}}C_2\right) \tag{B.6}$$

$$G^{\mathrm{g}}_{\text{co-o}} = \frac{1}{\Delta^{\mathrm{g}}} \frac{I_{\mathrm{pv}}}{LC_2} \left(\frac{D' V^{\mathrm{g}}_{\mathrm{eq}}}{I_{\mathrm{pv}}} - R^{\mathrm{g}}_{\mathrm{eq}} - sL \right) \left(1 + sr_{\mathrm{C2}}C_2\right) \tag{B.7}$$

$$\Delta^{\mathrm{g}} = s^2 + s\frac{R^{\mathrm{g}}_{\mathrm{eq}}}{L} + \frac{D'^2}{LC_2} \tag{B.8}$$

$$R^{\mathrm{g}}_{\mathrm{eq}} = r_{\mathrm{L}} + Dr_{\mathrm{sw}} + D' \left(r_{\mathrm{D}} + r_{\mathrm{C2}}\right) \tag{B.9}$$

$$V^{\mathrm{g}}_{\mathrm{eq}} = V_{\mathrm{D}} + V_{\mathrm{dc}} + \left(r_{\mathrm{D}} - r_{\mathrm{sw}} + Dr_{\mathrm{C2}}\right) I_{\mathrm{pv}} \tag{B.10}$$

$$I_{\mathrm{L}} = \frac{I_{\mathrm{dc}}}{D'} \tag{B.11}$$

$$I_{\mathrm{pv}} = I_{\mathrm{L}} \tag{B.12}$$

$$V_{\mathrm{dc}} = V_{\mathrm{C2}} \tag{B.13}$$

$$(r_{C2}I_{dc} - V_D - V_{dc})\,D'^2 + (V_{pv} - (r_D + r_{C2} - r_{sw})\,I_{pv} + V_{pv})\,D' - (r_L + r_{sw})\,I_{dc} = 0 \quad \text{(B.14)}$$

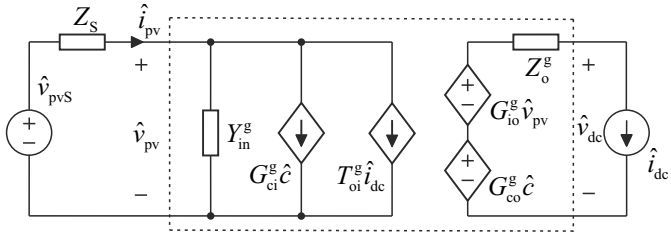

Fig. B.1: Two-port model of voltage-to-voltage converter having nonideal source

Source affected g-parameter model

$$\begin{bmatrix} \hat{i}_{pv} \\ \hat{v}_{dc} \end{bmatrix} = \begin{bmatrix} Y_{in}^{gS} & T_{oi}^{gS} & G_{ci}^{gS} \\ G_{io}^{gS} & -Z_o^{gS} & G_{co}^{gS} \end{bmatrix} \begin{bmatrix} \hat{v}_{pvS} \\ \hat{i}_{dc} \\ \hat{c} \end{bmatrix} \quad \text{(B.15)}$$

$$Y_{in}^{gS} = \frac{Y_{in}^z}{1 + Z_s Y_{in}^g} \quad \text{(B.16)}$$

$$T_{oi}^{gS} = \frac{T_{oi}^z}{1 + Z_s Y_{in}^g} \quad \text{(B.17)}$$

$$G_{ci}^{gS} = \frac{G_{ci}^z}{1 + Z_s Y_{in}^g} \quad \text{(B.18)}$$

$$G_{io}^{gS} = \frac{G_{io}^z}{1 + Z_s Y_{in}^g} \quad \text{(B.19)}$$

$$Z_o^{gS} = \frac{1 + Z_s Y_{in\text{-}sco}^g}{1 + Z_s Y_{in}^g} Y_o^g \quad \text{(B.20)}$$

$$G_{co}^{gS} = \frac{1 + Z_s Y_{in\text{-}\infty}^g}{1 + Z_s Y_{in}^g} G_{co}^g, \quad \text{(B.21)}$$

$$Y^{\mathrm{g}}_{\text{in-sco}} = Y^{\mathrm{g}}_{\text{in}} + \frac{G^{\mathrm{g}}_{\text{io}} T^{\mathrm{z}}_{\text{oi}}}{Z^{\mathrm{g}}_{\text{o}}} \tag{B.22}$$

$$Y^{\mathrm{g}}_{\text{in}-\infty} = Y^{\mathrm{g}}_{\text{in}} - \frac{G^{\mathrm{g}}_{\text{io}} G^{\mathrm{z}}_{\text{ci}}}{G^{\mathrm{g}}_{\text{co}}}. \tag{B.23}$$

Closed-loop transfer functions under output voltage control

$$\begin{bmatrix} \hat{i}_{\text{pv}} \\ \hat{v}_{\text{dc}} \end{bmatrix} = \begin{bmatrix} Y^{\mathrm{g}}_{\text{in-c}} & T^{\mathrm{g}}_{\text{oi-c}} & G^{\mathrm{g}}_{\text{ri}} \\ G^{\mathrm{g}}_{\text{io-c}} & -Z^{\mathrm{g}}_{\text{o-c}} & G^{\mathrm{g}}_{\text{ro}} \end{bmatrix} \begin{bmatrix} \hat{v}_{\text{pv}} \\ \hat{i}_{\text{dc}} \\ \hat{v}^{\text{ref}}_{\text{dc}} \end{bmatrix} \tag{B.24}$$

$$Y^{\mathrm{g}}_{\text{in-c}} = \frac{Y^{\mathrm{g}}_{\text{in-o}}}{1 + L^{\mathrm{g}}_{\text{out}}} + \frac{L^{\mathrm{g}}_{\text{out}}}{1 + L^{\mathrm{g}}_{\text{out}}} Y^{\mathrm{g}}_{\text{in-}\infty} \tag{B.25}$$

$$T^{\mathrm{g}}_{\text{oi-c}} = \frac{T^{\mathrm{g}}_{\text{oi-o}}}{1 + L^{\mathrm{g}}_{\text{out}}} + \frac{L^{\mathrm{g}}_{\text{out}}}{1 + L^{\mathrm{g}}_{\text{out}}} T^{\mathrm{g}}_{\text{oi-}\infty} \tag{B.26}$$

$$G^{\mathrm{g}}_{\text{ri}} = \frac{L^{\mathrm{g}}_{\text{out}}}{1 + L^{\mathrm{g}}_{\text{out}}} \frac{G^{\mathrm{g}}_{\text{ci-o}}}{G^{\mathrm{g}}_{\text{co-o}}} \frac{1}{G^{\mathrm{g}}_{\text{se-out}}} \tag{B.27}$$

$$G^{\mathrm{g}}_{\text{io-c}} = \frac{G^{\mathrm{g}}_{\text{io-o}}}{1 + L^{\mathrm{g}}_{\text{out}}} \tag{B.28}$$

$$Z^{\mathrm{g}}_{\text{o-c}} = \frac{Z^{\mathrm{g}}_{\text{o-o}}}{1 + L^{\mathrm{g}}_{\text{out}}} \tag{B.29}$$

$$G^{\mathrm{g}}_{\text{ro}} = \frac{L^{\mathrm{g}}_{\text{out}}}{1 + L^{\mathrm{g}}_{\text{out}}} \frac{1}{G^{\mathrm{g}}_{\text{se-out}}}, \tag{B.30}$$

where

$$L^{\mathrm{z}}_{\text{out}} = G^{\mathrm{z}}_{\text{se-out}} G_{\mathrm{c}} G_{\mathrm{a}} G^{\mathrm{g}}_{\text{co-o}} \tag{B.31}$$

$$T^{\mathrm{g}}_{\text{oi-}\infty} = T^{\mathrm{g}}_{\text{oi-o}} + \frac{Z^{\mathrm{g}}_{\text{o-o}} G^{\mathrm{g}}_{\text{ci-o}}}{G^{\mathrm{g}}_{\text{co-o}}} \tag{B.32}$$

C Z-PARAMETER MODEL OF THE VOLTAGE-BOOSTING DC-DC CONVERTER

$$\begin{bmatrix} \hat{v}_{\mathrm{pv}} \\ \hat{v}_{\mathrm{dc}} \end{bmatrix} = \begin{bmatrix} Z^{\mathrm{z}}_{\text{in-o}} & T^{\mathrm{z}}_{\text{oi-o}} & G^{\mathrm{z}}_{\text{ci-o}} \\ G^{\mathrm{z}}_{\text{io-o}} & -Z^{\mathrm{z}}_{\text{o-o}} & G^{\mathrm{z}}_{\text{co-o}} \end{bmatrix} \begin{bmatrix} \hat{i}_{\mathrm{pv}} \\ \hat{i}_{\mathrm{dc}} \\ \hat{c} \end{bmatrix} \tag{C.1}$$

$$Z^{\mathrm{z}}_{\text{in-o}} = \frac{1}{\Delta^{\mathrm{z}}} \frac{1}{C_1} \left(s^2 + s \frac{R^{\mathrm{z}}_{\mathrm{eq}} - r_{\mathrm{C1}}}{L} + \frac{D'^2}{LC_2} \right) A_2 \tag{C.2}$$

$$T^{\mathrm{z}}_{\text{oi-o}} = -\frac{1}{\Delta^{\mathrm{z}}} \frac{D'}{LC_1C_2} A_1 A_2 \tag{C.3}$$

$$G^{\mathrm{z}}_{\text{ci-o}} = -\frac{1}{\Delta^{\mathrm{z}}} \frac{V^{\mathrm{z}}_{\mathrm{eq}}}{LC_1} \left(s + \frac{D' I_{\mathrm{pv}}}{V^{\mathrm{z}}_{\mathrm{eq}} C_2} \right) A_1 \tag{C.4}$$

$$G^{\mathrm{z}}_{\text{io-o}} = \frac{1}{\Delta^{\mathrm{z}}} \frac{D'}{LC_1C_2} A_1 A_2 \tag{C.5}$$

$$Z^{\mathrm{z}}_{\text{o-o}} = \frac{1}{\Delta^{\mathrm{z}}} \frac{1}{C_2} \left(s^2 + s \frac{R^{\mathrm{z}}_{\mathrm{eq}} - D'^2 r_{\mathrm{C2}}}{L} + \frac{1}{LC_1} \right) A_2 \tag{C.6}$$

$$G^{\mathrm{z}}_{\text{co-o}} = -\frac{1}{\Delta^{\mathrm{z}}} \frac{I_{\mathrm{pv}}}{C_2} \left(s^2 - s \frac{D' V^{\mathrm{z}}_{\mathrm{eq}} - R^{\mathrm{z}}_{\mathrm{eq}} I_{\mathrm{pv}}}{I_{\mathrm{pv}} L} + \frac{1}{LC_1} \right) A_2 \tag{C.7}$$

$$\Delta^{\mathrm{z}} = s^3 + s^2 \frac{R^{\mathrm{z}}_{\mathrm{eq}}}{L} + s \frac{C_2 + D'^2 C_1}{LC_1C_2} \tag{C.8}$$

$$R^{\mathrm{z}}_{\mathrm{eq}} = r_{\mathrm{L}} + r_{\mathrm{C1}} + D r_{\mathrm{sw}} + D' \left(r_{\mathrm{D}} + r_{\mathrm{C2}} \right) \tag{C.9}$$

$$V^{\mathrm{z}}_{\mathrm{eq}} = V_{\mathrm{D}} + V_{\mathrm{dc}} + \left(r_{\mathrm{D}} - r_{\mathrm{sw}} + D r_{\mathrm{C2}} \right) I_{\mathrm{pv}} \tag{C.10}$$

$$A_1 = 1 + s r_{\mathrm{C1}} C_1 \tag{C.11}$$

$$A_2 = 1 + s r_{\mathrm{C2}} C_2 \tag{C.12}$$

$$I_{\mathrm{L}} = \frac{I_{\mathrm{dc}}}{D'} = I_{\mathrm{pv}} \tag{C.13}$$

$$D' = \frac{I_{\mathrm{dc}}}{I_{\mathrm{pv}}} \tag{C.14}$$

$$V_{\mathrm{pv}} = V_{\mathrm{C1}} \tag{C.15}$$

$$V_{\mathrm{dc}} = V_{\mathrm{C2}} \tag{C.16}$$

$$V_{\mathrm{pv}} = D'V_{\mathrm{dc}} + D'V_{\mathrm{D}} + \left(r_{\mathrm{L}} + Dr_{\mathrm{sw}} + D'r_{\mathrm{D}} + DD'r_{\mathrm{C2}}\right) I_{\mathrm{pv}} \tag{C.17}$$

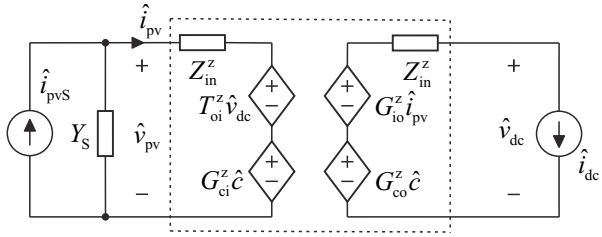

Fig. C.1: Two-port model of the current-to-voltage converter having nonideal source

Source affected z-parameter model

$$\begin{bmatrix} \hat{v}_{\mathrm{pv}} \\ \hat{v}_{\mathrm{dc}} \end{bmatrix} = \begin{bmatrix} Z^{\mathrm{zS}}_{\mathrm{in}} & T^{\mathrm{zS}}_{\mathrm{oi}} & G^{\mathrm{zS}}_{\mathrm{ci}} \\ G^{\mathrm{zS}}_{\mathrm{io}} & -Z^{\mathrm{zS}}_{\mathrm{o}} & G^{\mathrm{zS}}_{\mathrm{co}} \end{bmatrix} \begin{bmatrix} \hat{i}_{\mathrm{pvS}} \\ \hat{i}_{\mathrm{dc}} \\ \hat{c} \end{bmatrix} \tag{C.18}$$

$$Z^{\mathrm{zS}}_{\mathrm{in}} = \frac{Z^{\mathrm{z}}_{\mathrm{in}}}{1 + Y_{\mathrm{s}}Z^{\mathrm{z}}_{\mathrm{in}}} \tag{C.19}$$

$$T^{\mathrm{zS}}_{\mathrm{oi}} = \frac{T^{\mathrm{z}}_{\mathrm{oi}}}{1 + Y_{\mathrm{s}}Z^{\mathrm{z}}_{\mathrm{in}}} \tag{C.20}$$

$$G^{\mathrm{zS}}_{\mathrm{ci}} = \frac{G^{\mathrm{z}}_{\mathrm{ci}}}{1 + Y_{\mathrm{s}}Z^{\mathrm{z}}_{\mathrm{in}}} \tag{C.21}$$

$$G^{\mathrm{zS}}_{\mathrm{io}} = \frac{G^{\mathrm{z}}_{\mathrm{io}}}{1 + Y_{\mathrm{s}}Z^{\mathrm{z}}_{\mathrm{in}}} \tag{C.22}$$

$$Z^{\mathrm{zS}}_{\mathrm{o}} = \frac{1 + Y_{\mathrm{s}}Z^{\mathrm{z}}_{\mathrm{in\text{-}sco}}}{1 + Y_{\mathrm{s}}Z^{\mathrm{z}}_{\mathrm{in}}} Z^{\mathrm{z}}_{\mathrm{o}} \tag{C.23}$$

$$G^{\mathrm{zS}}_{\mathrm{co}} = \frac{1 + Y_{\mathrm{s}}Z^{\mathrm{z}}_{\mathrm{in\text{-}\infty}}}{1 + Y_{\mathrm{s}}Z^{\mathrm{z}}_{\mathrm{in}}} G^{\mathrm{z}}_{\mathrm{co}}, \tag{C.24}$$

$$Z^{\mathrm{z}}_{\text{in-sco}} = Z^{\mathrm{z}}_{\text{in}} + \frac{G^{\mathrm{z}}_{\text{io}} T^{\mathrm{z}}_{\text{oi}}}{Z^{\mathrm{z}}_{\text{o}}} \tag{C.25}$$

$$Z^{\mathrm{z}}_{\text{in}-\infty} = Z^{\mathrm{h}}_{\text{in}} - \frac{G^{\mathrm{z}}_{\text{io}} G^{\mathrm{z}}_{\text{ci}}}{G^{\mathrm{z}}_{\text{co}}}. \tag{C.26}$$

Closed-loop transfer functions under output voltage control

$$\begin{bmatrix} \hat{v}_{\text{pv}} \\ \hat{v}_{\text{dc}} \end{bmatrix} = \begin{bmatrix} Z^{\mathrm{z}}_{\text{in-c}} & T^{\mathrm{z}}_{\text{oi-c}} & G^{\mathrm{z}}_{\text{ri}} \\ G^{\mathrm{z}}_{\text{io-c}} & -Z^{\mathrm{z}}_{\text{o-c}} & G^{\mathrm{z}}_{\text{ro}} \end{bmatrix} \begin{bmatrix} \hat{i}_{\text{pv}} \\ \hat{i}_{\text{dc}} \\ \hat{v}^{\text{ref}}_{\text{dc}} \end{bmatrix} \tag{C.27}$$

$$Z^{\mathrm{z}}_{\text{in-c}} = \frac{Z^{\mathrm{z}}_{\text{in-o}}}{1 + L^{\mathrm{z}}_{\text{out}}} + \frac{L^{\mathrm{z}}_{\text{out}}}{1 + L^{\mathrm{z}}_{\text{out}}} Z^{\mathrm{z}}_{\text{in-}\infty} \tag{C.28}$$

$$T^{\mathrm{z}}_{\text{oi-c}} = \frac{T^{\mathrm{z}}_{\text{oi-o}}}{1 + L^{\mathrm{z}}_{\text{out}}} + \frac{L^{\mathrm{z}}_{\text{out}}}{1 + L^{\mathrm{z}}_{\text{out}}} T^{\mathrm{z}}_{\text{oi-}\infty} \tag{C.29}$$

$$G^{\mathrm{z}}_{\text{ri}} = \frac{L^{\mathrm{z}}_{\text{out}}}{1 + L^{\mathrm{z}}_{\text{out}}} \frac{G^{\mathrm{z}}_{\text{ci-o}}}{G^{\mathrm{z}}_{\text{co-o}}} \frac{1}{G^{\mathrm{z}}_{\text{se-out}}} \tag{C.30}$$

$$G^{\mathrm{z}}_{\text{io-c}} = \frac{G^{\mathrm{z}}_{\text{io-o}}}{1 + L^{\mathrm{z}}_{\text{out}}} \tag{C.31}$$

$$Z^{\mathrm{z}}_{\text{o-c}} = \frac{Z^{\mathrm{z}}_{\text{o-o}}}{1 + L^{\mathrm{z}}_{\text{out}}} \tag{C.32}$$

$$G^{\mathrm{z}}_{\text{ro}} = \frac{L^{\mathrm{z}}_{\text{out}}}{1 + L^{\mathrm{z}}_{\text{out}}} \frac{1}{G^{\mathrm{z}}_{\text{se-out}}}, \tag{C.33}$$

where

$$L^{\mathrm{z}}_{\text{out}} = G^{\mathrm{z}}_{\text{se-out}} G_{\mathrm{c}} G_{\mathrm{a}} G^{\mathrm{z}}_{\text{co-o}} \tag{C.34}$$

$$T^{\mathrm{z}}_{\text{oi-}\infty} = T^{\mathrm{z}}_{\text{oi-o}} + \frac{Z^{\mathrm{z}}_{\text{o-o}} G^{\mathrm{z}}_{\text{ci-o}}}{G^{\mathrm{z}}_{\text{co-o}}} \tag{C.35}$$

D SIMULATION MODEL OF THREE-PHASE PV INVERTER HAVING SATURATING GRID-FILTER INDUCTORS

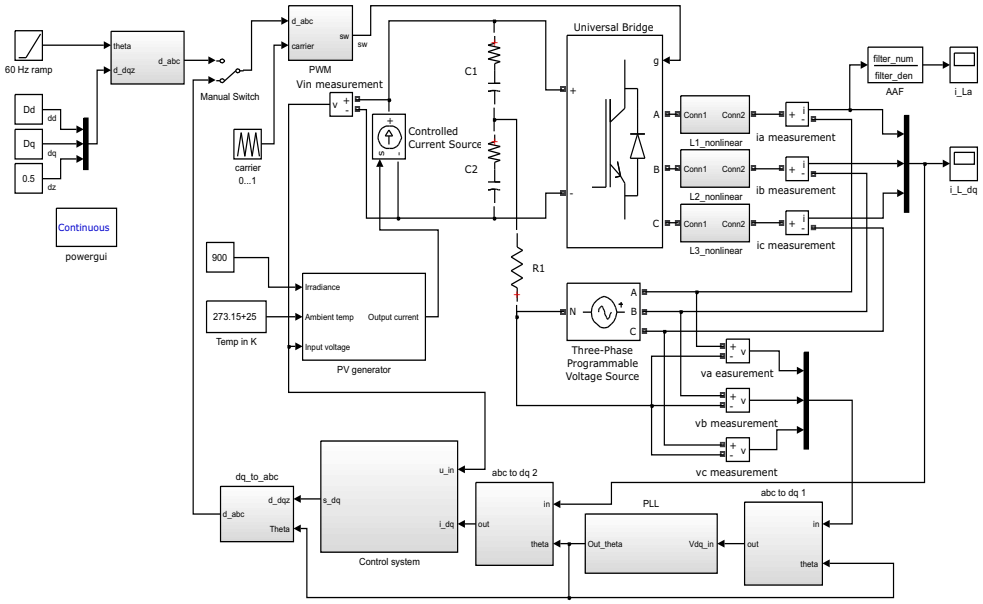

Fig. D.1: Implementation of the simulation model in MATLAB Simulink

E LABORATORY SETUP

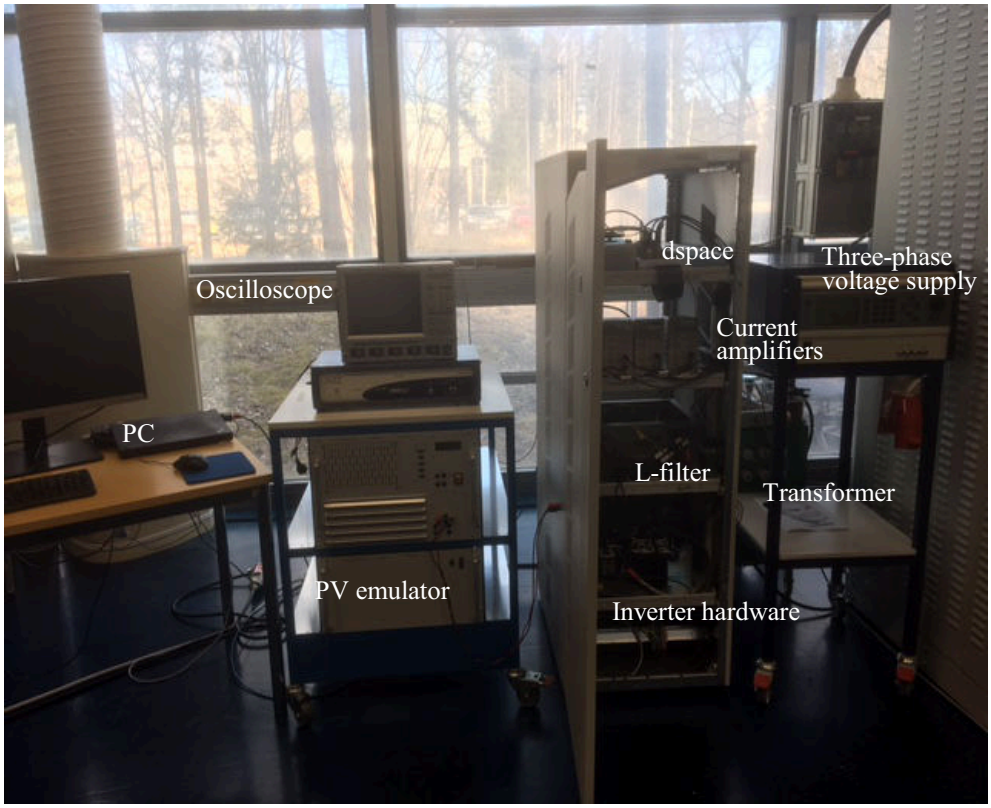

Fig. E.1: Laboratory setup for measuring the three-phase PV inverter

Tampereen teknillinen yliopisto
PL 527
33101 Tampere

Tampere University of Technology
P.O.B. 527
FI-33101 Tampere, Finland

ISBN 978-952-15-4049-3
ISSN 1459-2045